The University of Alabama in Huntsville Research Report

GRAVITY WAVE INITIATED CONVECTION

National Aeronautics and Space Administration Headquarters

Research Grant: NAGW-1165

Prepared by

R. J. Hung

The University of Alabama in Huntsville

Huntsville, Alabama 35899

The present research grant has resulted in the following referred article publications:

(1) Hung, R. J., Dodge, J. C., Liu J.M., and Smith, R. E., Remote Sensing of Cloud Distributions over the Bayanhar Mountains--Watershed of the Yangtze and Yellow Rivers, International Journal of Remote Sensing, 7, 577-587, 1986.

(2) Hung, R. J., and Tsao, Y. D., Study of Prestorm Environment by Using Rawinsonde and Satellite Observations, International Journal of Remote Sensing, 8, 1123-1150, 1987.

(3) Hung, R. J., Liu, J. M., Satellite Remote Sensing and Ozonesonde Observation of Ozone Vertical Profile and Severe Storm Development, International Journal of Remote Sensing, 9, 469-475, 1988.

(4) Hung, R. J., Tsao, Y. D., Johnson, D. L., Chen, A. J., Lin, C. H., Cheng, J. M., and You, C. M., VHF Radar Remote Sensing of Atmospheric Parameters Over Taiwan During the Time Period of Typhoon Wayne, International Journal of Remote Sensing, 9, 477-493, 1988.

(5) Hung, R. J., and Tsao, Y. D., Satellite Remote Sensing and Cloud Modeling of St. Anthony, Minnesota Storm Clouds and Dew Point Depression, Annales Geophysics, 6, 453-462, 1988.

(6) Hung, R. J., Tsao, Y. D., and Dodge, J. C., Satellite Observation and Mesoscale Cloud Modeling of St. Anthony, Minnesota Storm Clouds, Advances in Space Research, 9, No. 7, 415-423, 1989.

(7) Hung, R. J., Tsao, Y. D., Lee, C. C., Johnson, D. L., Chen, A. J.,

Lin, C. H., and Pan, J. J., Observations on Thermospheric and Mesospheric Density Disturbances Caused by Typhoons and Convective Storms, Journal of Spacecraft and Rockets, 27, 285-298, 1990.

(8) Hung, R. J., and Tsao, Y. D., Study of Ardmore, Oklahoma Convective Storm Cloud Initiation and Development Based on the Remote Sensing Gravity-Wave Induced Convection, International Journal of Remote Sensing, 11, in press, 1990.

(9) Hung, R. J., and Tsao, Y. D., Satellite Infrared Remote Sensing and Numerical Simulation of Ardmore, Oklahoma Storm Clouds, International Journal of Remote Sensing, 11, in press, 1990.

(10) Hung, R. J., Dodge, J. C., Satellite Remote Sensing of Water Resources in the Yangtze and Yellow Rivers of China Based on Infrared Imagery of Cloud Distributions, Progress in Aeronautics and Astronautics, 130, in press, 1990.

Following two sections of papers are also enclosed in this report:

Section I: Convective Storm Cloud Initiation and Development Based on the Remote Sensing Gravity Wave-Induced Convection

Section II: Satellite Infrared Remote Sensing and Numerical Simulation of Storm Clouds.

SECTION I

CONVECTIVE STORM CLOUD INITIATION AND DEVELOPMENT BASED ON THE REMOTE SENSING GRAVITY WAVE-INDUCED CONVECTION

Abstract

Convective instability can be induced by unstable vertical temperature profiles and can be supported by the release of latent heat of water vapor provided by a large quantity of moisture in the air. It can also be released by the presence of gravity waves. Large amplitude gravity waves have been linked to the onset of convective storm systems. In this study, the vertical velocity of convection initiated by gravity waves was investigated. The study of Ardmore, Oklahoma storms showed that weak convection was initiated by gravity waves having wave periods of 35 minutes, and the convection was enhanced by gravity waves having wave periods of 20 minutes. Cloud formation, due to the condensation of water vapor through convection initiated by the gravity waves, was evidenced from rapid-scan satellite imagery and radar summaries. In this particular case, the convective motion-initiated and supported by the gravity wave-induced activity (excluding contributions made by other mechanisms) reached its maximum value about one hour before the production of the funnel clouds. In this study, we did not rule out the contributions made by other mechanisms, such as low-level convergence and others, toward the initiation of convection; however, our main purpose is to discuss the role of gravity waves in wave-induced convection contributing to the fractions of formation and development of severe convective storms.

1. Introduction

In laboratory experiments Townsend (1964), Deardorff et al. (1969), Willis and Deardorff (1974), and Adrian (1975) observed that gravity waves were excited when convective elements overshot the top of the mixed layer and penetrated a short distance upward into the stable region. Curry and Murty (1974), Gossard and Sweezy (1974), Stull (1976), etc., have suggested that thunderstorms or fronts could excite gravity waves in the atmosphere. Einaudi and Lalas (1975) indicated that gravity waves can propagate upward through the atmosphere and stimulate cloud growth. In the observation of the equatorial ionosphere, Rottger (1977) showed the association of gravity waves with penetrative cumulus convection. Matsumoto and Akiyama (1969) contended that gravity waves were responsible for the pulsating tendency of winter and summer convective storms in western Japan. Uccellini (1975) proposed that gravity waves were an important mechanism for triggering severe convective storms.

Ray tracing of detected gravity waves showed that the source of the gravity waves was located in the cloud at the time of enhanced convection (Hung et al., 1979a; 1980; 1983; Hung and Smith, 1983). It is shown in this study that convective storms are triggered by gravity waves, and clouds with enhanced convection also excite gravity waves.

A number of case studies revealed that the existence of large amplitude gravity waves has a significant effect upon mesoscale weather features such as surface wind gusts, mid-level cloud distribution, and convective storm development. The earlier diagnostic study revealed that a cause and effect relationship

between gravity waves and severe convective storm development is credible (Uccellini, 1975).

Vertical velocity of the gravity wave-induced convection can be calculated through consideration of wave intensity (amplitude of the surface pressure perturbation), wavelength, and phase velocity of gravity waves (Eom, 1975). Vertical velocity of induced convective motions at different altitudes can also be calculated with the consideration of density ratios at different altitudes of the propagation medium, and with average wind velocities at the altitudes of induced convection and lifting (Uccellini, 1975). The computed results of the vertical velocity of induced convection initiated by gravity waves have been compared with radar, rapid-scan satellite imagery, and cloud modeling.

2. Meteorological Background

In this study, a severe storm at Ardmore, Oklahoma, at 0054 GMT (1854 LT), 30 April 1985 was chosen as a sample to study the initiation, formation and development of storm clouds based on gravity wave-induced convection. The results were compared with rapid-scan satellite infrared remote sensing and numerical modeling of storm clouds. On the evening of 29 April (LT), a tornado touched down at 1854 LT, about 20 km southwest of Ardmore, Oklahoma. The tornado moved north about 4.8 km, and then turned northeast and traveled another 17.6 km through the southeast outskirts of Ardmore before dissipating. The liftoff time of the tornado was 0131 GMT (1931 LT). Storm damage was rated as F2 on the Fujita Scale (National

Climate Data Center, 1985).

Surface meteorological data, in Figure 1, shows that there was a low pressure located at the southern part of North Dakota from where the cold front extended to a southwest direction, through South Dakota, Nebraska, Colorado, Utah to Nevada. In the southeast United States, there was another cold front located over Alabama and Florida. Figure 1 also shows that the area of low pressure extended through southwestern Nebraska, western Kansas, central and western Oklahoma, all of Texas except the eastern corner of the state, and southeastern New Mexico, at 0000 GMT, 30 April 1985. There were three axes of low pressure troughs: one along western Kansas, northeastern tip of Oklahoma, north central and south central Texas; the other along central and south central Oklahoma and eastern Texas; and the third along western Missouri, western Arkansas, and western Louisiana. The location of the Ardmore storm clouds was on the middle axis of the low pressure trough. This middle axis of low pressure developed into a cold front 12 hours later. There were several centers of high pressure surrounding this area of low pressure located over: Ohio, Arizona, and the Gulf of Mexico near Mississippi and Alabama. The area of low pressure was surrounded by the cold front located at the northwestern area of the U.S.; and the high pressure center, located at the southeastern area of the U.S., and at the Gulf of Mexico. Meanwhile, a large quantity of warm, moist air from the Gulf of Mexico moved into the south central area of the U.S. (see Figure 2). Twelve hours before the development of the cold front in the area of tornado occurrence, the atmosphere was unstable which could have easily

produced convective motion if there had been any triggering mechanism. The location of the tornado touchdown is marked on Figure 1 with a solid circle at south central Okalahoma, near the Texas border.

Figure 3 shows the skew T-log P temperature (solid line) and dew point temperature (dashed line) diagrams for Oklahoma City, Oklahoma at 0000 GMT, 30 April 1985. At the altitudes below 500 mb, there were four different heights at which the temperature lapse rates were dry adiabatic. These heights were between 820 and 850 mb, between 680 and 730 mb, and between 510 and 540 mb. Temperature inversions existed between those unstable regions. In the upper troposphere, there existed a height in which the temperature lapse rate was near dry adiabatic at the altitudes between 250 and 370 mb.

The possibility of cloud formation is dependent upon the amount of moisture available to provide the energy source for the initiation of condensation. Figure 3 shows the dew point temperature profile. Low dew point depression is an indication of high moisture concentration. There was moist air all the way from 550 mb to the surface. The dew point depression was smaller than $0.6^{\circ}C$ between the altitudes of 700 and 850 mb; and smaller than $0.8^{\circ}C$ between the altitudes of 590 and 610 mb.

Both the lifting condensation level (LCL) and the level of free convection (LFC) can be calculated from Figure 3. It was found that the LCL was at the 930 mb height, and the LFC was at 770 mb height.

Using techniques similar to those of Bluestein and Parks (1983), and Bluestein and Jain (1985), rawinsonde data was used to compute the

convective inhibition (CIN) (Colby, 1984), and the convective available potential energy (CAPE) (Moncrieff and Miller, 1976; Weisman and Klemp, 1982). CIN is the net work per unit mass required to lift a negatively buoyant air parcel from the surface to the level of free convection (LFC). The calculated value of CIN in this case is 27.44 $J.kg^{-1}$. CAPE is the net work per unit mass done by the environment on an air parcel (energy per unit mass gained by the air parcel) which rises from the LFC to the equilibrium level (lowest level of zero potential temperature excess above the LFC). In this case, the calculated value of CAPE is 2339 $J.kg^{-1}$. The CIN is a measure of the low-level thermodynamic stability, while the CAPE is a measure of the potential instability. The analysis of the convective instability, based on CIN and CAPE, showed that the pre-storm conditions were famorable for the development of severe storms (Bluestein and Jain, 1985).

Furthermore, the tropospheric humidity (Bluestein and Parks, 1983), and the bulk Richardson number (Moncrieff and Green, 1972; Weisman and Klemp, 1982) can be computed from rawinsonde data. The tropospheric humidity (ratio of precipitable water to saturation precipitable water) has been shown to be a good measure of the amount of vertically integrated water vapor in a column of air because it is relatively insensitive to layers of high relative humidity aloft in which the absolute amount of water vapor is low (Bluestein and Jain, 1985). In this case, the calculated value of the tropospheric humidity was 61%. The bulk Richardson number is the ratio of the total evergy available due to buoyancy, to the total energy available

from vertical shear. The calculated value of the bulk Richardson number (Ri) in this case was 65. Weisman and Klemp (1982) found observational and numerical evidence that low values of Ri (roughly between 15 and 35) favor the development of supercell thunderstorms; while high values of Ri (larger than 40) favor the development of multicell storms. The analysis of both the tropospheric humidity (Bluestein and Parks, 1983; Bluestein and Jain, 1985) and Ri showed that both water vapor content and wind profile were in favor of the development of severe storms.

The 850 mb synoptic map is shown in Figure 4. The location of the tornado touchdown is marked with a solid circle at south central Oklahoma, near the Texas border. The figure shows that convective cells of tornadic storms (marked with a solid circle) occurred at the boundary between low and high pressures. The center of low pressure was located at southeastern Colorado and northeastern New Mexico, and the center of high pressure was located at the Gulf of Mexico near Louisiana, with another center of high pressure at eastern Michigan. At this location of tornado occurrence, there was a convergence and confluence of flows made by southwest and southeast winds which brought warm, moist air from the Gulf of Mexico to the location of interest. Figures 5 and 2 show a geographical distribution of surface divergence (with a unit of 10^{-5} sec^{-1}), and a geographical distribution of surface moisture content (mixing ratio with a unit of g/kg), respectively, both at 0000 GMT, 30 April 1985, based on the available surface data. It is shown that, in the neighborhood of tornado occurence, the surface divergence was $-2x10^{-5}$ sec^{-1} (negative

value implies convergence), and a high concentration of moisture with mixing ratio of 13 g/kg. The temperature at the location of the tornado occurrence was 15°C at 850 mb height.

Figure 6 shows the radar summary at 2235 GMT, 29 April 1985. A convective cloud belt extending from Colorado to Louisiana is shown in the figure. This convective cloud belt was scattered in the area between the three axes of the low pressure trough where the atmosphere was extremely moist and unstable.

In general, radar returns show the echoes of radio waves reflected from the condensation systems which form the convective cloues. In convective cloud systems, both updraft and downdraft motions can exist at the same time. For high and low pressure areas shown in the surface weather map, low always corresponds to the convergence, and high is the divergence. Comparison between Figures 1 and 5 shows the correspondence between low and convergence; and also between high and divergence. Furthermore, comparison between Figures 5 and 6 also shows that radar echoes can appear either in the areas of convergence and/or divergence, but not in the area of zero surface divergence.

Radar returns, given in Figure 6, show that there were not any cloud formations at south central Oklahoma, near the Texas borderline before 2235 GMT (radar summaries are available at one-hour intervals). Satellite infrared imagery from GOES also shows that clouds did not form before 2300 GMT in south central Oklahoma. Figure 7 shows a time history of cloud formation and development for clouds responsible for the outbreak of tornadic storms. The cloud formed at

2314 GMT, and grew rapidly to the mature stage within one hour. This cloud merged with the rest of the cloud belt after 0200 GMT.

The temperature distribution of the cloud responsible for the outbreak of tornadic storms at 0100 GMT (time of tornado touchdown) was based on the analysis from the satellite infrared imagery shown in Figure 8. Rawinsonde data at Oklahoma City, Oklahoma showed that the tropopause temperature was -57 ^{0}C at 0000GMT. The lowest satellite-observed cloud-top temperature of -60 ^{0}C, at the southwestern part of the cloud, indicates the location of the highest one of the overshooting cloud-tops of the cloud system responsible for the formation of the funnel cloud in this case.

3. Characteristics of Gravity Waves Detected

Gravity waves associated with tornado activity (Hung et al., 1978; Hung and Smith, 1978) and hurricanes (Hung and Kuo, 1978; Hung et al., 1988; 1989) have been observed with a high frequency continuous radio wave Doppler array system and a VHF radar system. By using a ray tracing technique, Hunt et al. (1979 a,b) have shown that the enhanced convection-initiated gravity waves associated with severe storms were generated by thunderheads embedded in a squall line and/or an isolated cloud with intense convection.

High wind shear, flows across topographical barriers, and convectively unstable flows are believed to be the major causes of the excitation of gravity waves. Of the three dominant wave sources, gravity waves associated with convection are the least understood. In the case studied here, wave-like disturbances were observed in

microbarograph data while the squall line was active. Figure 9 shows the geographical distribution of microbarogram stations in the south central United States. The stations are marked with hollow circles and station numbers. Figure 10 shows a three station sample microbarograph data from Dallas/Ft. Worth, Texas (station number S21, shown in Figure 9); Amarillo, Texas (station number S14); and San Angelo, Texas (station number S26), during the time period between 2040 to 2155 GMT, 29 April 1985. A unit of pressure fluctuation is also shown with an arrow in the figure. The microbarograph data at each location were subfected to power-spectral density analysis in order to obtain the wave periods of the fluctuation; the direction of propagation and the phase velocity of the waves were obtained from cross correlation analysis from a combination of three stations. detailed descriptions of the data analysis technique are given by Hung et al. (1978) and Hung and Smith (1978). A window was chosen for the filtering of waves if multiple waves were detected in a power spectral density analysis (Hung et al., 1978).

In general, amplitudes of gravity waves in the tropospheric heights are too small to be considered linear waves. These amplitudes of gravity waves are enlarged as they propagate upward. The wave amplitudes vary inversely proportional to the square root of the density of propagation medium. Saturation of gravity waves may occur at mesospheric heights in which the wave field has reached amplitudes which may cause secondary instabilities (Lindzen, 1981; Dunkerton, 1982); or nonlinear interactions, such as the parametric subharmonic instability (Lindzen and Forbes, 1983), to occur, which

limits further wave growth. In our case, for gravity waves in the troposphere, waves are considered to be the linear waves in which nonlinear wave-wave interactions can be ignored in the calculation.

This study concentrates on gravity waves associated with mesoscale convective systems. Two-hour data samples from each microbarogram station were used in this study, from 1900 GMT (5 hours ahead of the tornado touchdown), 29 April 1985 to 0200 GMT (about liftoff time of the tornado), 30 April 1985. Figures A-1, A-2, A-3, A-4, and A-5 in Appendix A show the wave period, phase speed, propagation direction and the area of gravity waves detected during the time periods of 1900 to 2100, 2015 to 2215, 2130 to 2330, 2245 to 0045, and 0000 to 0200 GMT, respectively.

Tables B-1 through B-5 in Appendix B listed the wave peirod, wavelength, phase velocity, direction of the wave propagation (measured clockwise from the north), and the geographical area of coverage for each gravity wave detected, based on a cross correlation analysis from a combination of three microbarogram stations. The three stations comprising the area of coverage for each gravity wave are identified by an Arabic number corresponding to the locations shown in Figure 9.

Since we are interested only in the mesoscale gravity waves (with a wave period shorter than an hour), we have excluded gravity waves with synoptic scales (with a wave period longer than an hour). In other words, wave periods in the range of 5 to 60 minutes are of particular interest. About 5 to 6 hours before touchdown of the tornado (Figure A-1 and Table B-1), there were three groups of gravity

waves detected in the areas of eastern Kansas, southwestern Missouri, and northern Arkansas. The ray tracing technique has been used to trace the locations of wave sources by using characteristics of gravity waves (such as wave period, wavelength, phase velocity and direction of wave propagation) obtained from microbarograph data, and physical properties of wave propagation medium [such as three dimensional distribution (height and geographical locations) of temperature, density and wind profiles] obtained from rawinsonde data. All the rawinsonde data is stored in the Man Computer Interactive Data Access System (McIDAS) which is available at NASA Marshall Space Flight Center, Huntsville, Alabama. A detailed description of the technique of ray tracing computation has been discussed by Hung et al. (1978), Hung and Smith (1978), and Hung et al. (1980). This technique takes into consideration the probability of errors in the determination of the aximuthal angle of the wave arrival, the characteristics of the gravity waves, and the physical properties of the wave propagation medium to be used in the determination of the location of the wave sources.

Based on ray tracing, it is obvious, that most of the gravity waves, listed in Tables B-1 to B-5 of Appendix B, were excited by convective cloud systems at A (eastern Colorado, western Kansas and the northern tip of the Texas panhandle), B (northern and eastern Louisiana, southeastern Arkansas, and western Mississippi), and C (eastern Kansas, northwestern Arkansas and western Missouri) areas, shown as rectangles enclosed by dashed lines in radar summary (Figure 6). Figure 11 shows sample ray tracings selected from some of the

gravity waves shich initiated the most prominant contributions in induced convection. These selected gravity waves are those marked in the last column of Tables B-1 through B-5 of Appendix B. In this particular case, as shown in Figure 11, based on ray tracing, the No. 12 gravity waves (listed in Table B-2) having wave periods of 35 minutes originated from the convective cloud systems at area A shown in Figures 6 propagated to location I in Figure 11; the No. 3 gravity waves (listed in Table B-3) with wave periods of 20 minutes originated from convective cloud systems at area C propagated to location II in Figure 11; the No. 18 gravity waves (listed in Table B-3) originated from the convective cloud systems at area B propagated to location III in Figure 11; the No.1 gravity waves (listed in Table B-5) with wave period of 20 minutes originated from the convective cloud systems at area A propagated to locaiton IV in Figure 11; and the No. 9 gravity waves (listed in Table B-5) with wave period of 35 minutes originated from the convective cloud at area B propagated to location V in Figure 11. It has been statistically shown that large amplitude gavity waves associated with convective clouds, fronts, squall lines, jet streams, etc., are very likely responsible for the initiation of severe convective storms (Hung and Smith, 1981).

About 4 to 5 hours before the touchdown of the tornado (Figure A-2 and Table B-2), 15 gravity waves were detected in the areas of Kansas, eastern Missouri, Oklahoma, Arkansas, northwestern Mississippi, and northern Texas. Based on ray tracing, it was found that the No. 3 gravity waves originated from the convective system of the cloud belt in area C; Nos. 9 and 12 gravity waves were from area A; and No. 14

gravity waves were from area B, shown in Figure 6. Figure 11 shows a sample ray tracing I for the No. 12 gravity waves that propagated from the wave source of the convective cloud system at area A, to the location of waves detected at north central Texas.

About 3 to 4 hours before the touchdown of the tornado (Figure A-5 and Table B-3), 18 gravity waves were detected in the areas of Kansas, southern Missouri, Arkansas, northern Louisiana, Oklahoma, and north central Texas. Based on ray tracing computation, it was found that the Nos. 2, 6, 7, 8, and 11 gravity waves originated from the convective system of the cloud belt in area A; Nos. 3 and 9 gravity waves were from area C; and No. 18 gravity wave was from area B, shown in Figure 6. Figure A-4 shows additional ray tracing II and III for Nos. 3 and 18 gravity waves illustrated in Table B-3, respectively. The No. 3 gravity wave propagated from the wave source of the convective cloud system at area C; while the No. 18 gravity wave originated from area B to the location of waves detected at north central Texas.

About 2 to 3 hours before the touchdown of the tornado (Figure A-4 and Table B-4), 21 gravity waves were detected in southern Missouri, Arkansas, northwestern Mississippi, central Louisiana, southern Oklahoma, and northern Texas. Again, based on ray tracing, Nos. 4, 5, 6, and 8 gravity waves originated from the wave sources of the convective systems of the cloud belt in area A; the No. 13 gravity waves were from area B; and No. 2, 11, 16, 17, and 18 gravity waves were from area C, shown in Figure 6.

Finally, one hour before or about the time of the tornado

touchdown (Figure A-5 and Table B-5), 19 gravity waves were detected in southeastern Kansas, southern Missouri, Arkansas, Oklahoma, and northern Texas. Again, based on ray tracing, Nos. 1 and 6 gravity waves originated from the convective system of the cloud belt in area A; Nos. 3 and 9 gravity waves were from area B; and the No. 15 gravity wave was from area C, shown in Figure 6. Figure 11 shows another two sample ray tracings, IV and V, for Nos. 1 and 9 gravity waves illustrated in Table B-5, respectively. The No. 1 gravity wave propagated from the wave source of the convective cloud system at area A; while the No. 9 gravity wave originated from area B and traveled to the location of waves detected at north central Texas.

Based on the results of ray tracing computation for the determination of wave source locations, most of the gravity waves, in which we are particularly interested in the contribution to the wave-induced convection, were excited by the convective systems of the cloud belts in the area between the three lines of the low pressure trough, (marked as a rectangle enclosed by the dashed lines, in Figure 6).

4. Gravity Wave-Induced Convection

Large amplitude gravity waves have been linked to the onset of convective storm systems. Large amplitude gravity waves are animportant mechanism for the initiation of severe convection (Uccellini, 1975). Wavelength, wave frequency, and phase velocity of the gravity waves, as shown in Section 3 of this paper, in addition to the amplitude of waves, can be computed from microbarograph data.

Thus, the vertical velocity of the gravity wave-induced convection can be computed from the wave intensity (amplitude of the surface pressure perturbation), wavelength, and phase velocity of gravity waves, together with the average velocities of horizontal wind (Uccellini, 1975; Eom, 1975). Gravity wave-induced convection at different altitudes can also be calculated by considering density ratios and average velocities of horizontal winds at different altitudes.

In this study, Eom's model is employed for the calculation of convection initiated by the gravity waves (Uccellini, 1975). The vertical displacement induced by each gravity wave at 3 and 12 km heights in the area of coverage, shown in Tables 1 to 5, have been computed. The area of coverage for gravity waves is a combined area of three microbarogram stations from which a cross correlation analysis is employed to compute the characteristics of gravity waves (Hung et al., 1978). In cases where there were overlapping areas of coverage in the wave detection, contributing to the wave-induced convection, linear sperposition has been used to add up the contribution of the vertical displacement made by each gravity wave within the areas of coverage. Both the lifting condensation level (LCL) and the level of free convection (LFC) were calculated from Figure 3. Thus, the geographical distribution of the amount of vertical displacement induced by the gravity waves for air parcels at the level of free convection and above can be obtained through the computation of vertical displacement from 3 to 12 km heights.

Figures 12, 13, 14, 15, and 16 show the geographical distribution

of the vertical velocity at 3 km height, induced by the gravity waves shown in Figures A-1, A-2, A-3, A-4 and A-5 of Appendix A, respectively. The contribution to vertical motion made by each gravity wave and the area of coverage in terms of the locations of microbarogram stations, at 3 km and 12 km heights, is shown in Tables B-1 through B-5.

Figure 12 shows that about 5 to 6 hours before the touchdown of the tornado, there was very weak vertical motion at the 3 km height, in the convective system of the cloud belt at area C (illustrated in the radar summary at Figure 6). Table B-1 of Appendix B indicates that the major contribution to convection was induced by the No. 3 gravity waves (see geographical location at Figure A-1) having 35 minute wave periods. Based on ray tracing computation, the No. 3 gravity waves were excited ty the convective cloud systems located at area C (illustrated in the radar summary in Figure 6). At this time period, mesoscale convection based on the gravity wave-induced convection was not detected at the location of the tornado touchdown in the south central Oklahoma and north central Texas area.

About 4 to 5 hours before the touchdown of the tornado (Figure 13), a vertical motion of 0.1 m/s was induced at 3 km height, in the area of south central Oklahoma and north central Texas. Table B-2 of Appendix B indicates that the major contribution to convection was induced by the No. 12 gravity waves (see geographical location at Figure A-2) with 35 minute wave periods which were excited by the convective cloud systems located in area A shown in Figure 6, based on ray tracing computation. This convection started to push up the air

mass in the area of interest, at south central Oklahoma and north central Texas, to the level of free convection (2.4 km height, see Figure 3 for detail) and the above heights. There was no cloud formation shown in satellite imagery in the area of south central Oklahoma and north central Texas, at this period of time.

About 3 to 4 hours before the touchdown of the tornado (Figure 14), a vertical convection of 0.2 m/s was initiated at 3 km height, in the area of central and northern Texas. Table B-3 of Appendix B indicates that the major contribution to convections was initiated by the No. 6, and a small portion by the No. 7, gravity waves (see geographical locations at Figure A-3) which were all excited by the convective cloud systems located in area A shown in Figure 6, based on ray tracing computation. Both of the gravity waves had a wave period of 20 minutes, and these gravity waves were responsible for the initiation of major convection shown in Figure 14 (see Tables B-1 through B-5 of Appendix B) for the computed values of the vertical velocity of convective activity induced by the gravity waves).

Based on more than 100 cases of gravity waves associated with severe convective storms detected at ionospheric heights when the overshooting cloud turrets started to penetrate above the tropopause, it was found that mesoscale gravity waves with wave periods of 10 to 20 minutes were dominant in the triggering of severe convective storms (Hung et al., 1979b; 1980, 1983; Hung and Smith, 1978; 1981; 1982; 1983). The result from the present study, that gravity waves with wave periods of 20 minutes provided a major contribution in the induced-convection (values of induced vertical velocity shown in

Tables B-1 through B-5) which, in turn, contributed to the initiation of mesoscale clouds that eventually developed into a severe convective storm, is in agreement with the ionospheric observation of mesoscale gravity waves. Both the satellite rapid scan imagery and the radar summary show that the convective clouds, located at south central Oklahoma, were formed during the later part of this data smpling time when the convective motions initiated by the gravity waves pushed up the air mass to the free condensation levels and started the cloud formation.

The area of maximum convection induced by the gravity waves at 3 km height, (Figure 14), did not exactly cover the touchdown location of Ardmore tornadoes. This is due to the fact that the cloud tower was tilted toward the northeastern direction resulting from the soughwest winds in the horizontal direction which also pushed the air mass moving along this direction. The motion of the air mass can be viewed and estimated from the satellite imagery (see Figure 7) which indicated that the convective cloud system developed and moved toward the northeastern direction with a velocity of 40 km/hr. This horizontal motion of the convective system made the area of maximum convection move toward the site of tornado touchdown at the moment of severe storm formation.

Comparison between Figures 14 and 6 show that there were no radar echoes at the location of the initial stage of maximum gravity wave-induced convection. This is due to the fact that the droplets are not viewed at the initial stage of convection, as shown in Figures 6 and 14. As we can see from satellite imagery, the convective cloud

started to form after 2300 GMT which was 30 minutes later than the radar echoes shown in Figure 6.

About 2 to 3 hours before the touchdown of the tornado (Figure 15), there was a vertical motion of 0.8 m/s at 3 km height, in the areas of southwestern Oklahoma, north central Texas, and southwestern Louisiana. Table B-4 of Appendix B indicates that the major contribution of convections was initiated by the No. 4 gravity waves (see geographical location at Figure A-4) with wave periods of 20 minutes. Based on ray tracing, the No. 4 gravity wave originated from the convective systems of the cloud belt in Area A, shown in Figure 6. During this period of time, satellite infrared imagery, shown in Figures 7-A, 7-B, and 7-C, showed a rapid growth of mesoscale clouds in the area of south central Oklahoma.

Finally, less than one hour before or about the time of the tornado touchdown, (Figre A-5), a vertical convection of 0.3 m/s was initiated at 3 km height in the area of north central Texas. Table B-5 of Appendix B indicates that the major contribution to induced vertical motion came from the No. 1 gravity waves (see geographical location at Figure A-5) with wave periods of 20 minutes. A comparison of Figures 15 and 16, shows that the vertical motion of the gravity wave-induced convection decreased from 0.8 to 0.3 m/s between the period 2245-0045 GMT, and the period 0000-0200 GMT. On the other hand, the momentum of the up-draft motion showed a tendency of increasing based on the satellite infrared imagery of the growth of cloud-tops (see Figure 7). This occurred even though the calculated result of the vertical convection induced by the gravity waves shows a

tendency of decreasing values for wave-induced convection.

Figure 17 shows the life cycle, formation, development and dissipation of Ardmore storm clouds derived from rapid-scan imagery of satellite observation, in terms of growth and collapse of cloud tops. This figure shows that the Ardmore storm clouds initiated at 2314 GMT, 29 April 1985 at the height of 4 km, grew quickly and penetrated above the tropopause in less than 20 minutes. The tropopause height was determined from rawinsonde data shown in Figure 3. The cloud top started to oscillate up and down and grew up to 13 km height at 0045 GMT. The cloud was finally collapsing with a high rate, in the altitude of 12.5 km at 0125 GMT. From inspection of Figures 12 through 16 and Figure 17 for the timing of gravity wave-induced convection and satellite observation of the life cycle of Ardmore storm clouds, the following conclusions can be drawn: (1) Gravity wave-induced convection started the vertical motion during the time period of 2015 to 2215 GMT, in the area of north central Texas and south central Oklahoma. (2) Once the vertical displacement induced by the gravity waves for air parcels pushed up above the level of free convection (2.4 km height), condensation occurred, and cloud formation was observed at 2314 GMT, at the height of 4 km. (3) The intensity of vertical displacement induced by the gravity waves increased continuously, and played the major role in the thrust mechanism of convection until the cloud top grew to the height of tropopause at 0000 GMT. (4) The act of initiating vertical displacement played by the gravity waves lost its major role after the cloud top of the storms penetrated above the tropopause. The

vertical displacement incuded by the gravity waves at the height of 12 km was computed for each gravity wave, and is illustrated in Tables B-1 to B-5 of Appendix B. To show an example, Figure 18 illustrates gravity wave-induced convection at 12 km height, during the period of data sampling time 2245 GMT, 29 April 1985 to 0045 GMT, 30 April 1985. This figure shows that a strong initiation of convection with a maximum vertical velocity of 2.5 m/s was induced in the area of north central Texas and south central Oklahoma.

In this case, it is interesting to note that the gravity waves that contributed to the wave-induced cnvection are those with phase speeds in the range of 18 to 120 m/s. In particular, the gravity waves that contributed most effectively to the wave-induced convection are those with phase speeds below 60 m/s. In other words, the gravity waves with phase speeds higher than 120 m/s made very little contribution to the wave-induced convection and can therefore be ignored.

Gravity wave-induced vertical displacements at 3 km and 12 km heights from 5 to 6 hours before touchdown of the tornado, to the time of tornado touchdown have been computed based on the available microbarograph data. It is interesting to study the role of gravity waves in wave-induced convection contributing to the initial, formation, developing and mature stages of storm cloud life cycle. In other words, we are interested in seeking the fractions of convections which were contributed by the gravity wave-induced convection. It was proposed to perform the numerical modeling of Ardmore storm clouds in which the mesoscale convergence was assumed.

The purpose was to study the evolution of convection and the time-dependent variation of convection in storm cloud formation and development, and to investigate in what degree contributions were made by the wave-induced convection by comparing convection obtained from cloud modeling and that induced by gravity waves.

Numerical simulation of the storm cloud formation was carried out with the initial input from rawinsonde data shown in Figure 3 for consideration of the fractions of convection induced by the gravity waves in comparison with the other mechanisms which have contributed to the convective activity. The cloud model, employed in the calculation, was designed to study mesoscale cloud formation and development in which mesoscale convergence was input to the convective scale domain; convergence was superimposed in the lower levels and divergence in the upper levels (Orville, 1965; Orville and Kopp, 1977; Orville et al., 1984). With the inclusion of the ice phase (Orville and Kopp, 1977) and realistic turbulence of eddy coefficient for momentum, eddy diffusion coefficient for water vapor, eddy coefficient for heat flux, etc. (Chen and Orville, 1980; Orville et al., 1984) into the model, we were able to simulate the development of mesoscale severe storms (Hung and Tsao, 1987; 1988). This program is available and installed on Cyber 205 at NASA Goddard Space Flight Center, Greenbelt, Maryland, and CRAY X-MP at NASA Marshall Space Flight Center, Huntsville, Alabama. A detailed description of the numerical simulation of Ardmore, Oklahoma storm cloud formation is in preparation and will be presented in the subsequent paper (Hung and Tsao, 1989). A detailed setup of cloud modeling, including setting

of grid points, selection of initial input data from sounding, numerical scheme, etc., for this cloud modeling, are discussed in Hung and Tsao (1987; 1988).

Results based on cloud modeling are included in this paper in order to have a better comparison between cloud initiation and formation, based on gravity wave-induced conveciton. In particular, the fractions of convection induced by gravity waves compared to other mechanisms which support convection. Figure 19 shows the instantaneous maximum vertical velocity of up-draft motion of Ardmore, Oklahoma, storm clouds based on numerical simulation. The high and low values of the instantaneous maximum vertical velocity were in phase with the growth and collapse of cloud tops observed from satellite rapid-scan imagery, shown in Figure 17. In comparison between vertical displacement induced by gravity waves at 12 km altitude, shown in Tables B-1 to B-5 of Appendix B, and Figure 19 for the values of vertical velocity, the following conclusions can be drawn: (1) Gravity waves were responsible for more than 80% of the mechanism which induced vertical displacement of air parcels before 0015 GMT, approximately 40 minutes before the formation of severe storms; (2) Gravity waves decreased gradually as the 80% contributor for the initiation of vertical displacement to less than 30% contributor at 0035 GMT, approximately 20 minutes before the formation of severe storms; and (3) The contributions of gravity wave-induced convection were less than 10% for the total vertical displacement produced at the time of severe storm formation.

5. Conclusions

In this study, we did not rule out the contribution of the initiation of convection made by other mechanisms, such as low-level convergence along mesoscale boundary and others. What we discuss here is the kind of role gravity waves played in the wave-induced convection contributing to the formation and development of severe convective storms.

The Ardmore, Oklahoma storm on 29-30 April 1985 was chosen as a case study in this investigation. Six hours of microbarograph data, ending at the liftoff time of the tornado, from all the available microbarogram stations in the south central United States were used in the analysis. We have excluded gravity waves from synoptic and large scale systems, and we are interested only in the mesoscale gravity waves with periods from 5 to 60 minutes. During the period of interest, seventy-six gravity waves were detected in this area. Less than 30% of the gravity waves detected were responsible for the major contribution in wave-induced vertical displacement. In particular, gravity waves with phase speeds higher than 120 m/s made almost no contribution to wave-induced convections. The waves which provided a major contribution in Wave-induced convection are listed in the last column of Tables B-1 to B-5 of Appendix B. The ray tracing technique has been applied to trace the locations of wave sources. It was found that most of the large amplitude gravity waves responsible for the initiation of the largest vertical motion were excited by enhanced convective systems (see last column of Tables B-1 to B-5 of Appendix B for the locations of wave source based on ray tracing calculation).

Large amplitude gravity waves have been linked to the onset of convective storm systems. Eom's model has been used for the computation of vertical motion induced by each gravity wave at different altitudes (Uccellini, 1975). In this study, the vertical motion induced by all 76 gravity waves detected during the period of interest at different altitudes, from 3 to 12 km, have been computed and are shown in Tables B-1 through B-5 of Appendix B. At least five hours before the touchdown of the tornado, there were no mesoscale gravity waves with large amplitudes detected in the area of interest. Three to five hours before the touchdown of the tornado, very weak vertical motion was induced by the large amplitude gravity waves with wave periods of 35 minutes which were excited by the convective cloud systems at areas A, B, and C, shown in the radar summary at Figure 6. In this particular case, about 2 to 3 hours before the touchdown of the tornado, the mesoscale convective systems (located at the area A shown in Figure 6 based on ray tracing computation) generated large amplitude gravity waves with wave periods of 20 minutes which started to initiate convection in the area of central and northern Texas. Similar gravity waves with wave periods of 20 minutes have been detected at ionospheric heights for their dominance in the triggering of severe convective storms when the overshooting cloud tops start to penetrate above the tropopause (Hung et al., 1980; 1983; Hung and Smith, 1981). Based on computation of vertical motion induced by each gravity wave at different altitudes, from 3 to 12 km heights shown in Table B-3 of Appendix B, and the total amount of vertical motion induced by the corresponding gravity waves in the area shown in Figure

14, wave-induced convection provided a sufficient lifting, and the air masses were, thus, pushed up above the level of free convection (2.4 km height, see Figure 3 for detail) due to the strong convection initiated by the large amplitude gravity waves with 20 minutes wave periods. Formation of clouds is the result of the initiation of condensation which is evidenced from the satellite infrared imagery, shown in Figures 7 and 17, and the radar summary, shown in Figure 6.

Vertical velocity of convective motions induced by the large amplitude gravity waves provided a sufficient lifting, grew rapidly, and developed a tall convective cloud, as shown in Figures 7, 8, and 17. This vertical velocity of convective motions induced by the gravity waves reached the maximum value which contributed more than 80% of the total convection about 40 minutes before the production of the funnel clouds in this particular case, based on cloud model simulation for maximum vertical velocity shown in Figure 19. There are many mechanisms which can contribute to the initiation of vertical motion, and gravity wave-induced convection is one of these mechanisms.

In this study, it has been shown that gravity waves acted as a major contributor for the initiation, formation and development of mesoscale storm clouds among the other possible mechanisms of contribution in this particular case. It is quite obvious that hte contribution of induced convection, made by gravity waves for the development of mesoscale storm clouds, declines slowly during the further lifetime of a storm system once it has been initiated, and is replaced by the other forms of dynamical forces as the major driving

mechanisms which maintain the development of convection through adding substantial moisture to the system. These additional mechanisms, including convergence at higher levels, thermal forcing and others, eventually pushed up clouds to be a severe storm in the last stage of cloud development, and replaced the role played by the gravity waves in the initial and early stage of convection based on the calculations made in Table B-5 of Appendix B in comparison with satellite imagery shown in Figure 7 and 17, and also cloud model simulation for maximum vertical velocity shown in Figure 19. Gravity waves are excited continuously, as long as there is a convective system. The existence of large amplitude gravity waves provides an important mechanism for the initiation of severe convection if the instability conditions of the lapse rate of potential temperature and low level high moisture concentration support the vertical displacemlent.

Acknowledgement

The authors thank the Office of Space Science and Applications, the National Aeronautics and Space Administration Headquarters for the research grant NAGW-1165 which supported the present research.

References

Adrian, R. J., 1975: Turbulent convection in water over ice. Journal of Fluid Mechanics, 69, 753-781.

Bluestein, H. B., and M. H. Jain, 1985: Formation of mesoscale lines of precipitation: severe squall lines in Oklahoma during the spring. Journal of Atmospheric Sciences, 42, 1711-1732.

Bluestein, H. B., and C. R. Parks, 1983: A synoptic and photographic climatology of low preccipitation severe thunderstorms in the Southern Plains. Monthly Weather Reviews, 111, 2034-2046.

Chen, C. H. and H. R. Orville, 1980: Effects of mesoscale convergence on cloud convection. Journal of Applied Meteorology, 19, 256-274.

Colby, F. P., Jr., 1984: Convective inhibition as a predictor of the outbreak of convection in AVE-SESAME II. Monthly Weather Reviews, 112, 2239-2252.

Curry, M. J., and R. C. Murty, 1974: Thunderstorm-generated gravity waves. Journal of Atmospheric Sciences, 31, 1402-1408.

Deardorff, J. W., G. W. Willis, and D. K. Lilly, 1969: Laboratory investigation of non-steady penetrative convection. Journal of Fluid Mechanics, 35, 7-31.

Dunkerton, T. J., 1982: Stochastic parameterization of gravity wave stresses. Journal of Atmospheric Sciences, 39, 1711-1725.

Einaudi, F., and D. P. Lalas, 1975: Wave-induced instabilities in an atmosphere near saturation. Journal of Atmospheric Sciences, 32, 536-547.

Eom, J. K., 1975: Analysis of the internal wave occurrence of 19 April

1970 in the Midwest. Monthly Weather Reviews, 103.

Gossard, E. E., and W. B. Sweezy, 1974: Dispersion and spectra of gravity waves in the atmosphere. Journal of Atmospheric Sciences, 31, 1540-1548.

Hung, R. J., J. C. Dodge, and R. E. Smith, 1983: The life cycle of a tornadic cloud as seen from a geosynchronous satellite. American Institute of Aeronautics and Astronautics Journal, 21, 1217-1224.

Hung, R. J., and J. P. Kuo, 1978: Ionospheric observation of gravity waves associated with Hurricane Eloise. Journal of Geophysics, 45, 67-80

Hung, R. J., T. Phan, and R. E. Smith, 1978: Observation of gravity waves during the extreme tornado outbreak of 3 April 1974. Journal of Atmospheric and Terrestrial Physics, 40, 831-843.

Hung, R. J., T. Phan, and R. E. Smith, 1979a: Case studies of gravity waves associated with isolated tornadic storms on January 13, 1976. Journal of Applied Meteorology, 18, 460-466.

Hung, R. J., T. Phan, and R. E. Smith, 1979b: Coupling of ionosphere and troposphere during the occurrence of isolated tornadoes on November 20, 1973. Journal of Geophysical Research, 84, 1261-1268.

Hung, R. J., T. Phan, D. C. Lin, R. E. Smith, R. R. Jayroe, and G. S. West, 1980: Gravity waves and GOES IR data study of an isolated tornadic storm on 29 May 1977. Monthly Weather Reviews, 108, 456-464.

Hung, R. J., and R. E. Smith, 1978: Ray tracing of gravity waves as a

possible warning system for tornadic storms and hurricanes. Journal of Applied Meteorology, 17, 3-11.

Hung, R. J., and R. E. Smith, 1981: Ionospheric remote sensing of medium scale gravity waves and tornadic storms. Il Nuovo Cimento, 4C, 339-358.

Hung, R. J., and R. E. Smith, 1982: Remote sensing of tornadic storms from geosynchronous satellite infrared digital data. International Journal of Remote Sensing, 3, 69-81.

Hung, R. J., and R. E. Smith, 1983: Remote sensing of Arkansas tornadoes on 11 April 1976 from a satellite, a balloon and an ionospheric sounder array. International Journal of Remote Sensing, 4, 617-630.

Hung, R. J., and Y. D. Tsao, 1987: Study of prestorm environment by using rawinsonde and satellite observations. International Journal of Remote Sensing, 8, 1123-1150.

Hung, R. J., and Y. D. Tsao, 1988: Satellite remote sensing and cloud modeling of St. Anthony, Minnesota storm clouds and dew point depression. Annales Geophysics, 6, 453- 462.

Hung, R. J., and Y. D. Tsao, 1989: Satellite infrared remote sensing and numerical simulation of Ardmore, Oklahoma storm clouds. International Journal of Remote Sensing, 10, in press.

Hung, R. J., Y. D. Tsao, D. L. Johnson, A. J. Chen, C. H. Lin, J. M. Cheng, and C. M. You, 1988: VHF radar remote sensing of atmospheric parameters over Taiwan during the time period of Typhoon Wayne. International Journal of Remote Sensing, 9, 477-493.

Hung, R. J., Y. D. Tsao, D. L. Johnson, A. J. Chen, C. H. Lin, and J. J. Pan, 1989: Observation of VHF radar on mesospheric and HF Doppler sounder on thermospheric density disturbances caused by typhoons and convective storms in the western Pacific area. Journal of Spacecraft and Rockets, 26, in press.

Lindzen, R. S., 1981: Turbulence and stress due to gravity waves and tidal breakdown. Journal of Geophysics Research, 86, 9707-9714.

Lindzen, R. S., and J. Forbes, 1983: Trubulence originating from convectively stable internal waves. Journal of Geophysical Research, 88, 6549-6553.

Matsumoto, S., and T. Akiyama, 1969: Some characteristic features of the heavy rainfalls observed over western Japan on 9 July 1967, I, Mesoscale structure and short period of pulsation. Journal of Meteorological Society of Japan, 47, 255-266.

Moncrieff, M. W., and J. S. A. Green, 1972: The propagation and transfer properties of steady convective overturning in shear. Quarterly Journal of Royal Meteorological Society, 98, 336-352.

Moncrieff, M. W. and M. J. Miller, 1976: The dynamics and simulation of tropical cumulonimbus and squall lines. Quarterly Journal of Royal Meteorological Society, 373-394.

National Climate Data Center, 1985: Storm Data, 27, 4-5.

Orville, H. D., 1965: A numerical study of the initiation of cumulus clouds over mountain terrain. Journal of Atmospheric Sciences, 22, 684-699.

Orville, H. D., R. D. Farley, and J. H. Hirsch, 1984: Some surprising results from simulated seeding of stratiform-type clouds,

Journal of Climate and Applied Meteorology, 23, 1585-1600.

Orville, H. D., and F. J. Kopp, 1977: Numerical simulation of the life history of hailstorm. Journal of Atmospheric Society, 34, 1596-1618.

Rottger, J., 1977: Travelling disturbance in the equatorial ionosphere and their association with penetrative cumulus convection. Journal of Atmospheric and Terrestrial Physics, 39, 987-998.

Stull, R. B., 1976: Internal gravity waves generated by penetrative convection. Journal of Atmospheric Sciences, 33, 1279-1286.

Townsend, A. A., 1964: Natural convection in water over an icy surface. Quarterly Journal of Royal Meteorological Society, 90, 248-259.

Uccellini, L. W., 1975: A case study of apparent gravity waves initiation of severe convective storms. Monthly Weather Reviews, 103, 497-513.

Weisman, M. L. and J. B. Klemp, 1982: The dependence of numerically simulated convective storms on vertical wind shear and buoyancy. Monthly Weather Reviews, 110, 504-520.

Willis, G. E., and J. W. Deardorff, 1974: A laboratory model of the unstable planetary boundary layer. Journal of Atmospheric Sciences, 31, 1292-1307.

Figure Captions

Figure 1. Geographical distribution of surface meteorological data, including isobars (with a unit of mb), axes of low pressure trough, and low and high pressure centers in the United States, at 0000 GMT, 30 April 1985.

Figure 2. Geographical distribution of surface moisture content (mixing ratio, with a unit of g/kg) in the area of south central United States, at 0000 GMT, 30 April 1985.

Figure 3. Vertical temperature and dew point temperature profiles in a Skew T, log P diagrams for Oklahoma City, Oklahoma at 0000 GMT, 30 April 1985, from rawinsonde data.

Figure 4. The 850 mb (height in gpdam) weather map in the United States and surrounding areas at 0000 GMT, 30 April 1985.

Figure 5. Geographical distribution of surface divergence, in the area of south central United States, at 0000 GMT, 30 April 1985.

Figure 6. Radar summary of central United States at 2235 GMT, 29 April 1985. Shaded areas depict radar echos. Marked rectangular areas A, B, and C represent obvious main source regions of observed gravity waves.

Figure 7. Growth of mesoscale convective cloud, located at south central Oklahoma, during the time period from 2330 GMT, 29 April 1985 to 0200 GMT, 30 April 1985 based on satellite infrared imagery of GOES west.

Figure 8. Cloud-top temperature distribution of the convective cloud located at south central Oklahoma, at 0100 GMT, 30

convection initiated by the gravity waves during the data sampling time: 0000-0200 GMT, 30 April 1985, at 3 km height.

Figure 17. Life cycle of Ardmore storm clouds, based on rapid-scan imagery obtained from GOES.

Figure 18. Geographical distribution of vertical velocity (m/s) of convection initiated by the gravity waves during the data sampling time: 2245 GMT, 29 April 1985 to 0045 GMT, 30 April 1985, at 12 km height.

Figure 19. Evolution of instantaneous maximum vertical velocity of Ardmore, Oklahoma storm clouds, based on the results of cloud simulation with input data from rawinsonde data shown in Figure 2.

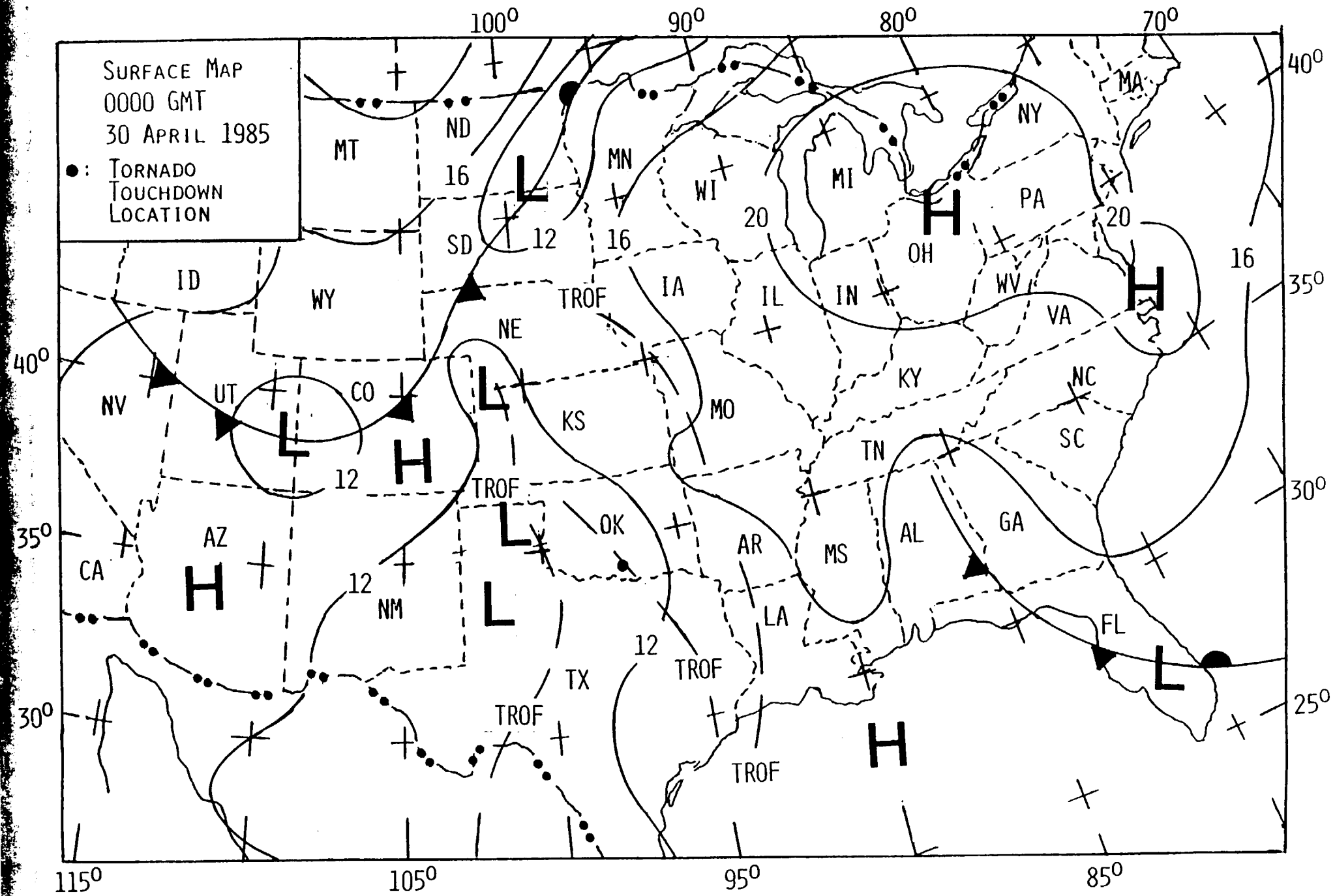
SURFACE MAP
0000 GMT
30 APRIL 1985
●: TORNADO TOUCHDOWN LOCATION
100°
90°
80°
70°
40°
35°
30°
25°
115°
105°
95°
85°
MT
ND
MN
WI
MI
NY
MA
PA
OH
WV
VA
ID
WY
SD
NE
IA
IL
IN
KY
NC
SC
NV
UT
CO
KS
MO
TN
AZ
CA
NM
OK
AR
MS
AL
GA
LA
TX
FL
TROF
16
20
12
L
H

FIG. 1

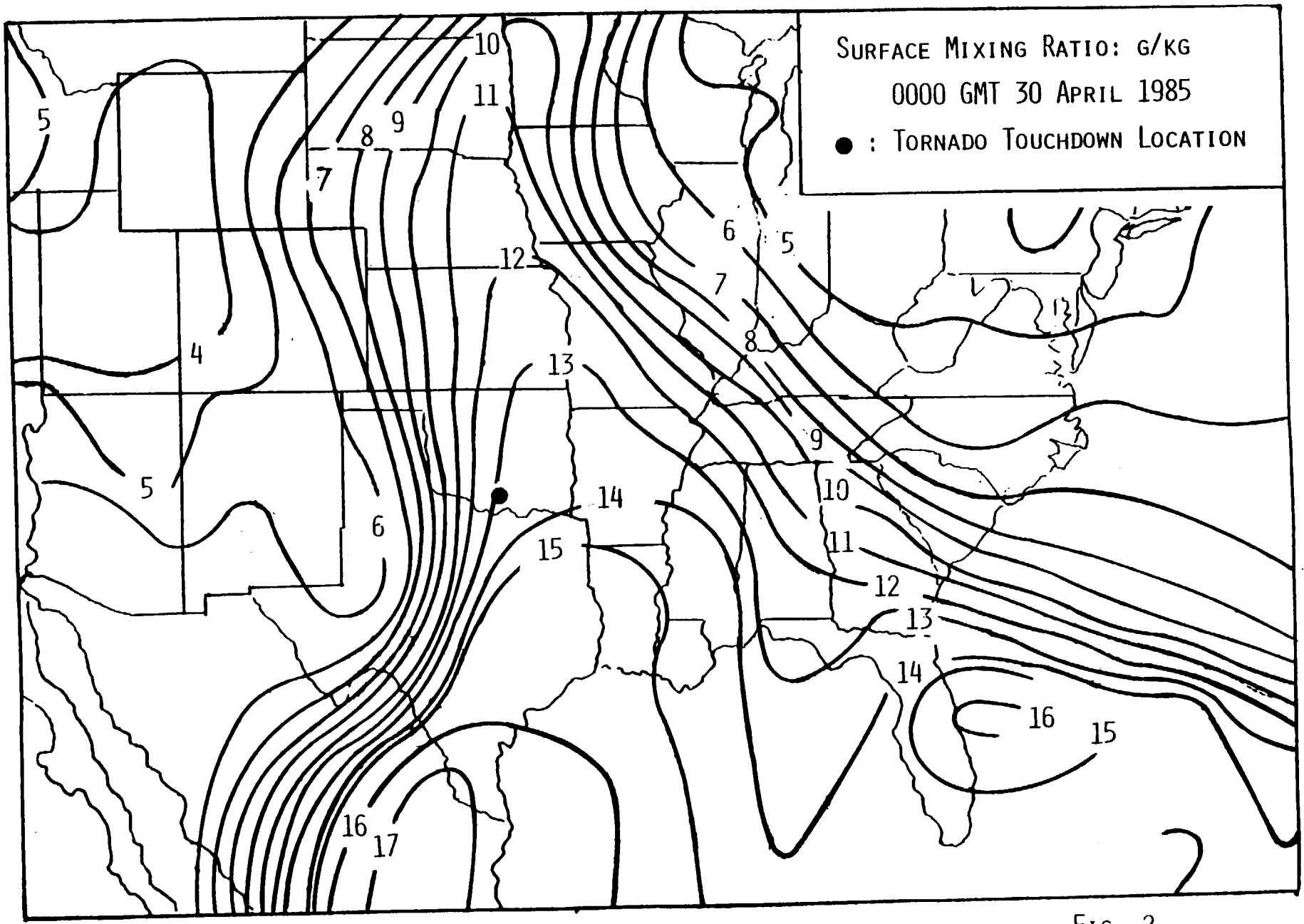
SURFACE MIXING RATIO: G/KG
0000 GMT 30 APRIL 1985
● : TORNADO TOUCHDOWN LOCATION
5
10
11
8
9
7
12
6
5
7
13
8
4
13
9
5
14
10
6
15
11
12
13
14
16
15
16
17

FIG. 2

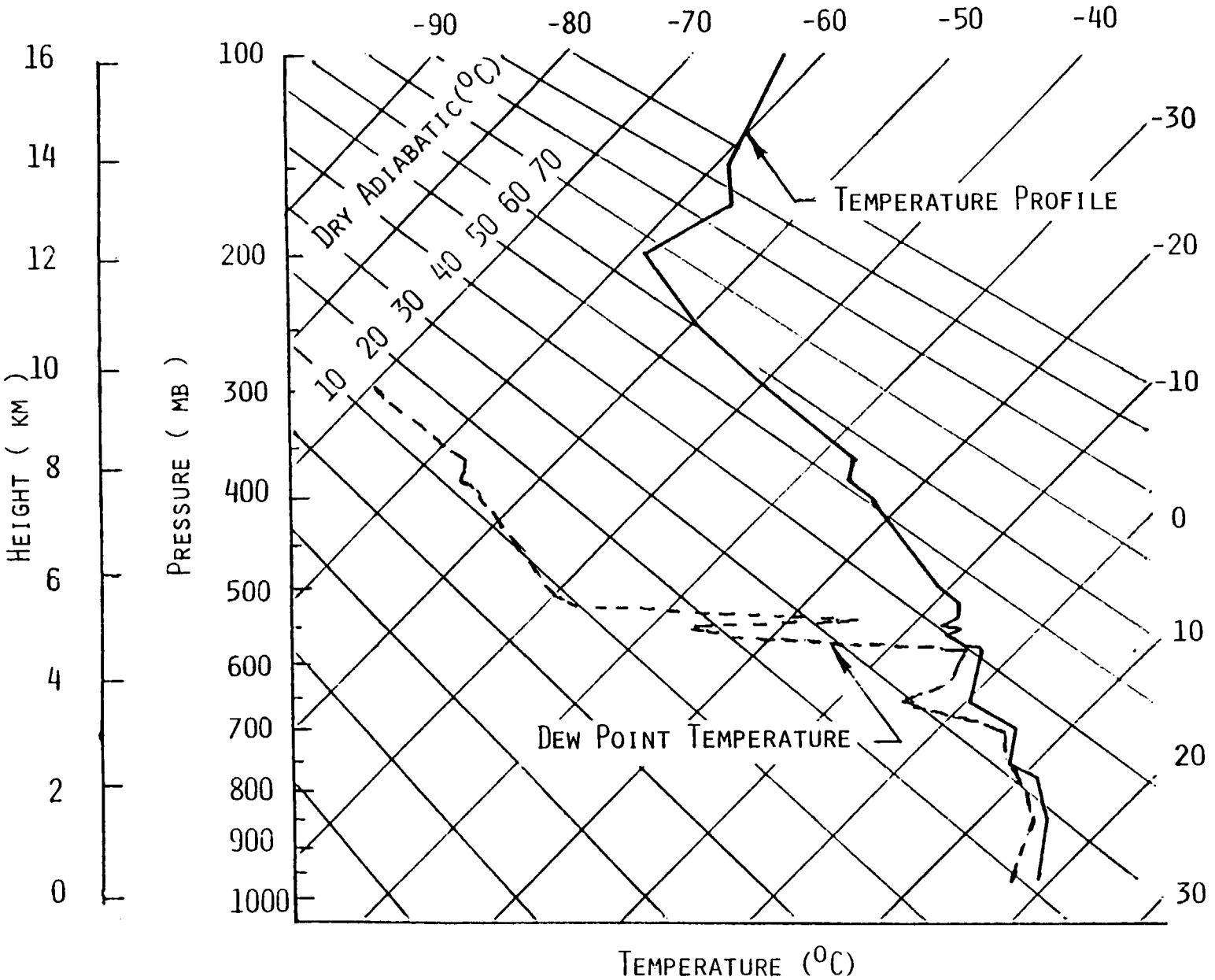
-90
-80
-70
-60
-50
-40
100
200
300
400
500
600
700
800
900
1000
16
14
12
10
8
6
4
2
0
-30
-20
-10
0
10
20
30
DRY ADIABATIC(°C)
10 20 30 40 50 60 70
TEMPERATURE PROFILE
DEW POINT TEMPERATURE
HEIGHT (KM)
PRESSURE (MB)
TEMPERATURE (°C)
OKLAHOMA CITY
OKLAHOMA
0000 GMT
APRIL 30, 1985

FIG. 3

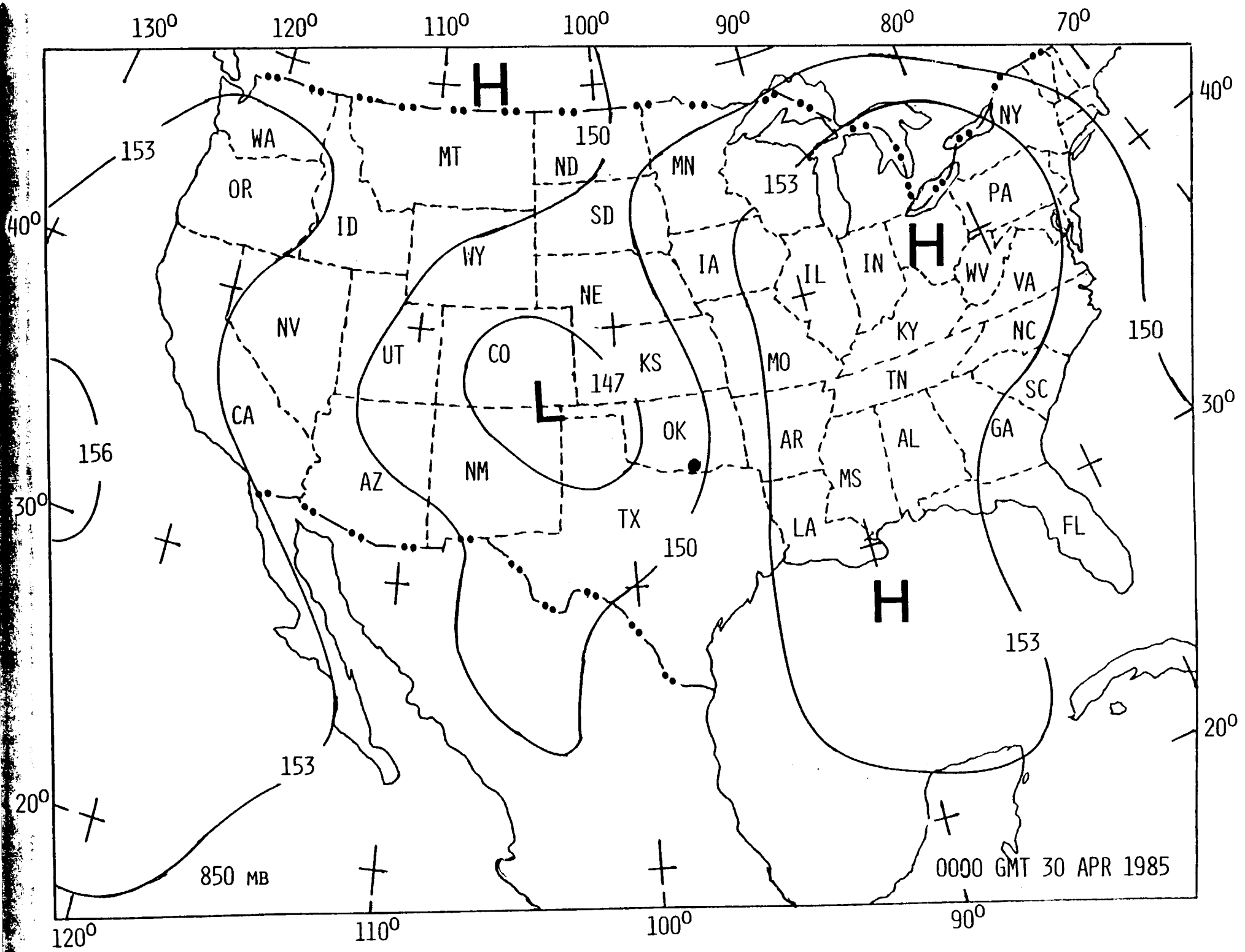
130°
120°
110°
100°
90°
80°
70°
40°
30°
20°
H
L
H
H
WA
OR
ID
MT
ND
MN
SD
WY
NE
NV
UT
CO
KS
CA
AZ
NM
TX
OK
MO
IA
IL
IN
WV
VA
KY
NC
TN
SC
AR
AL
GA
MS
LA
FL
NY
PA
153
150
147
156
850 MB
0000 GMT 30 APR 1985

FIG. 4

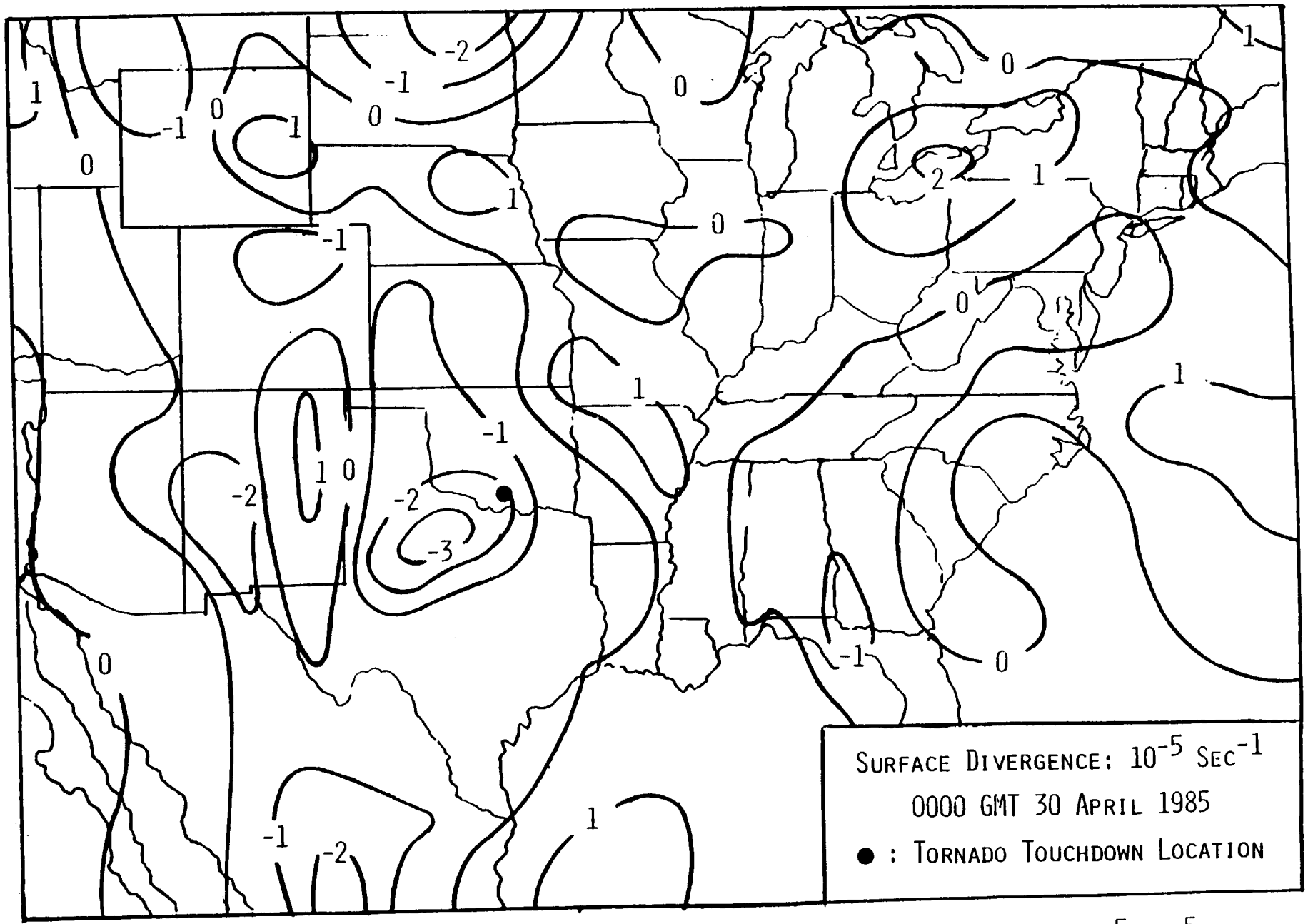
SURFACE DIVERGENCE: 10^{-5} SEC^{-1}
0000 GMT 30 APRIL 1985
● : TORNADO TOUCHDOWN LOCATION

FIG. 5

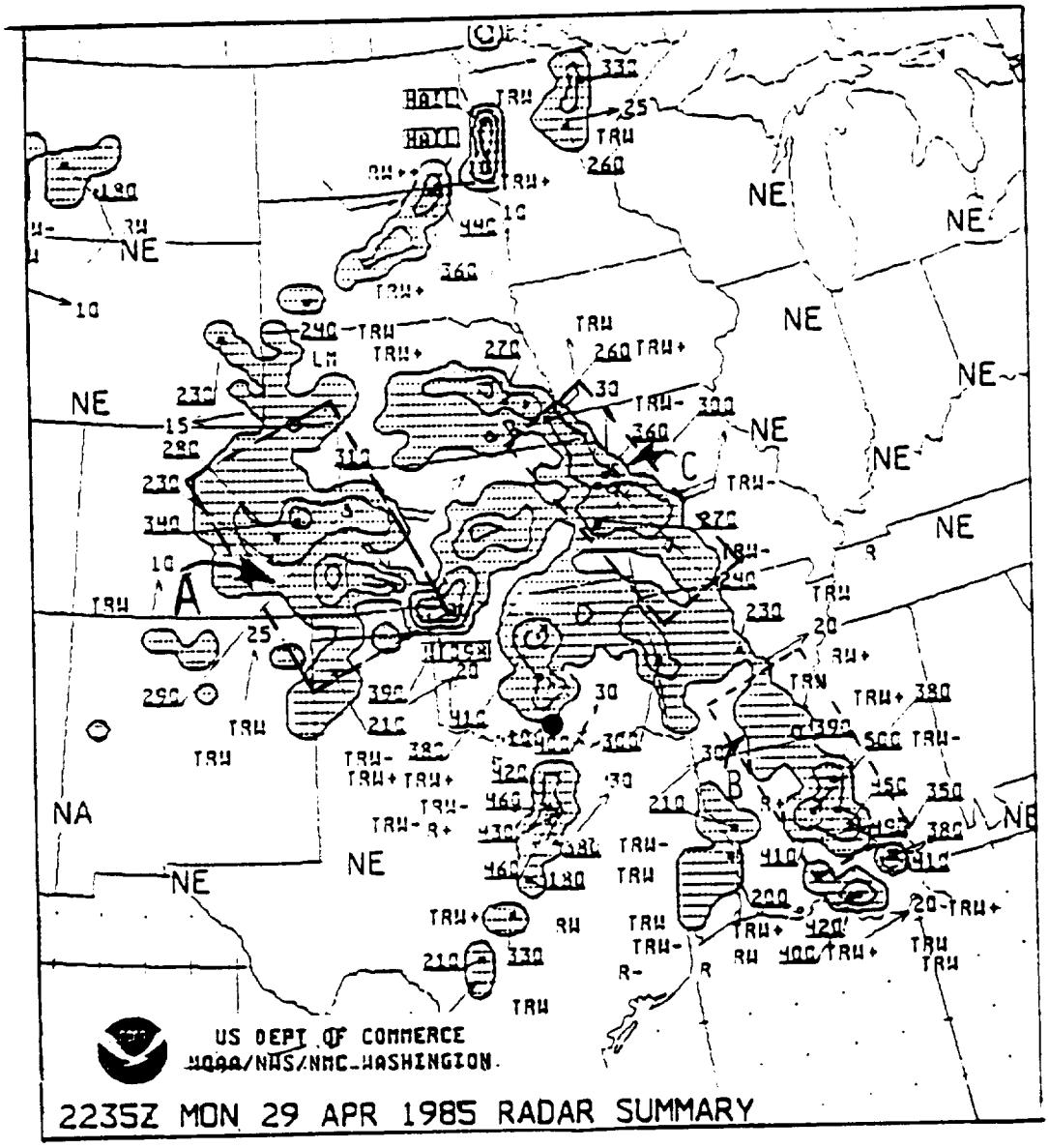

FIG. 6

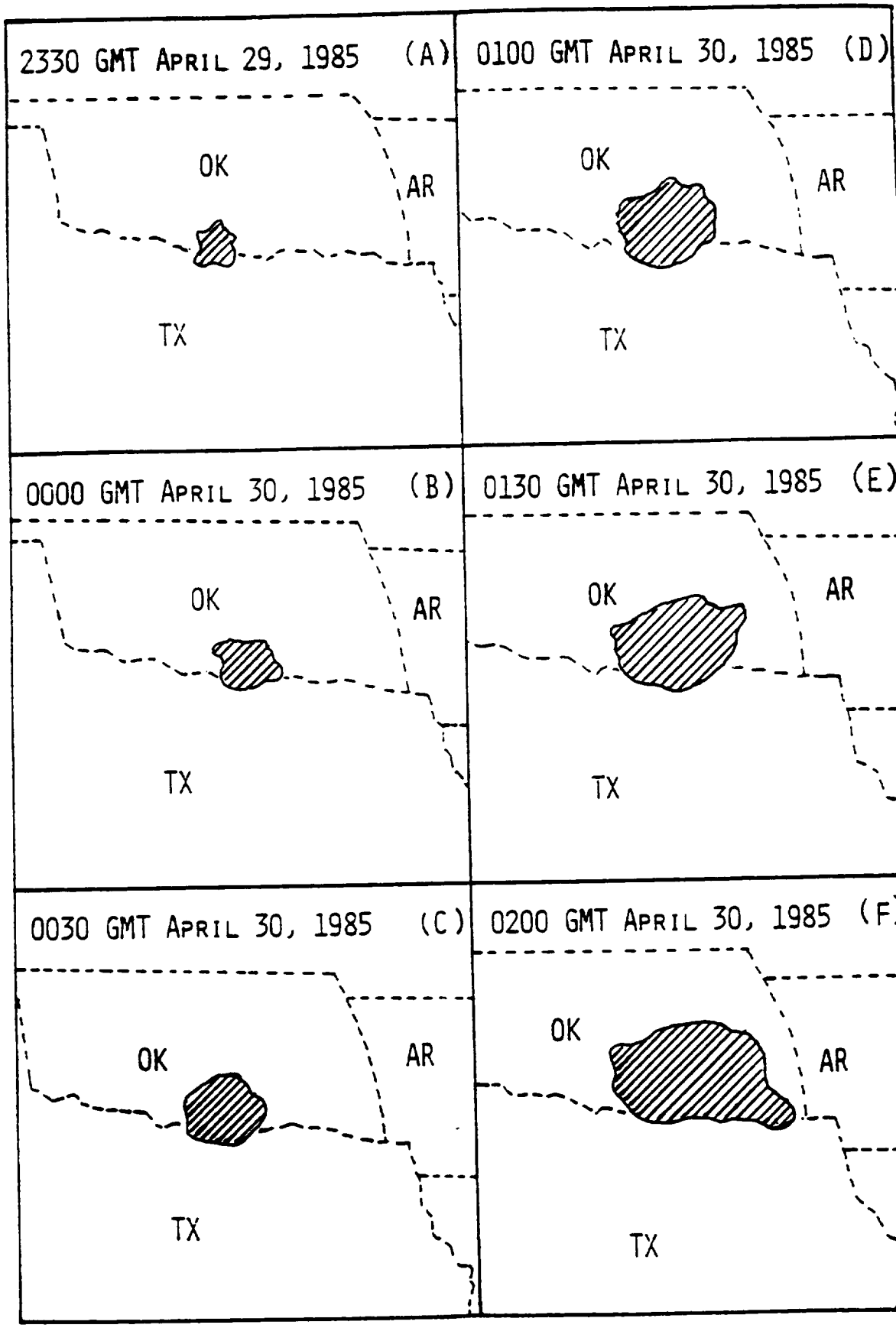
2330 GMT APRIL 29, 1985 (A)
OK
AR
TX
0100 GMT APRIL 30, 1985 (D)
OK
AR
TX
0000 GMT APRIL 30, 1985 (B)
OK
AR
TX
0130 GMT APRIL 30, 1985 (E)
OK
AR
TX
0030 GMT APRIL 30, 1985 (C)
OK
AR
TX
0200 GMT APRIL 30, 1985 (F)
OK
AR
TX

FIG. 7

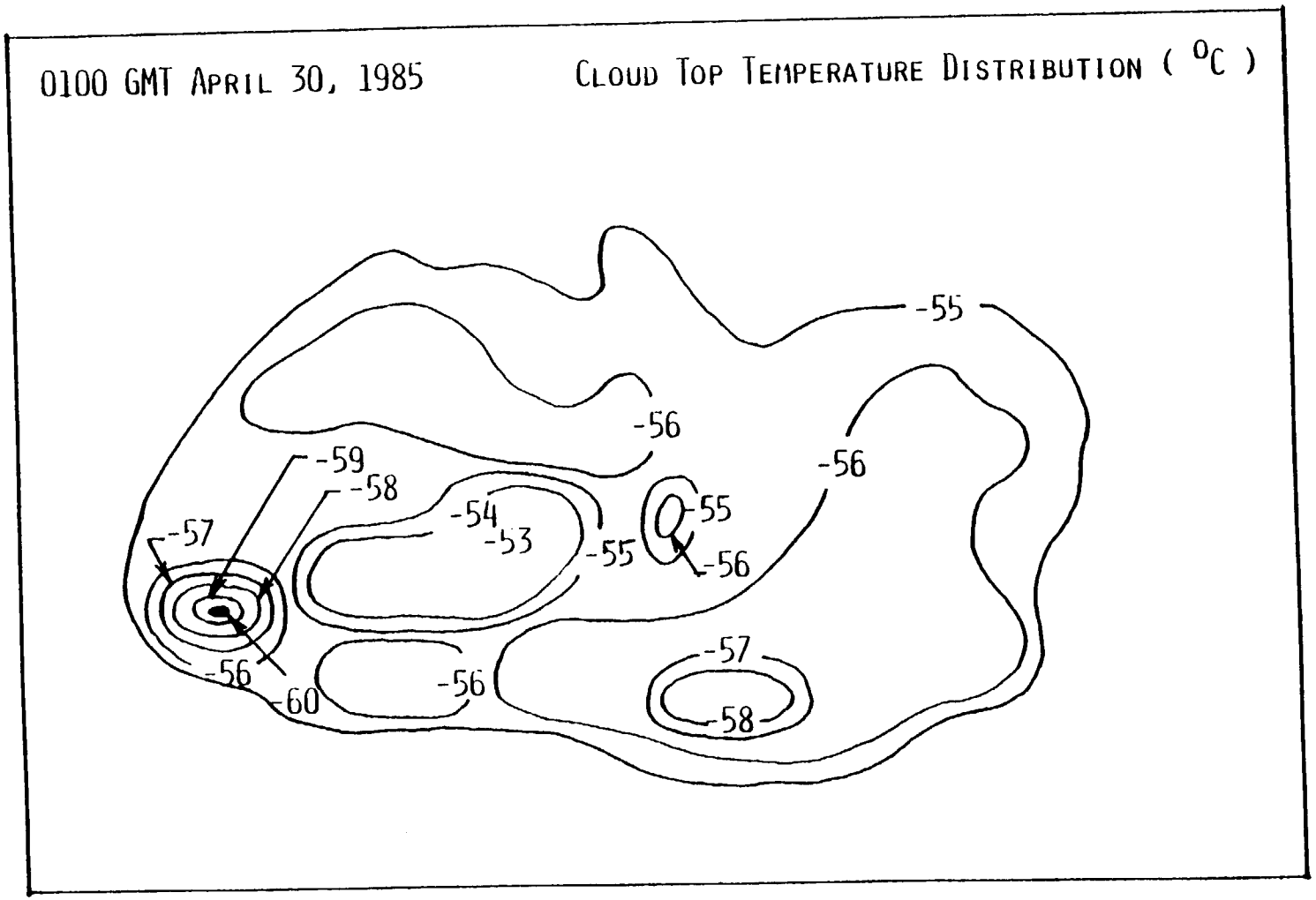
0100 GMT APRIL 30, 1985
CLOUD TOP TEMPERATURE DISTRIBUTION (°C)
-55
-56
-59
-58
-56
-57
-54
-53
-55
-55
-56
-57
-56
-60
-56
-58

FIG. 8

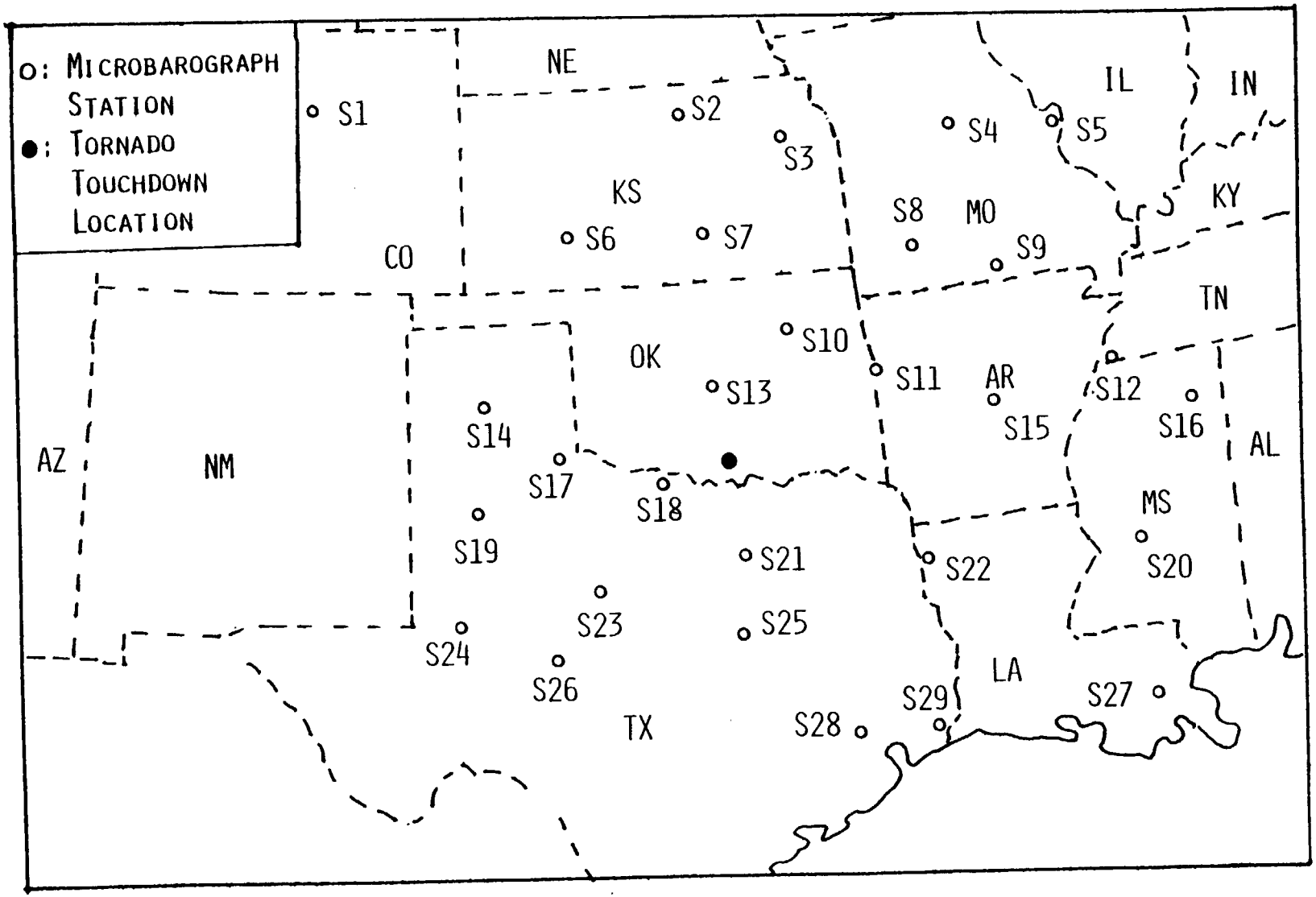
o: Microbarograph Station
●: Tornado Touchdown Location
NE
IL
IN
S1
S2
S3
S4
S5
KS
S8
MO
KY
S6
S7
S9
CO
TN
S10
OK
S11
AR
S12
S13
S14
S15
S16
AZ
NM
S17
S18
AL
MS
S19
S21
S22
S20
S23
S25
S24
LA
S26
S29
S27
TX
S28

Fig. 9

MICROBAROGRAPH DATA

2040-2155 GMT, 29 APRIL 1985

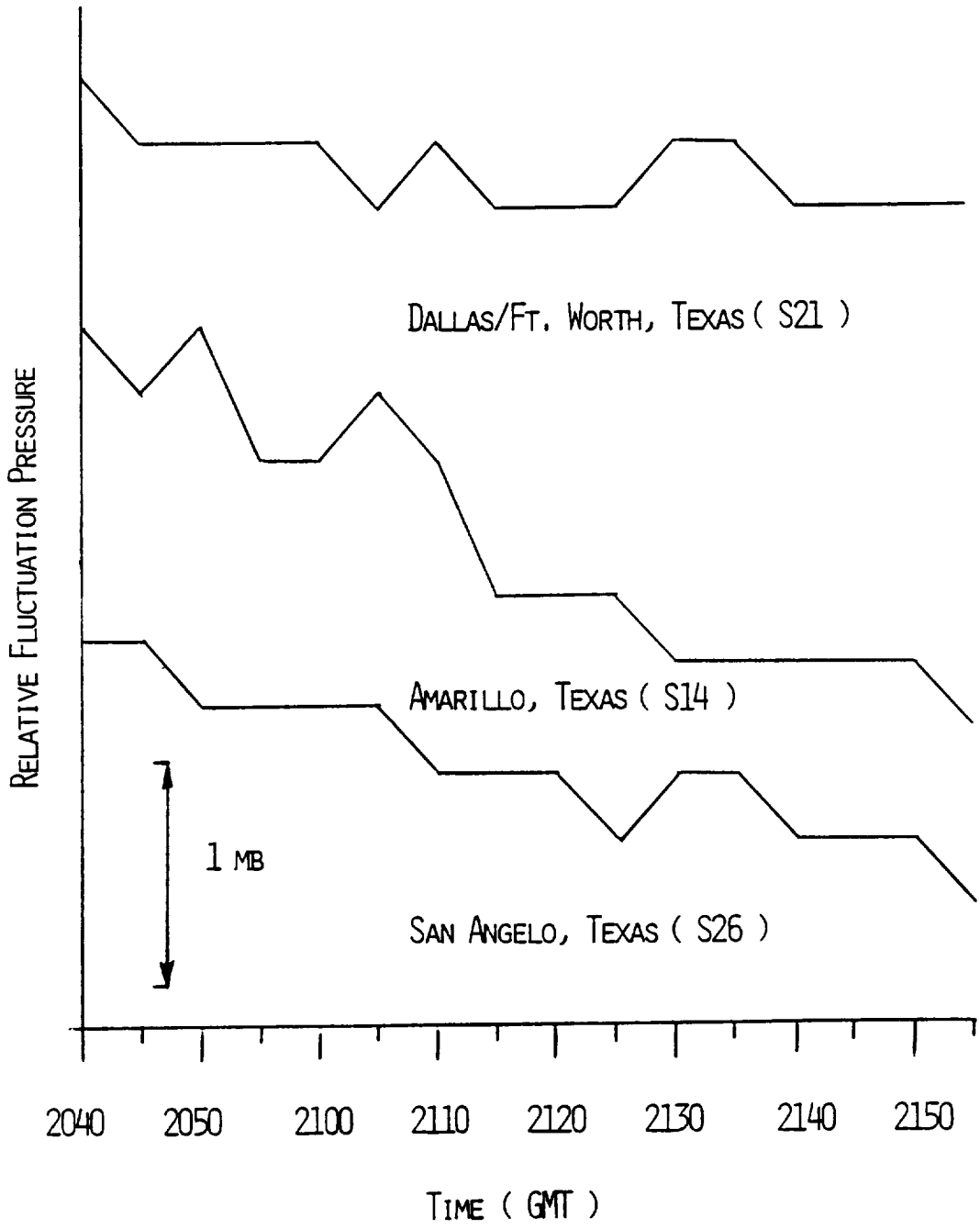

FIG. 10

SAMPLE OF RAY TRACING

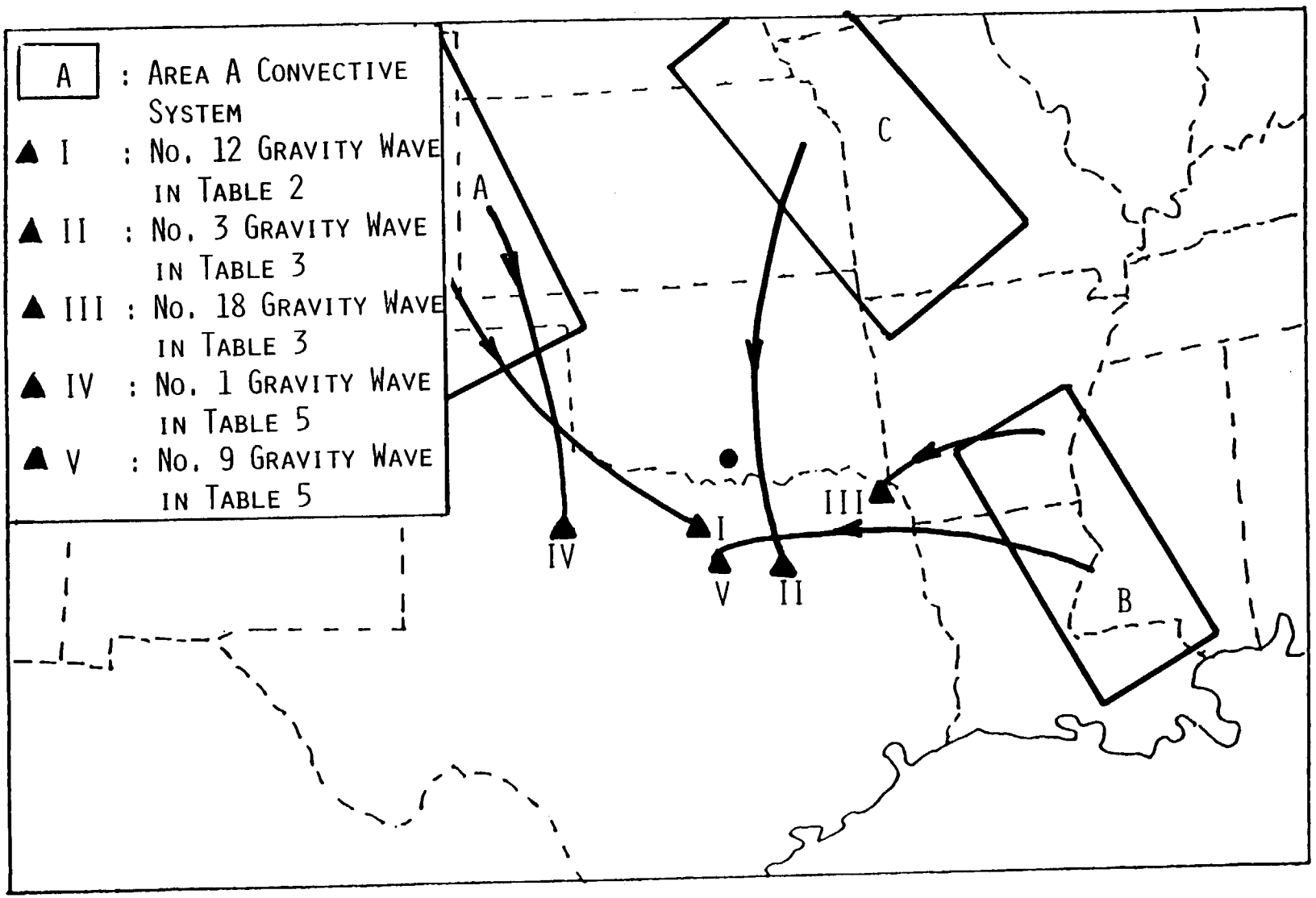

FIG. 11

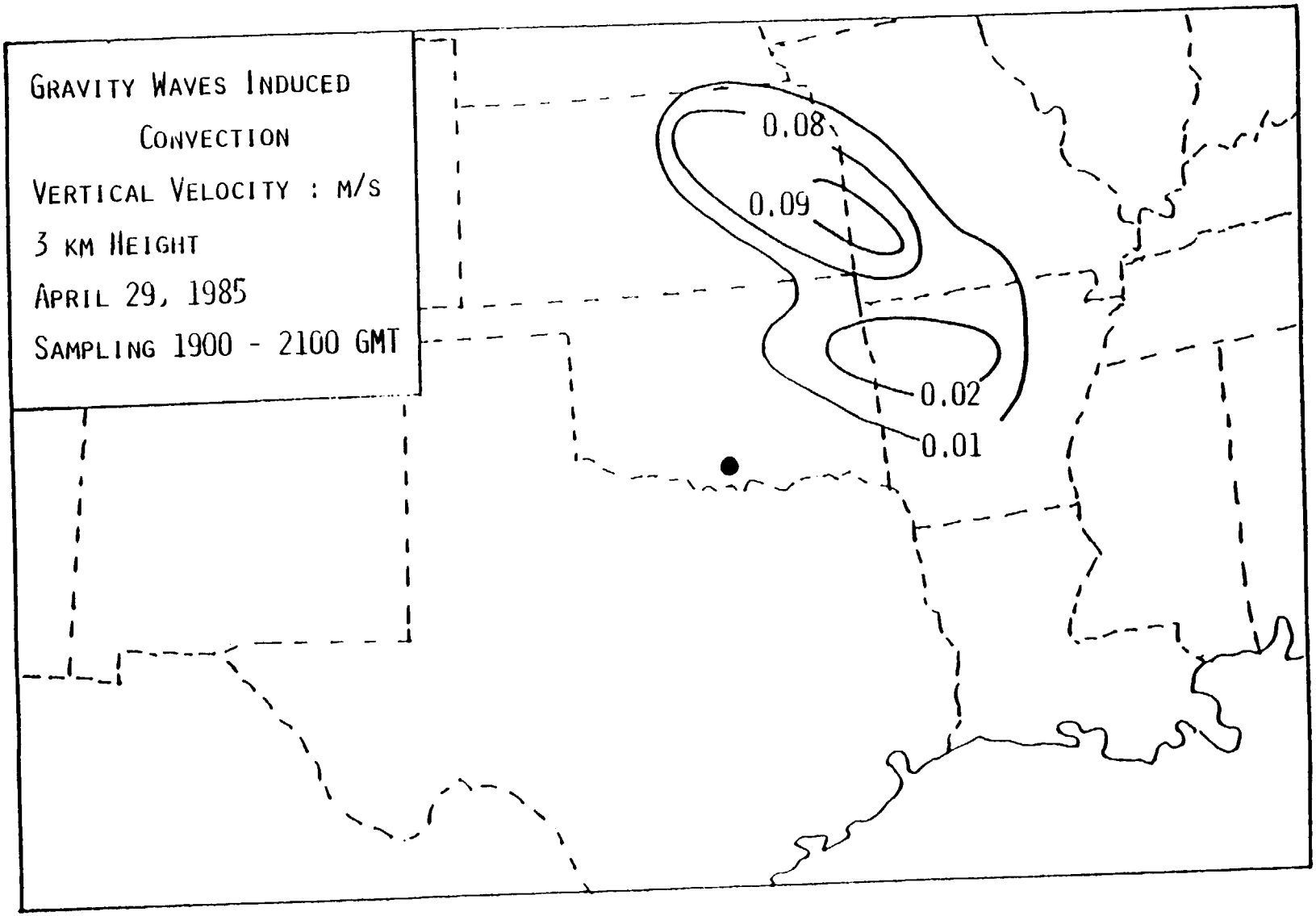
GRAVITY WAVES INDUCED
CONVECTION
VERTICAL VELOCITY : M/S
3 KM HEIGHT
APRIL 29, 1985
SAMPLING 1900 - 2100 GMT
0.08
0.09
0.02
0.01

FIG. 12

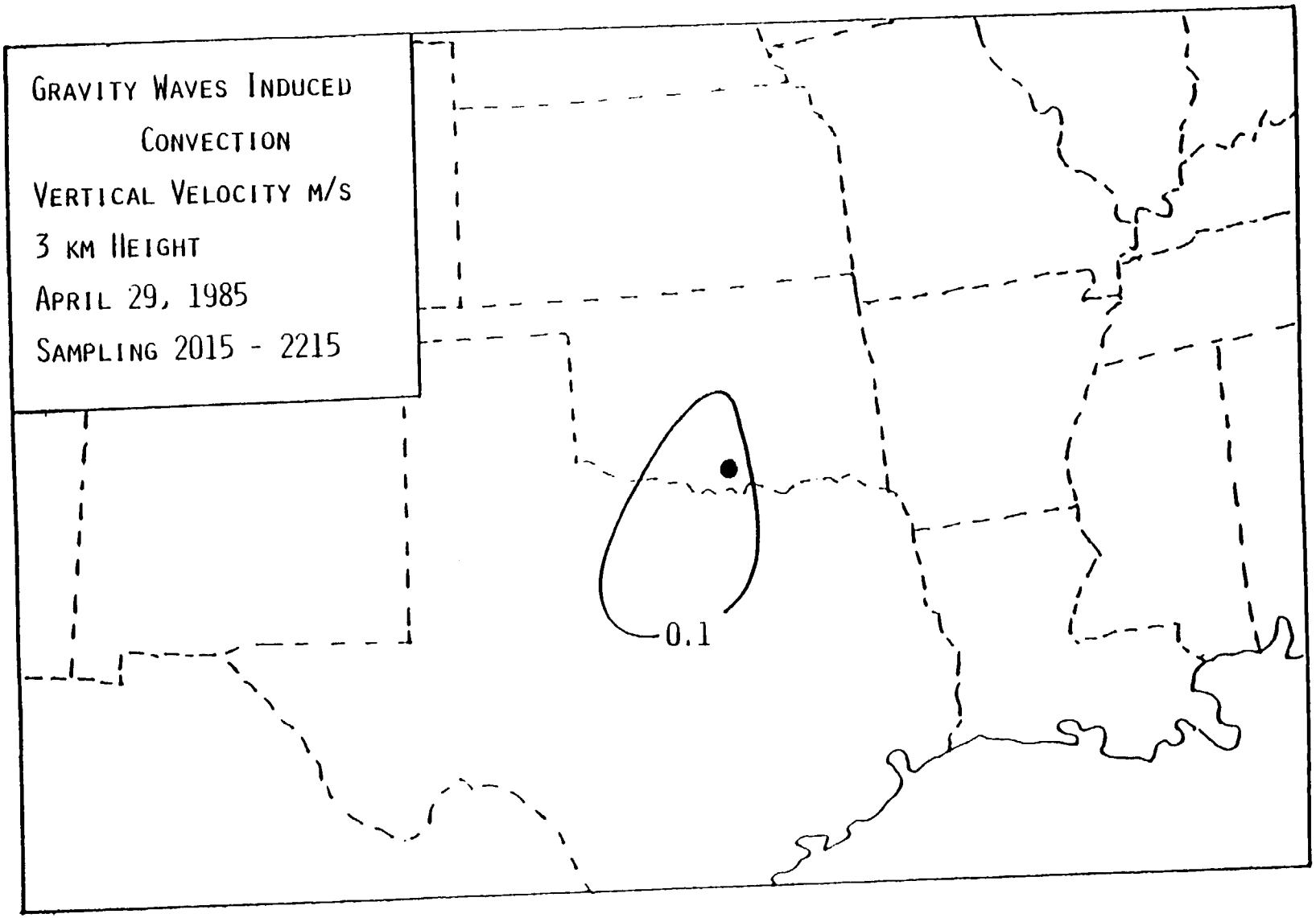
GRAVITY WAVES INDUCED
CONVECTION
VERTICAL VELOCITY M/S
3 KM HEIGHT
APRIL 29, 1985
SAMPLING 2015 - 2215
0.1

FIG. 13

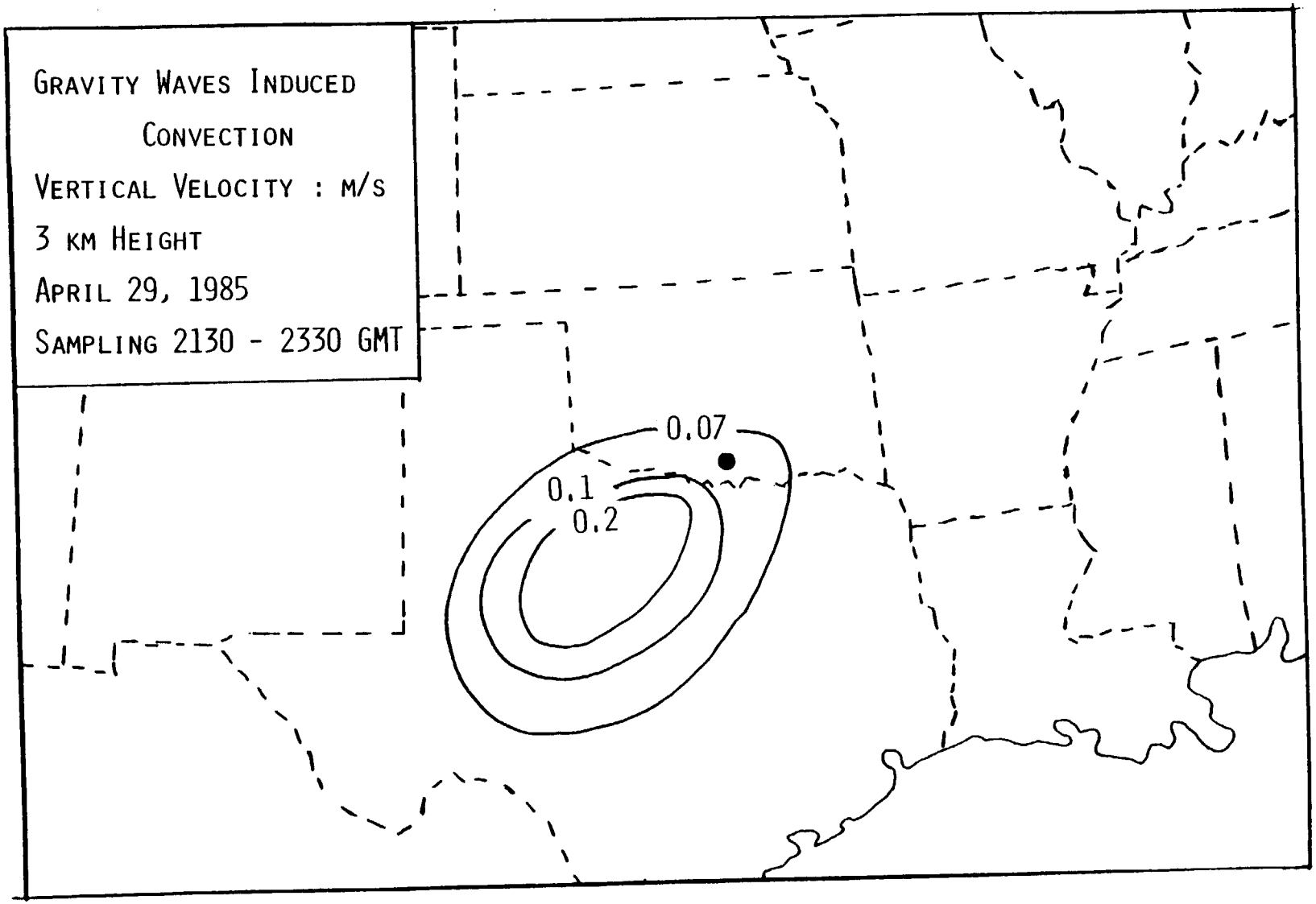
GRAVITY WAVES INDUCED
CONVECTION
VERTICAL VELOCITY : M/S
3 KM HEIGHT
APRIL 29, 1985
SAMPLING 2130 - 2330 GMT
0.07
0.1
0.2

FIG. 14

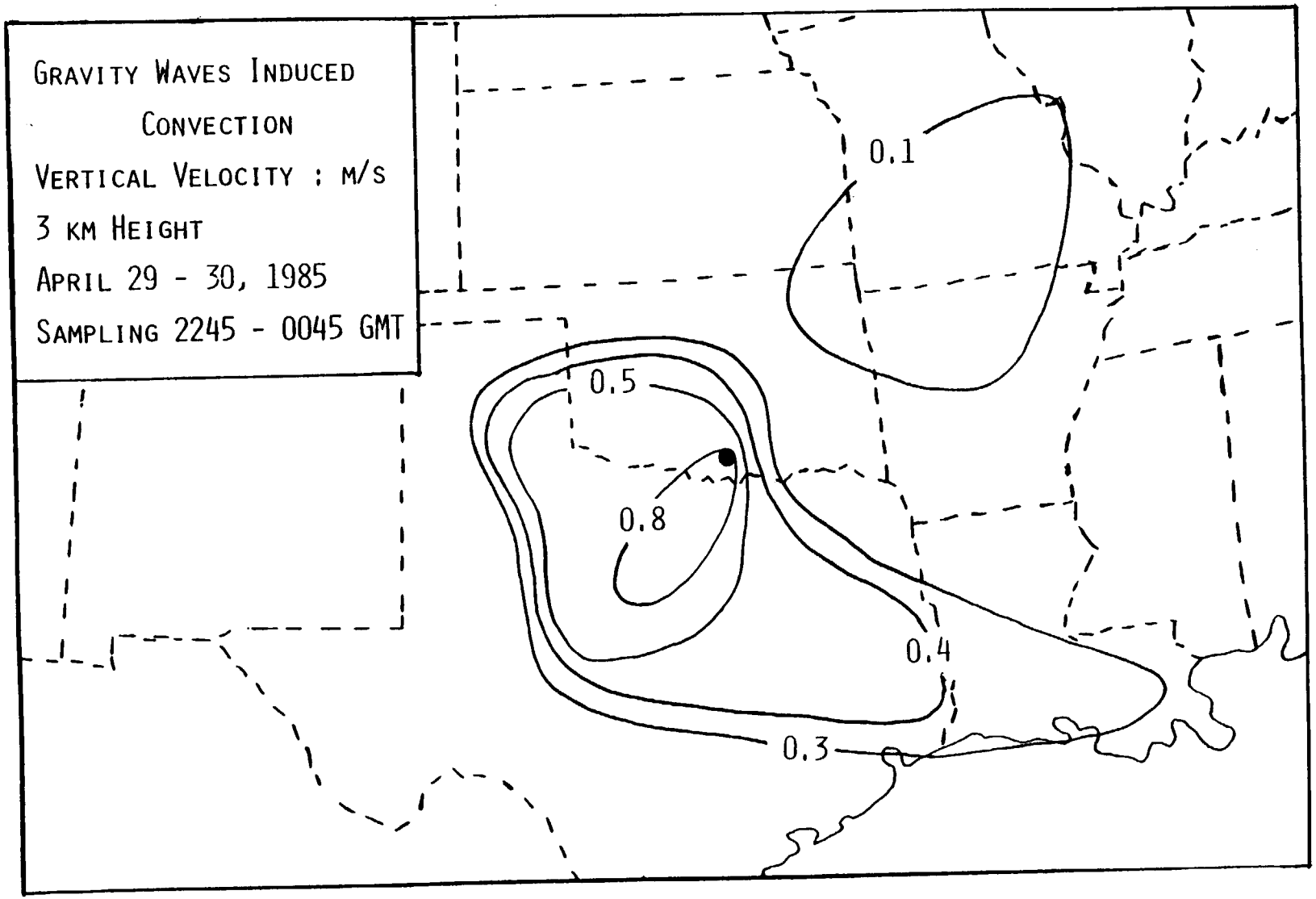
GRAVITY WAVES INDUCED
CONVECTION
VERTICAL VELOCITY : M/S
3 KM HEIGHT
APRIL 29 - 30, 1985
SAMPLING 2245 - 0045 GMT
0.1
0.5
0.8
0.4
0.3

FIG. 15

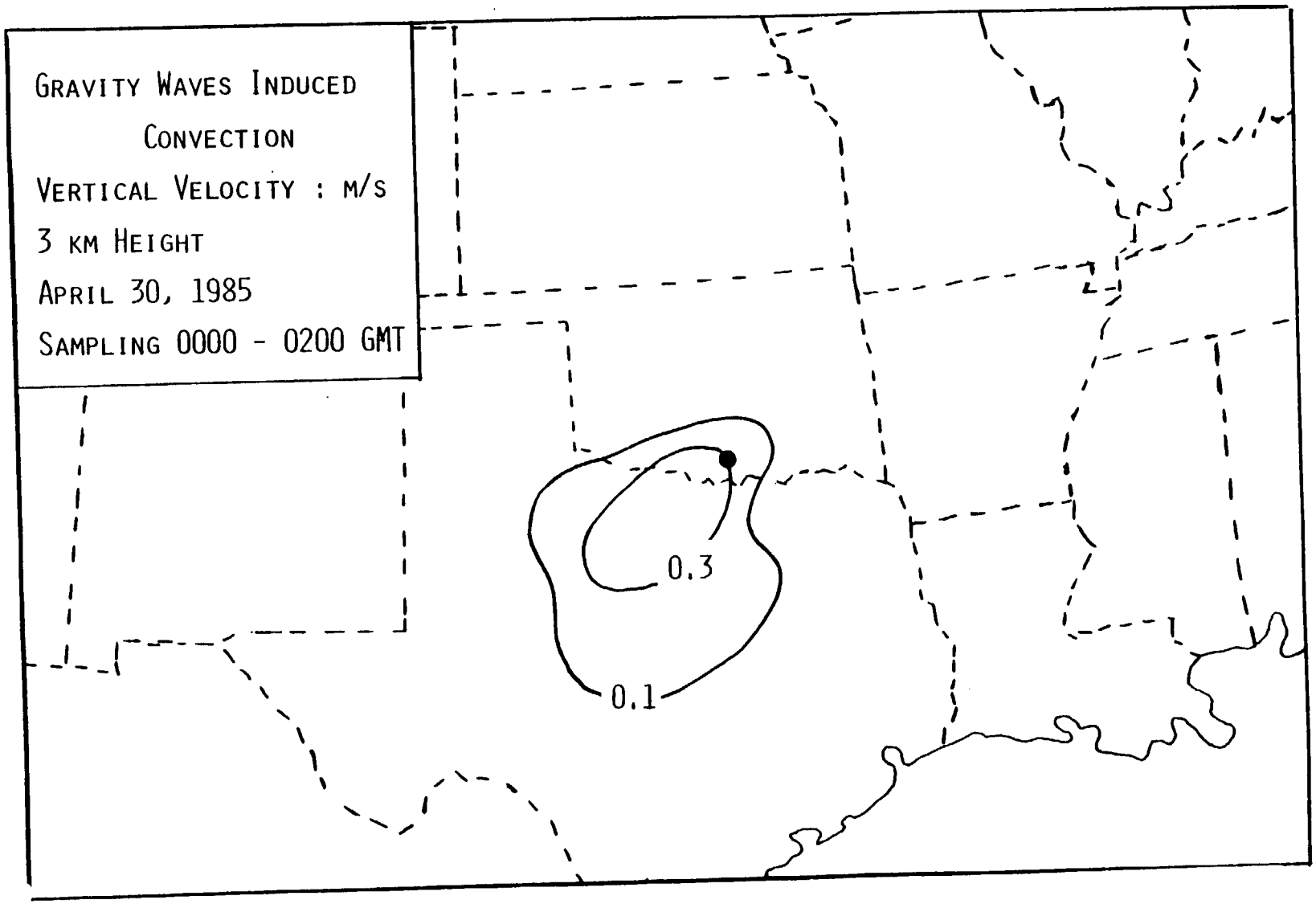
GRAVITY WAVES INDUCED
CONVECTION
VERTICAL VELOCITY : M/S
3 KM HEIGHT
APRIL 30, 1985
SAMPLING 0000 - 0200 GMT
0.3
0.1

FIG. 16

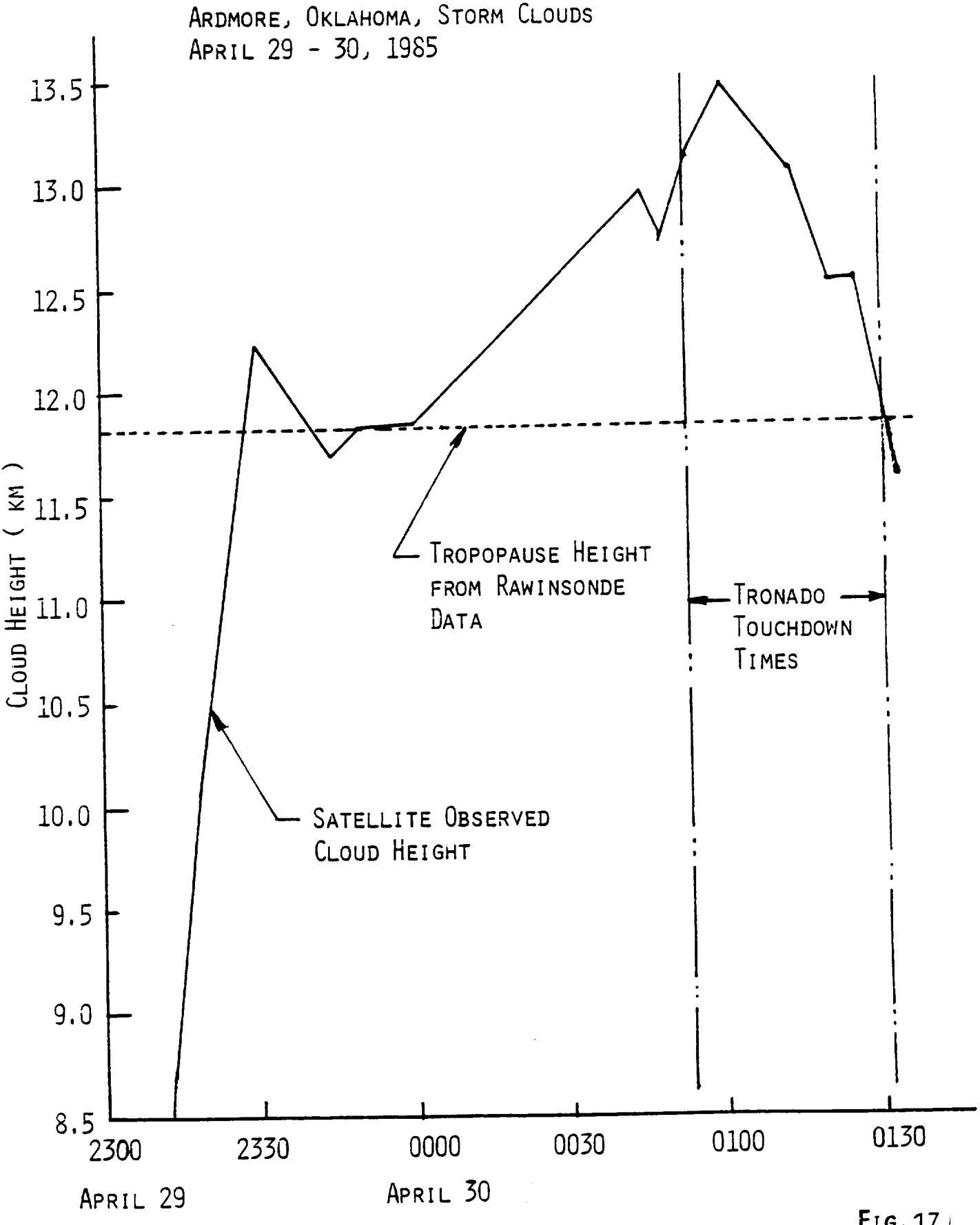
ARDMORE, OKLAHOMA, STORM CLOUDS
APRIL 29 - 30, 1985
13.5
13.0
12.5
12.0
11.5
11.0
10.5
10.0
9.5
9.0
8.5
CLOUD HEIGHT (KM)
TROPOPAUSE HEIGHT FROM RAWINSONDE DATA
TRONADO TOUCHDOWN TIMES
SATELLITE OBSERVED CLOUD HEIGHT
2300
2330
0000
0030
0100
0130
APRIL 29
APRIL 30
TIME (GMT)

FIG. 17

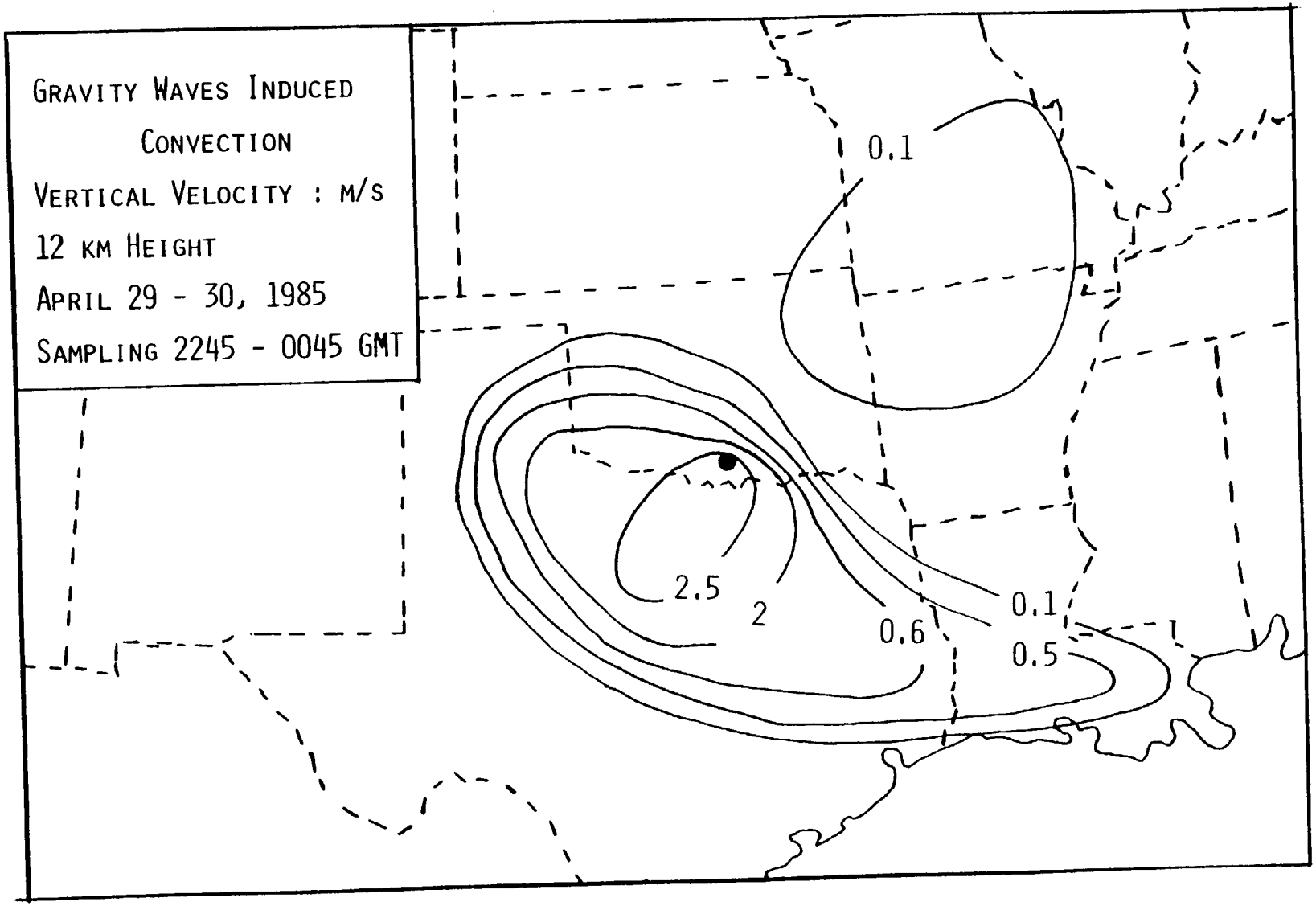
GRAVITY WAVES INDUCED
CONVECTION
VERTICAL VELOCITY : M/S
12 KM HEIGHT
APRIL 29 - 30, 1985
SAMPLING 2245 - 0045 GMT
0.1
2.5
2
0.6
0.1
0.5
1

FIG. 18

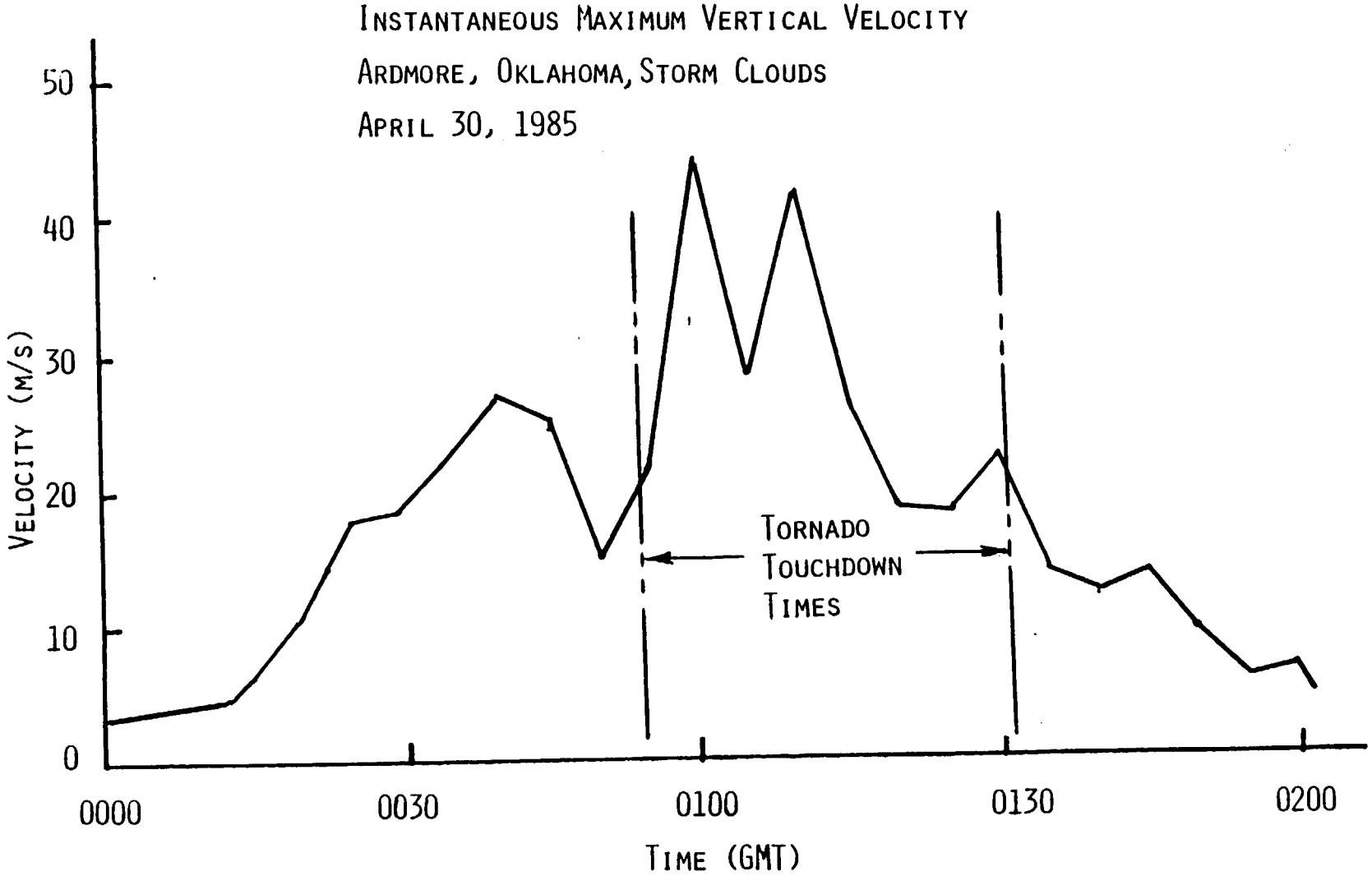
INSTANTANEOUS MAXIMUM VERTICAL VELOCITY
ARDMORE, OKLAHOMA, STORM CLOUDS
APRIL 30, 1985
VELOCITY (M/S)
50
40
30
20
10
0
TORNADO
TOUCHDOWN
TIMES
0000
0030
0100
0130
0200
TIME (GMT)

FIG. 19

Appendix A

Geographical Locations and Characteristics of Gravity Waves Detected

Figures A-1, A-2, A-3, A-4, and A-5 in Appendix A show the wave period, phase speed, propagation direction, and geographical location of gravity waves detected during the time periods of 1900 to 2100, 2015 to 2215, 2130 to 2330, 2245 to 0045, and 0000 to 0200 GMT, respectively. Detailed geographical locations for the area of gravity waves detected are shown in Tables B-1 through B-5 in Appendix B, based on cross correlation analysis from the combination of three microbarogram stations. These geographical location of microbarogram stations are shown in Figure 9. In these figures, a wave period of 20 minutes is marked with a hollow triangle; a wave period of 35 minutes, with a solid triangle; a wave period of 42 minutes, with a hollow circle; and a wave period of 53 minutes, with a smaller solid circle; and tornado touchdown location, with a larger solid circle. The symbols of phase velocities are illustrated at the lower left-hand corner of each figure. As we have mentioned earlier, all of the gravity waves, illustrated in Figuers A-1 through A-5 in Appendix A, are shown at the locations of the wave detection, not at the source points of the waves which will be calculated based on ray tracing computation.

Appendix B

Tables of the Characteristics of Detected Gravity Waves

Table B-1, B-2, B-3, B-4, and B-5 in Appendix B listed the wave period, wavelength, phase velocity, direction of the wave propagation (measured clockwise from the north), and the geographical area of coverage for each gravity wave detected during the time periods of 1900 to 2100, 2015 to 2215, 2130 to 2330, 2245 to 0045, and 0000 to 0200 GMT, respectively. Detection of gravity waves is based on a cross correlation analysis from a combination of three microbarogram stations. The three stations comprising the area of coverage for each gravity wave are identified by an Arbabic number corresponding to the locations shown in Figure 9.

Table B-1: Characteristics of Gravity Waves and Wave - Induced Vertical Convection.
Data Sampling Time : 1900 - 2100 GMT. 29 April 1985

Number	Wave period (min)	Wave length (km)	Phase velocity (m/s)	Direction of propagation (degree)	Induced vertical velocity at 3 km height (m/s)	Induced vertical velocity at 12 km height (m/s)	Area coverage of stations* from cross correlation calculation	Location+ of wave source for gravity waves which induced most significant vertical convection
1	20	145	121	-1.43	0.00932	0.0143	S4, S9, S10	
2	20	330	275	48.65	0.00179	0.0301	S9, S10, S15	
3	35	86	41	-59.22	0.08187	0.0038	S2, S3, S8	C

* See Figure 1 for the geographical distribution of station numbers for microbarograms.
+ See Figures 4 and 14 for map discription.

TableB-2: Characteristics of Gravity Waves and
Wave - Induced Vertical Convection.
Data Sampling Time : 2015 - 2215 GMT. 29 April 1985

Number	Wave period (min)	Wave length (km)	Phase velocity (m/s)	Direction of propagation (degree)	Induced vertical velocity at 3 km height (m/s)	Induced vertical velocity at 12 km height (m/s)	Area coverage of stations* from cross correlation calculation	Location of wave source for gravity waves which induced most significant vertical convection
1	20	281	235	-9.01	0.00265	0.0303	S2, S6, S10	
2	20	154	128	9.08	0.00888	0.0173	S6, S10, S13	
3	20	149	124	74.76	0.01294	0.0223	S10, S11, S13	C
4	20	398	332	-33.95	0.00182	0.0472	S12, S15, S16	
5	20	301	251	-54.19	0.0032	0.0430	S15, S16, S22	
6	20	188	157	-33.09	0.00318	0.0122	S13, S22, S28	
7	35	278	132	-36.62	0.00676	0.0148	S3, S4, S10	
8	35	582	277	45.96	0.00154	0.0263	S3, S6, S10	

TableB-2(Continued)

Number	Wave period (min)	Wave length (km)	Phase velocity (m/s)	Direction of propagation (degree)	Induced vertical velocity at 3 km height (m/s)	Induced vertical velocity at 12 km height (m/s)	Area coverage of stations* from cross correlation calculation	Location+ of wave source for gravity waves which induced most significant vertical convection
9	35	212	101	-82.45	0.01086	0.0070	S6, S10, S13	A
10	35	238	113	53.47	0.00867	0.0101	S6, S13, S17	
11	35	234	112	-60.99	0.00923	0.0100	S13, S17, S23	
12	35	63	30	-53.51	0.12588	0.0642	S13, S21, S23	A
13	35	215	102	85.68	0.00601	0.0042	S10, S21, S23	
14	35	192	91	66.12	0.01372	0.0042	S21, S23, S29	B
15	42	230	91	-46.34	0.00598	0.0018	S10, S13, S21	

* See Figure 1 for the geographical distribution of station numbers for microbarograms.
+ See Figures 4 and 14 for map discription.

TableB-3: Characteristics of Gravity Waves and
Wave - Induced Vertical Convection.
Data Sampling Time : 2130 - 2330 GMT. 29 April 1985

Number	Wave period (min)	Wave length (km)	Phase velocity (m/s)	Direction of propagation (degree)	Induced vertical velocity at 3 km height (m/s)	Induced vertical velocity at 12 km height (m/s)	Area coverage of stations* from cross correlation calculation	Location+ of wave source for gravity waves which induced most significant vertical convection
1	20	296	246	-8.82	0.00211	0.0272	S8, S13, S15	
2	20	356	297	-70.59	0.00116	0.0233	S13, S15, S22	
3	20	64	53	-23.07	0.02212	0.0057	S13, S22, S25	C
4	20	118	98	53.95	0.00668	0.0035	S13, S18, S25	
5	20	270	225	25.32	0.00177	0.0182	S13, S18, S19	
6	20	33	28	-15.35	0.15155	0.1105	S19, S24, S26	A
7	20	52	43	-78.77	0.06214	0.0058	S18, S19, S26	A
8	20	288	240	-28.62	0.00199	0.0242	S18, S25, S26	

TableB-3(Continued)

Number	Wave period (min)	Wave length (km)	Phase velocity (m/s)	Direction of propagation (degree)	Induced vertical velocity at 3 km height (m/s)	Induced vertical velocity at 12 km height (m/s)	Area coverage of stations* from cross correlation calculation	Location of wave source for gravity waves which induced most significant vertical convection
9	35	108	51	18.35	0.02788	0.0067	S2, S6, S10	C
10	35	484	230	-21.38	0.00138	0.0150	S2, S4, S10	
11	35	554	264	-55.73	0.00105	0.0160	S4, S9, S10	
12	35	426	203	51.21	0.00178	0.0140	S9, S10, S15	
13	35	279	133	86.06	0.00414	0.0092	S10, S18, S22	
14	35	203	96	-2.10	0.00786	0.0037	S10, S15, S22	
15	35	243	116	30.82	0.00493	0.0063	S18, S24, S25	
16	35	401	191	62.47	0.00281	0.0189	S20, S22, S29	

Table B-3 (Continued)

Number	Wave period (min)	Wave length (km)	Phase velocity (m/s)	Direction of propagation (degree)	Induced vertical velocity at 3 km height (m/s)	Induced vertical velocity at 12 km height (m/s)	Area coverage of stations* from cross correlation calculation	Location of wave source for gravity waves which induced most significant vertical convection
17	53	302	95	12.08	0.00805	0.0034	S20, S22, S28	
18	42	215	85	73.66	0.01851	0.0022	S18, S23, S25	B

* See Figure 1 for the geographical distribution of station numbers for microbarograms.
+ See Figures 4 and 14 for map discription.

TableB-4: Characteristics of Gravity Waves and Wave - Induced Vertical Convection.
Data Sampling Time : 2245 - 0045 GMT. 29 - 30 April 1985

Number	Wave period (min)	Wave length (km)	Phase velocity (m/s)	Direction of propagation (degree)	Induced vertical velocity at 3 km height (m/s)	Induced vertical velocity at 12 km height (m/s)	Area coverage of stations* from cross correlation calculation	Location+ of wave source for gravity waves which induced most significant vertical convection
1	20	383	319	-63.48	0.00072	0.0169	S3, S4, S15	
2	20	28	24	-23.91	0.11998	0.1403	S4, S5, S15	C
3	20	360	300	82.12	0.00119	0.0245	S12, S15, S20	
4	20	15	13	-51.56	0.51724	2.0145	S14, S21, S26	A
5	20	32	26	-18.81	0.12844	0.1080	S21, S25, S26	A
6	20	27	22	-44.33	0.10419	0.1419	S21, S25, S29	A
7	35	208	99	-22.56	0.00741	0.0041	S4, S9, S11	
8	35	55	26	-86.92	0.12452	0.1058	S13, S17, S18	A

Table B-4(Continue)

Number	Wave period (min)	Wave length (km)	Phase velocity (m/s)	Direction of propagation (degree)	Induced vertical velocity at 3 km height (m/s)	Induced vertical velocity at 12 km height (m/s)	Area coverage of stations* from cross correlation calculation	Location+ of wave source for gravity waves which induced most significant vertical convection
9	35	267	127	-50.25	0.00535	0.0100	S11, S13, S18	
10	35	242	115	-77.87	0.00545	0.0069	S9, S11, S15	
11	35	196	93	-4.78	0.01117	0.0041	S9, S12, S15	C
12	35	529	252	32.49	0.00128	0.0174	S17, S19, S26	
13	35	131	62	69.26	0.02211	0.0058	S17, S18, S26	B
14	35	536	255	78.87	0.00133	0.0186	S15, S18, S26	
15	35	457	218	28.51	0.00182	0.0173	S11, S15, S18	
16	42	64	25	-10.61	0.12898	0.1230	S4, S10, S11	C
17	53	59	18	-7.15	0.26961	0.5411	S21, S23, S27	C
18	53	108	34	35.6	0.04282	0.0112	S9, S20, S21	C

Table B-4(Continue)

Number	Wave period (min)	Wave length (km)	Phase velocity (m/s)	Direction of propagation (degree)	Induced vertical velocity at 3 km height (m/s)	Induced vertical velocity at 12 km height (m/s)	Area coverage of stations* from cross correlation calculation	Location+ of wave source for gravity waves which induced most significant vertical convection
19	53	490	154	45.62	0.00209	0.0076	S5, S9, S12	
20	53	383	120	24,42	0.00344	0.0052	S9, S12, S20	
21	53	715	225	23.54	0.00114	0.0117	S20, S21, S27	

* See Figure 1 for the geographical distribution of station numbers for microbarograms.
+ See Figures 4 and 14 for map discription.

Table B-5: Characteristics of Gravity Waves and Wave - Induced Vertical Convection.
Data Sampling Time : 0000 - 0200 GMT. 30 April 1985

Number	Wave period (min)	Wave length (km)	Phase velocity (m/s)	Direction of propagation (degree)	Induced vertical velocity at 3 km height (m/s)	Induced vertical velocity at 12 km height (m/s)	Area coverage of stations* from cross correlation calculation	Location+ of wave source for gravity waves which induced most significant vertical convection
1	20	21	18	-1.42	0.32450	0.7081	S18, S19, S23	A
2	20	236	197	-54.33	0.00165	0.01206	S19, S23, S26	
3	20	107	89	88.77	0.01298	0.00288	S18, S23, S25	B
4	20	283	236	26.08	0.00230	0.02663	S4, S8, S16	
5	20	215	179	13.17	0.00400	0.0225	S13, S18, S19	
6	20	22	19	-46.16	0.18643	0.37492	S23, S25, S26	A
7	20	170	142	-50.55	0.00638	0.01766	S13, S18, S25	
8	53	421	133	73.02	0.00825	0.01814	S4, S8, S16	

TableB-5(Continued)

Number	Wave period (min)	Wave length (km)	Phase velocity (m/s)	Direction of propagation (degree)	Induced vertical velocity at 3 km height (m/s)	Induced vertical velocity at 12 km height (m/s)	Area coverage of stations* from cross correlation calculation	Location+ of wave source for gravity waves which induced most significant vertical convection
9	35	159	76	82.12	0.01280	0.00128	S21, S23, S25	B
10	35	316	150	-80.43	0.00323	0.01088	S6, S10, S14	
11	35	361	172	-72.12	0.00248	0.01242	S10, S11, S21	
12	35	316	150	-58.11	0.00324	0.01086	S11, S21, S22	
13	35	350	167	0.13	0.00527	0.02418	S11, S15, S22	
14	35	423	201	-33.91	0.00181	0.01397	S14, S21, S23	
15	35	161	77	-19.58	0.01246	0.00100	S21, S22, S25	C
16	42	314	125	43.55	0.00353	0.00617	S4, S7, S10	

Table B-5(Continued)

Number	Wave period (min)	Wave length (km)	Phase velocity (m/s)	Direction of propagation (degree)	Induced vertical velocity at 3 km height (m/s)	Induced vertical velocity at 12 km height (m/s)	Area coverage of stations* from cross correlation calculation	Location+ of wave source for gravity waves which induced most significant vertical convection
17	42	318	126	71.08	0.00498	0.00911	S4, S10, S11	
18	42	315	125	39.71	0.00625	0.0110	S4, S11, S15	
19	42	438	174	-39.62	0.00323	0.01673	S4, S12, S15	

* See Figure 1 for the geographical distribution of station numbers for microbarograms.
+ See Figure 4 and 14 for map discription.

Appendix A - Figure Captions

Figure A-1. Geographic distribution of gravity waves detected from microbarograph data during the data sampling time: 1900-2100 GMT, 19 April 1985. Numbers of corresponding gravity waves are listed in Table B-1 of Appendix B. Symbolized times are wave periods of gravity waves which are explained in the left upper corner of the figure; while the symbols of arrow are phase velocities of gravity waves which are illustrated in the left lower corner of the figure.

Figure A-2. Geographic distribution of gravity waves detected from microbarograph data during the data sampling time: 2015-2215 GMT, 29 April 1985. Numbers of corresponding gravity waves are listed in Table B-2 of Appendix B. Symbolized times are wave periods of gravity waves which are explained in the left upper corner of the figure; while the symbols of arrow are phase velocities of gravity waves which are illustrated in the left lower corner of the figure.

Figure A-3. Geographic distribution of gravity waves detected from microbarograph data during the data sampling time: 2130-2330 GMT, 29 April 1985. Numbers of corresponding gravity waves are listed in Table B-3 of Appendix B. Symbolized times are wave periods of gravity waves which are explained in the left upper corner of the figure; while the symbols of arrow are phase velocities of

gravity waves which are illustrated in the left lower corner of the figure.

Figure A-4. Geographic distribution of gravity waves detected from microbarograph data during the data sampling time: 2245 GMT, 29 April 1985 to 0045 GMT, 30 April 1985. Numbers of corresponding gravity waves are listed in Table B-4 of Appendix B. Symbolized times are wave periods of gravity waves which are explained in the left upper corner of the figure; while the symbols of arrow are phase velocities of gravity waves which are illustrated in the left lower corner of the figure.

Figure A-5. Geographic distribution of gravity waves detected from microbarograph data during the data sampling time: 0000-0200 GMT, 30 April 1985. Numbers of corresponding gravity waves are listed in Table B-5 of Appendix B. Symbolized times are wave periods of gravity waves which are explained in the left upper corner of the figure; while the symbols of arrow are phase velocities of gravity waves which are illustrated in the left lower corner of the figure.

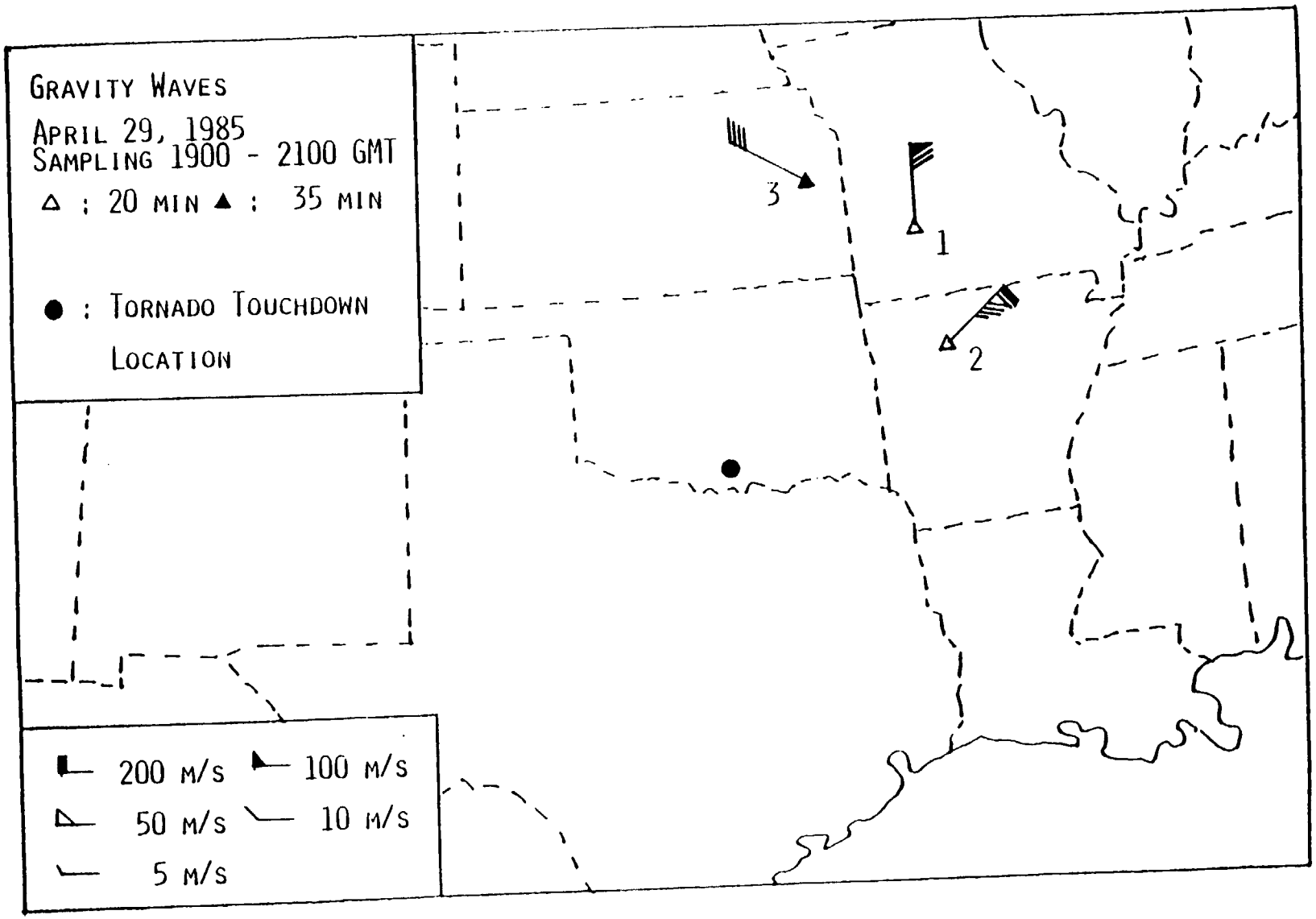
GRAVITY WAVES
APRIL 29, 1985
SAMPLING 1900 - 2100 GMT
△ : 20 MIN ▲ : 35 MIN
● : TORNADO TOUCHDOWN LOCATION
200 M/S
100 M/S
50 M/S
10 M/S
5 M/S
1
2
3

FIG. A-1

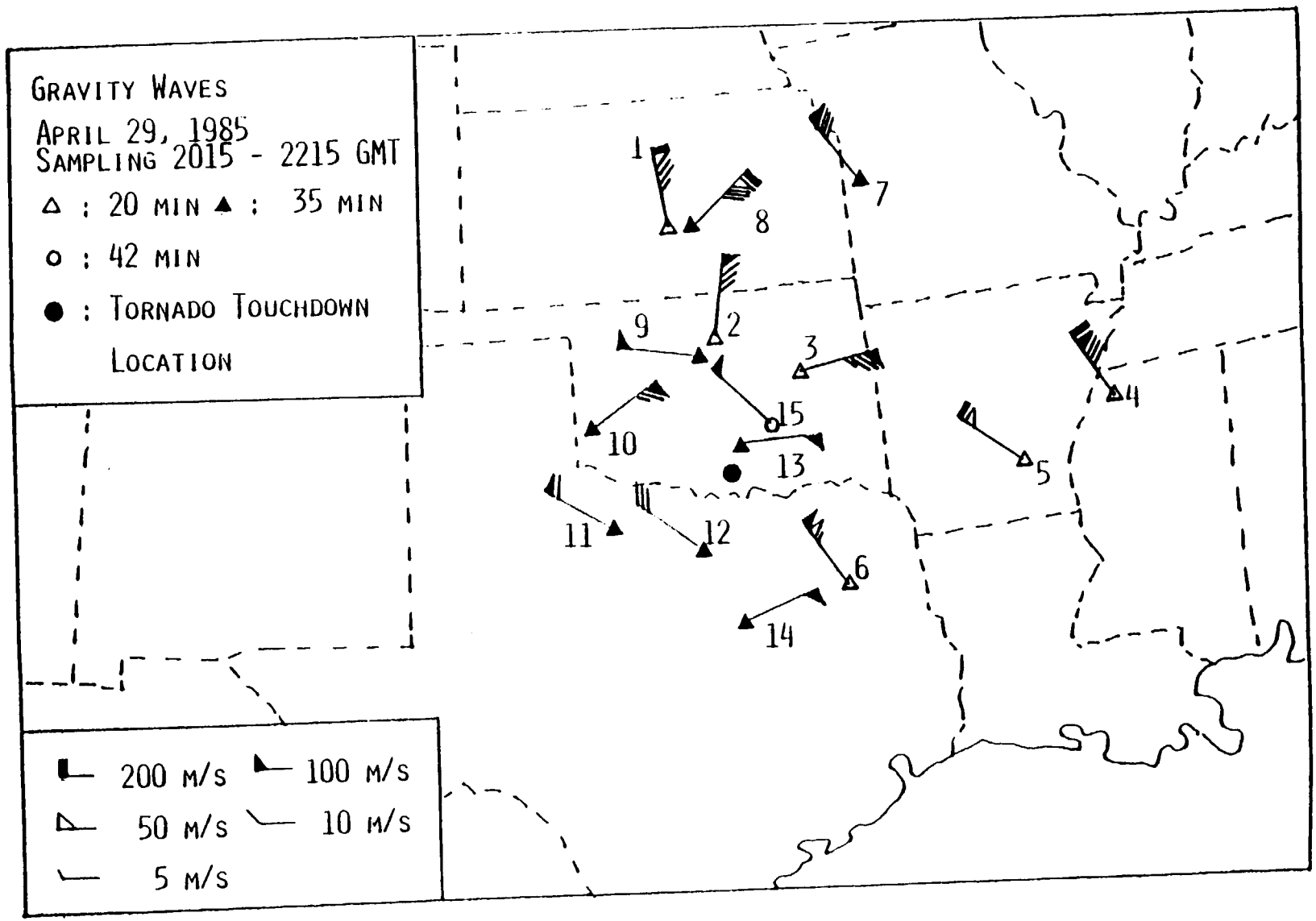
GRAVITY WAVES
APRIL 29, 1985
SAMPLING 2015 - 2215 GMT
△ : 20 MIN ▲ : 35 MIN
○ : 42 MIN
● : TORNADO TOUCHDOWN LOCATION
200 M/S
100 M/S
50 M/S
10 M/S
5 M/S
1
2
3
4
5
6
7
8
9
10
11
12
13
14
15

FIG. A-2

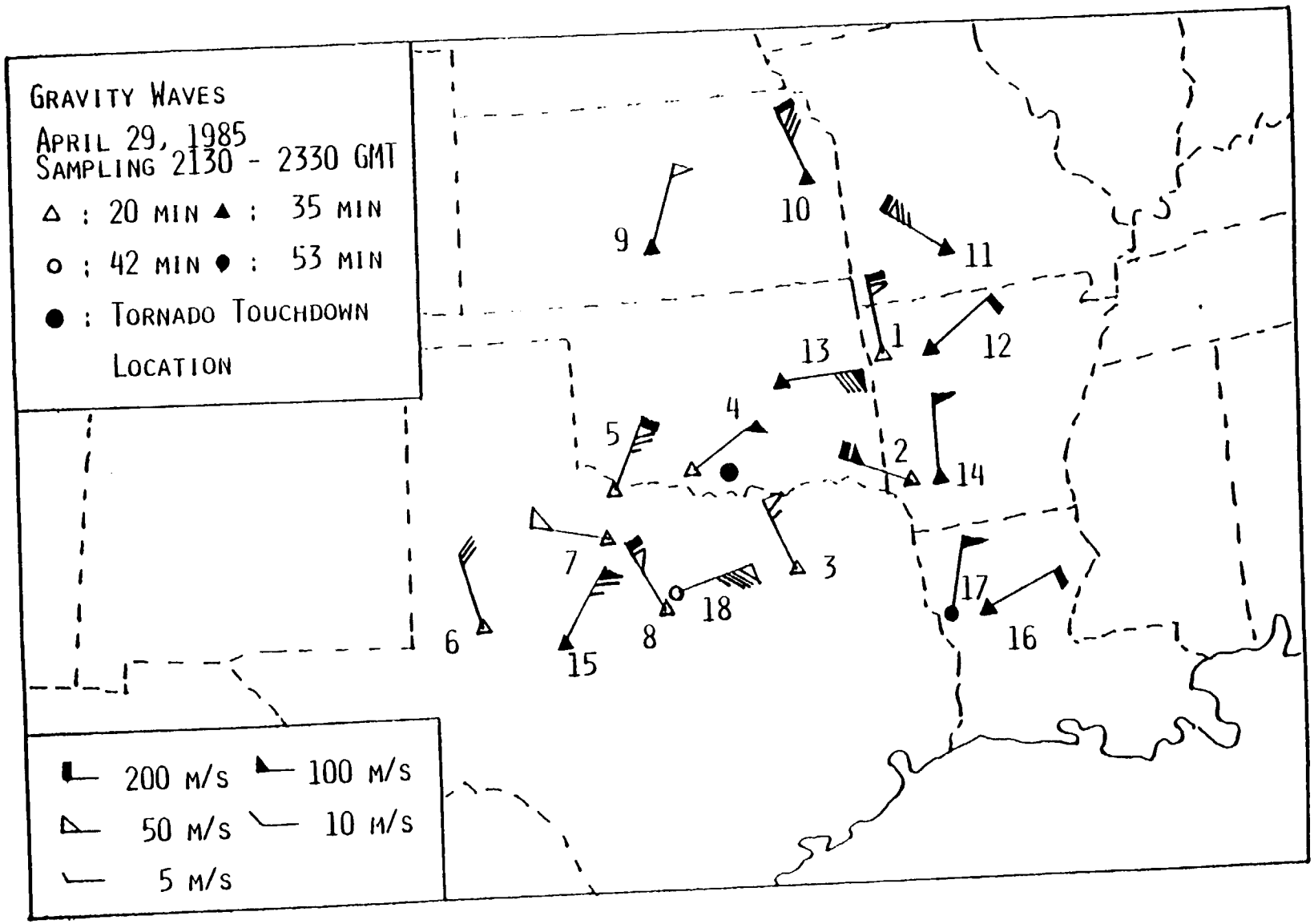
GRAVITY WAVES
APRIL 29, 1985
SAMPLING 2130 - 2330 GMT
△ : 20 MIN ▲ : 35 MIN
○ : 42 MIN ● : 53 MIN
● : TORNADO TOUCHDOWN LOCATION
200 M/S
100 M/S
50 M/S
10 M/S
5 M/S
1
2
3
4
5
6
7
8
9
10
11
12
13
14
15
16
17
18

FIG. A-3

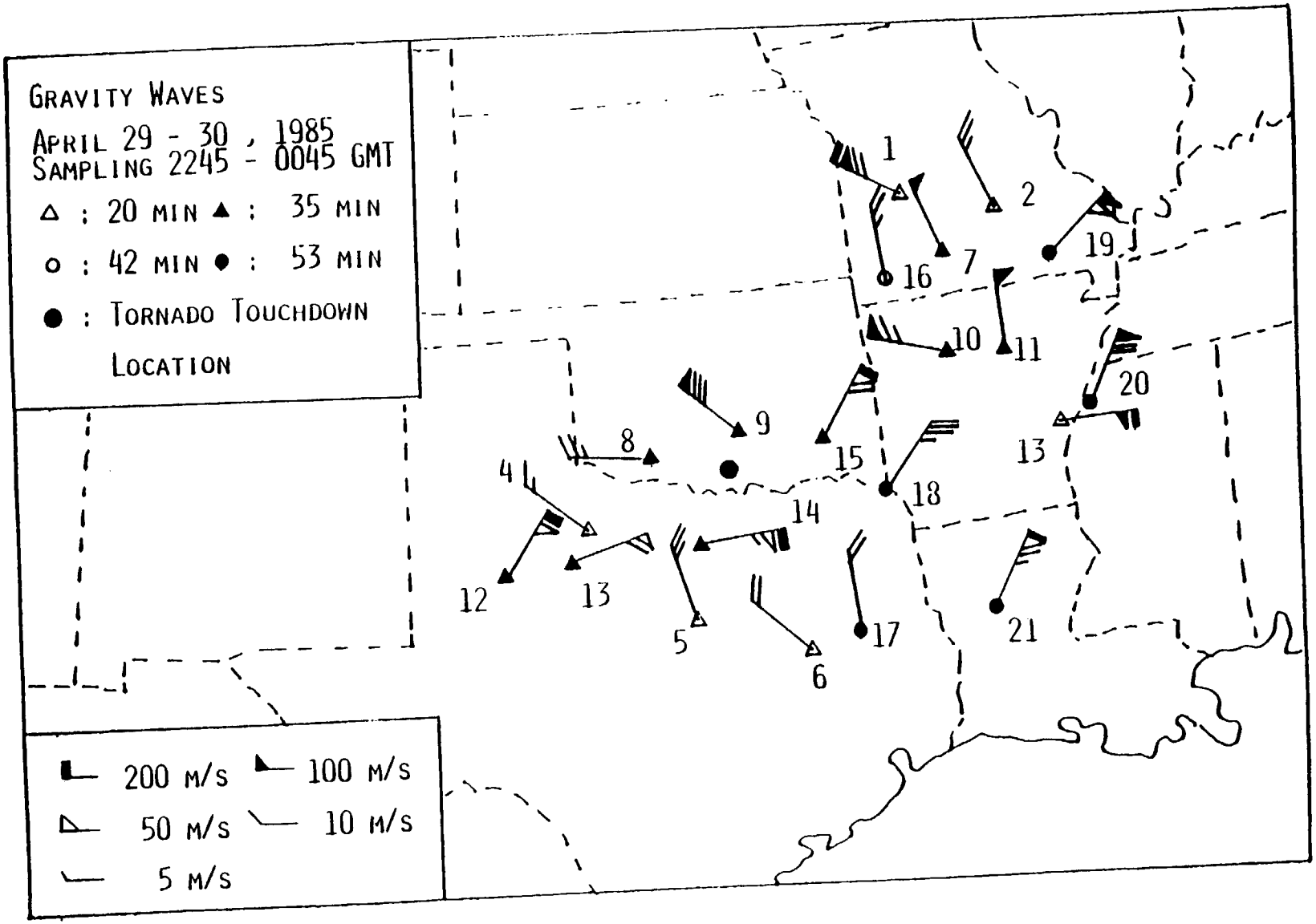
GRAVITY WAVES
APRIL 29 - 30 , 1985
SAMPLING 2245 - 0045 GMT
△ : 20 MIN ▲ : 35 MIN
○ : 42 MIN ● : 53 MIN
● : TORNADO TOUCHDOWN LOCATION
200 M/S
100 M/S
50 M/S
10 M/S
5 M/S
1
2
3
19
16
7
10
11
20
9
8
15
13
4
18
14
12
13
5
6
17
21

FIG. A-4

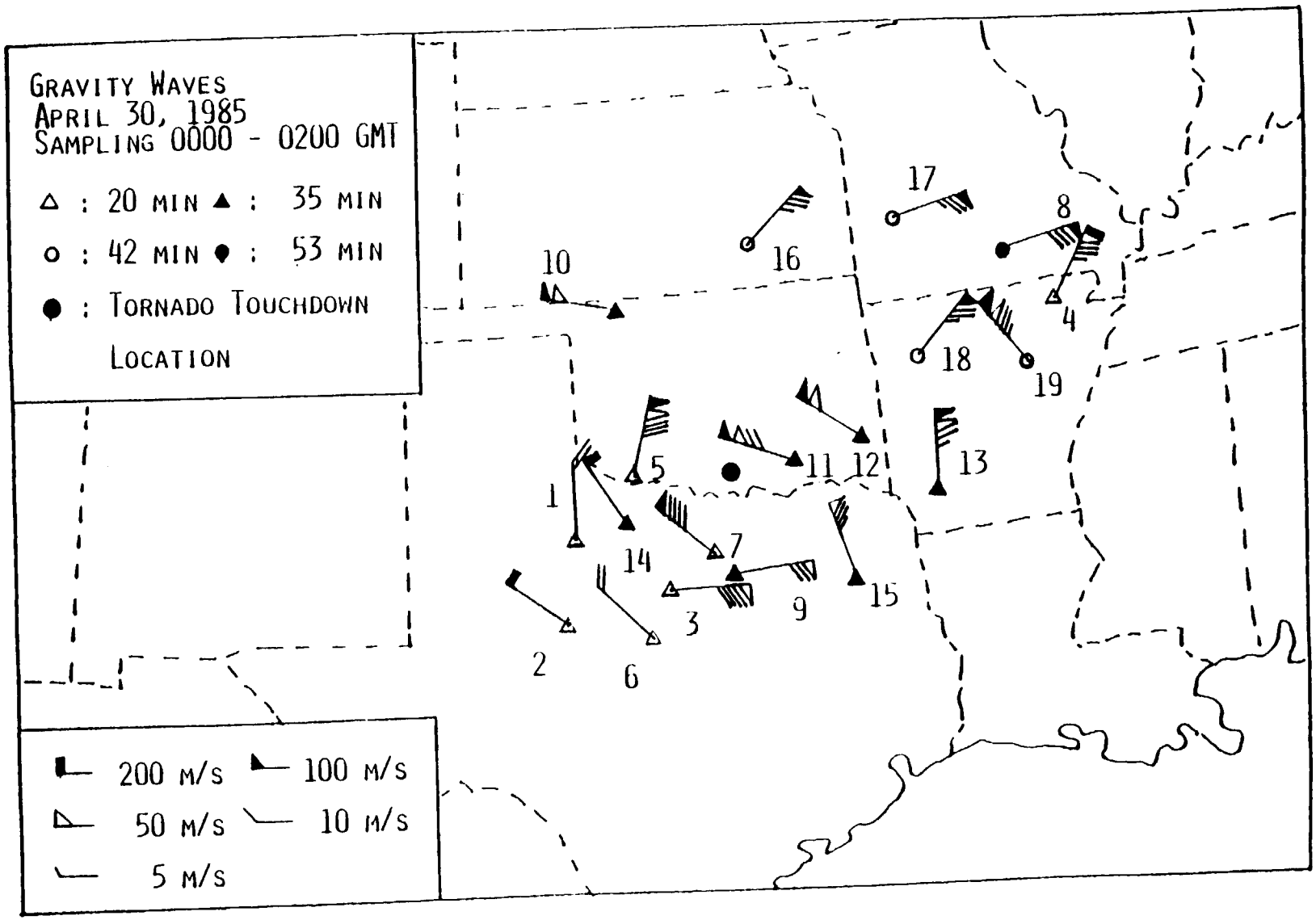
GRAVITY WAVES
APRIL 30, 1985
SAMPLING 0000 - 0200 GMT
△ : 20 MIN ▲ : 35 MIN
○ : 42 MIN ● : 53 MIN
● : TORNADO TOUCHDOWN LOCATION
200 M/S
100 M/S
50 M/S
10 M/S
5 M/S
1
2
3
4
5
6
7
8
9
10
11
12
13
14
15
16
17
18
19

FIG. A-5

SECTION II

SATELLITE INFRARED REMOTE SENSING AND NUMERICAL SIMULATION OF STORM CLOUDS

Abstract

Both rawinsonde data and geosynchronous satellite imagery were used to study the life cycles of Ardmore, Oklahoma's severe convective storms. Cloud Modeling with input sounding data from Oklahoma City, Oklahoma, and rapid-scan imagery from GOES were used to investigate storm cloud formation, development and dissipation in terms of growth and collapse of cloud tops, as well as, the life cycle of the penetration of overshooting turrets above the tropopause. The results based on these two approaches showed: (1) storm clouds developed to a mature stage with overshooting cloud tops that penetrated above the tropopause; (2) they collapsed at approximately 9 minutes before the touchdown of tornadoes; and (3) at the time of storm dissipation, cloud tops collapsed at a high rate, approximately 6 minutes before the liftoff time of the tornadoes. Cloud modeling also showed that the local tropopause height decreased during the time when overshooting cloud tops penetrated above the tropopause due to the local subsidence around the overshooting top.

1. Introduction

It has long been recognized that severe storm development is favored by strong convective instability, abundant moisture at low levels, strong wind shear, and a dynamical lifting mechanism that can release the instability (Newton, 1963). Most thunderstorms are composed of short-lived units of convection referred to as cells. The cumulus stage in cell development is characterized by updrafts and downdrafts. As the cell builds up, a large amount of water vapour condenses and cloud droplets grow to precipitation particles (Barnes, 1976). Schlesinger (1973a; 1973b) showed that the greater moisture supply can intensify the convection which, in turn, will support an intense storm. Kuo (1965, 1974) indicates that the greater temperature difference between the cloud and the environment, and the larger convergence of moisture produced by the large scale flow, will be favorable in the development of cumulus convection. In the presence of favorable vertical distributions of temperature, humidity, and wind velocity encountered in some frontal regions, a much more vigorous unit of convection may develop (Browning, 1964). These convective systems are important, because they are responsible for a disproportionate amount of severe weather, especially damaging tornadoes and hail (Nelson, 1976).

Convective instability can be induced by proper vertical profiles of temperature and moisture (Schlesinger,

1973a; 1973b). It can also be initiated by gravity waves (Curry and Murty, 1974; Gossard and Sweezy, 1974; Stull, 1976; Uccellini, 1975; Hung and Kuo, 1978; Hung and Smith, 1978; Hung et al., 1978; 1979a; 1979b).

In this study, rawinsonde data was used to investigate the background meteorological conditions. Based on the analysis of rawinsonde data available all over the United States, the Barnes (1964) scheme was used to maximize the geographical detail, and to determine that the area favored the initiation of storm development. Rawinsonde observation was also used as initial input data for the cloud modeling for the life cycle of storm formation, development and dissipation of the Ardmore, Oklahoma storm clouds. Rawinsonde data from Oklahoma City, Oklahoma at 0000 GMT, 30 April 1985 was used in the analysis. Rapid-scan infrared imagery from GOES was also used to study the life cycle of the Ardmore storm clouds and was compared with the results obtained from cloud modeling.

In the investigation of mesoscale storm development, it is not practical to use conventional sounding data taken at 12 hour intervals to study cloud formation and development. Special sounding data, such as the Atmospheric Variability Experiments (AVE) conducted by the NASA Marshall Space Flight Center, and the Severe Environmental Storms and Mesoscale Experiments (SESAME) managed by the NOAA National Severe Storms Laboratory, were designed for the observation of

mesoscale storm development. Sometimes, even the use of these special sounding data taken at 3 hour intervals is not frequent enough to study clouds that have a life cycle of a couple of hours. To improve this situation, numerical cloud modeling is carried out to study cloud formation, development and dissipation.

The model used in this study has been designed such that mesoscale convergence can be superimposed in the lower levels and divergence in the upper levels, which can result in stratus-type clouds being formed under certain atmospheric conditions (Orville, 1965; Orville and Kopp, 1977; Chen and Orville, 1980; Orville et al., 1984; Hung and Tsao, 1987; Hung and Tsao, 1988). The lower level wind profile is computed from all the available rawinsonde data in the area, and mesoscale convergence is superimposed in the lower 6 km height. The upper level wind profile is also calculated from all the available rawinsonde data with the upper level divergence adjusted by the rapid-scan visible and infrared imagery of cloud development obtained from GOES. The continuity equation is used to guarantee the flows satisfying the condition of mass conservation. In this model, deep convection, in which the basic equations are given in Chen and Orville (1980), is considered. This cloud model is available at NASA Marshall Space Flight Center and NASA Goddard Space Flight Center (Hung and Tsao, 1987; and 1988).

Geosynchronous satellite data is a potentially powerful

tool for studying enhanced convection and mesoscale systems. Purdom (1976), Sikdar et al. (1970), and Hung et al. (1980) used satellite infrared and visible imagery to study mesoscale convection. The life cycle of a severe storm can also be observed from rapid-scan infrared imagery from a satellite (Hung et al., 1983). In this study, three-minute interval rapid-scan imagery from GOES was used in the analysis to study the life cycle of the Ardmore storm clouds and was compared with the results obtained from cloud modeling.

2. Meteorological Background

In this study, a severe storm at Ardmore, Oklahoma, at 0054 GMT (1854 LT), 30 April 1985 was chosen as a case to study the initiation, formation and development of storm clouds based on numerical simulation and comparison with rapid-scan satellite infrared remote sensing of storm clouds. On the evening of 29 April (LT), a tornado touched down at 1854 LT, about 20 km southwest of Ardmore, Oklahoma, moved north about 4.8 km, and then turned northeast and traveled another 17.6 km through the southeast outskirts of Ardmore before dissipating. The liftoff time of the tornado was 0131 GMT (1931 LT). Storm damage was rated as F2 on the Fujita Scale (National Climate Data Center, 1985).

Detailed description of surface meteorological data, geographical distribution of surface humidity mixing ratio,

vertical temperature and dew point temperature profile, the 850 mb weather map, geographical distribution of surface divergence, etc., on this perticular day, have been fully discussed in the first paper of present study (Hung and Tsao, 1989).

Figure 1 shows the radar summary at 2235 GMT, 29 April 1985. A convective cloud belt extending from Colorado to Louisiana is shown in the figure. This convective cloud belt was scattered in the area between the three axes of the low pressure trough where the atmosphere was extremely moist and unstable.

Radar returns show that clouds did not form at south central Oklahoma, near the Texas borderline before 2235 GMT (radar summaries are available at one-hour intervals). Satellite infrared imagery from GOES also shows that clouds did not form before 2300 GMT in south central Oklahoma. Figure 2 shows a time history of cloud formation and development for clouds responsible for the outbreak of tornadic storms. The cloud formed at 2314 GMT, and grew rapidly to the mature stage within one hour. This cloud merged with the rest of the cloud belt after 0200 GMT.

Convective instability can be induced by proper vertical profiles of temperature and moisture. It can also be released by the presence of gravity waves (Curry and Murty, 1974; Uccellini, 1975; Hung et. al., 1978; Hung and Smith, 1981). Gravity waves associated with tornado activity (Hung

et. al., 1978; 1980; Hung and Smith, 1978; 1983) and hurricane/typhoon (Hung and Kuo, 1978; Hung et al., 1988a) have been observed with a high frequency continuous wave Doppler array system and VHF radars. By using a ray tracing technique, Hung et. al. (1979a; 1979b) have shown that the enhanced convection-initiated gravity waves associated with severe storms were generated by thunderheads embedded in a squall line and/or an isoloated cloud with intense convection. During the time period between 1900 GMT, 29 April 1985 and 0200 GMT, 30 April 1985, microbarograph data from all the available microbarogram stations in the south central United States were used in the analysis of gravity waves detected in the area. The data showed to what degree large amplitude gravity waves had been linked to the onset of convective storm systems. Figure 3 shows a three-station sample microbarograph data from Dallas/Ft. Worth, Texas; Amarillo, Texas; and San Angelo, Texas, during the time period between 2040 to 2155 GMT, 29 April 1985. Unit of pressure fluctuation is also shown with an arrow in the figure. Analysis shows that large amplitude gravity waves, having wave periods of 20 minutes generated by the mesoscale convective systems, initiated convection in the area of the tornado occurrence. Calculation also shows that the maximum vertical motion induced by the gravity waves was 0.8 m/s at 3 km height and 2.5 m/s at 12 km height for the case of the Ardmore storms. Detailed description of gravity wave-

induced convection for Ardmore storm clouds will be presented in Hung and Tsao (1989).

3. Mathematical Model

The fundamental equations governing the processes of the evolution of wind components, water vapor content and potential temperature under the influences of vertical turbulent momentum transfer, and turbulent energy transfer are referred to by Orville and Kopp(1977), Orville et al. (1984), and Hung and Tsao (1988).

In this study, a two-dimensional model is considered. Within a time period of two hours for the study of mesoscale phenomena, average horizontal wind field has been determined mainly based on satellite rapid-scan imagery to obtain the average direction of the horizontal wind. By using average direction of horizonal wind as the direction of x-coordinate, and vertical direction as the z-coordinate, we can formulate a two-dimensional model. With the inclusion of ice phase (Orville and Kopp, 1977) and the realistic turbulence of eddy coefficient for momentum, eddy diffusion coefficient for water vapor, eddy coefficient for heat flux, etc., (Chen and Orville, 1980; Orville et. al., 1984) into the model, we can simulate the development of mesoscale severe storms (Hung and Tsao, 1987; and 1988).

For the computation of deep convection, the main idea of the technique is to decompose the velocity into cloud-scale

velocity and mesoscale velocity (Pielke, 1974). The mesoscale velocity is kept constant with respect to time. Running the model with no initial impulse indicates how rapidly this steady state mesoscale convergence field destabilizes the atmosphere (Chen and Orville, 1980). This stabilization is the essential mechanism for an explosive burst of cloud convection.

This model has been designed to study mesoscale cloud formation and development in which mesoscale convergence is input to the convective scale domain and convergence is superimposed in the lower levels and divergence in the upper levels (Orville, 1965; Orivlle and Kopp, 1977; Orville et al., 1984). In this model, deep convection, in which the basic equations were given in Chen and Orville (1980), is considered.

The computer program is available and installed on the Cyber 205 at NASA Goddard Space Flight Center, Greenbelt, Maryland, and CRAY X-MP at NASA Marshall Space Flight Center, Huntsville, Alabama (Hung and Tsao, 1987; 1988).

4. Numerical Simulation of Storm Clouds

The concepts of fundamental equations governing the processes of the evolution of wind components, water vapor content, and potential temperature under the influences of vertical turbulent momentum transfer and turbulent energy transfer are described in our earlier papers (Hung and Tsao,

1987; 1988).

Simulation of the life cycle of a cloud can be carried out with the location of the low level concentration of moisture, determined from the larger area computation, based on the available rawinsonde observations all over the United States by using the Barnes (1964) scheme, as a center, and the spatial coordinate of 20 km x 20 km size, with 100 x 100 grid points.

Figures 4 and 5 show a geographical distribution of surface divergence (with a unit of 10^{-5} sec^{-1}), and a geographical distribution of surface moisture content (mixing ratio with a unit of g/kg), respectively, both at 0000 GMT, 30 April 1985, based on the available surface data. It is shown that, in the neighborhood of tornado occurence, the surface divergence was -2×10^{-5} sec^{-1} (negative value implies convergence), and a high concentration of moisture with mixing ratio of 13 g/kg. The temperature at the location of the tornado occurrence was 15^{0}c at 850 mb height.

Procedures of the numerical computation are as follows: (1) read sounding data, (2) iterate sounding data and fill in all grid points, (3) set up perturbation, (4) compute stream function and vorticity, (5) store all the data in the history file, (6) calculate the time $t = t + \Delta t$, (7) calculate the wind from the stream function, (8) calculate the advection, turbulence, diffusion, moisture balance, etc., (9) calculate the new stream function and vorticity, and (10) calculate the

cloud formation and dissipation. The iteration process indicated in Item (2) implies the following procedures: (a) fill in all grid points from sounding data with the same heights, (b) make adjustments of data stored in all grid points through the open boundaries obtained from the flow parameters based on the larger area computation from all the available rawinsonde data in the area, and the computation of the continuity equation, and (c) iterate the data of fluid flow satisfying the steady state condition of mass conservation.

The domain of the model is an area of 20 km in the horizontal, by 20 km in the vertical, with a 200 m grid spacing in each direction. Perturbations in the intitial temperature field induce vertical motions which lead to cloud formation. In this study, a 0.5 K increase in temperature was added to the center grid points in the lowest layers of the model, decreasing to either side and in the vertical. Thus, a warm bubble is introduced in the center of the grid at the surface. This bubble, which extends over an area of 2 to 3 km on each side, serves as the driving force of convection.

In this study, the lateral boundary conditions are open so that an air flow is permitted through them. Horizontal gradients are assumed to be zero for all variables except the stream function; therefore, inflows are not advecting a gradient into the grid. The boundary conditions on the stream function determine the convergence. For a no-

convergence case, the horizontal gradient in the stream function at the boundary is zero; otherwise, it is non-zero (Chang and Orville, 1973).

Input parameters in the computation of the cloud model include an initial time step which is determined from: (1) the length of the grid spacing divided by the maximum wind speed; (2) concentration of condensation nuclei; and (3) pressure, temperature, dew point, and wind speed obtained from the rawinsonde data. In the present study, an initial time step of 0.25 mimutes, based on grid spacing and maximum wind speed from rawinsonde data, was adopted. The model was designed to calculate the time step automatically based on numerical stability conditions.

Available temperature, moisture and wind profiles from rawinsonde observations all over the United States were analyzed using the Barnes (1964) scheme, through the Man Computer Interactive Data Access System (McIDAS), to maximize the geographical detail. On the McIDAS system, available at NASA Marshall Space Flight Center, Huntsville, Alabama, the "smoothness" of the gridded fields depends on two factors, the weight function parameter and the convergence factor. The convergence factor is fixed at 0.3 which allows the user to pick a response curve by varying the weight function parameter to fit the geographical station distribution of rawinsonde data. To avoid rawinsonde data

taken during the period of time inside the clouds, or some data modified by the convection, manual modification of temperature and moisture profiles of geographical distribution have been made for abrupt jumps of data which were cross-checked with rapid-scan imagery obtained from GOES. Among the many locations where low level, high moisture content appeared on this stormy day, the location at south central Oklahoma was chosen as a center, and, in this case, the spatial x-coordinate axis was chosen along the direction of wind motion based on the rapid-scan imagery obtained from GOES. Rawinsonde data from Oklahoma City, Oklahoma at 0000 GMT, 30 April 1985, shown in Figure 6, was chosen as an initial sounding data for the iteration process and used to fill in the data in all grid points. Computation was carried out on the Cyber 205 super-computer at NASA Goddard Space Flight Center, Greenbelt, Maryland.

Figure 6 shows the skew T-log P temperature (solid line) and dew point temperature (dashed line) diagrams for Oklahoma City, Oklahoma at 0000 GMT, 30 April 1985. At altitudes below 500 mb, there were four different heights at which the temperature lapse rates were dry adiabatic. These heights were between 820 and 850 mb, between 680 and 730 mb, and between 510 and 540 mb. Temperature inversions existed between those unstable regions. In the upper troposphere, there existed a geight in which the temperature lapse rate was near dry adiabatic at the altitudes between 250 and 370 mb.

The possibility of cloud formation is dependent upon the amount of moisture available to provide an energy source for the initiation of condensation. Figure 3 shows the dew point temperature profile. Low temperature dew point depression is an indication of high moisture concentration. There was moist air all the way from 550 mb to the surface. The temperature dew point depression was smaller than 0.6^{0}c between the altitudes of 700 and 850 mb, and smaller than 0.8^{0}c between the altitudes of 590 and 610 mb.

It is known that a dynamical lifting mechanism can release conditional instability, thus the mesoscale convergence was superimposed in the cloud model. By using available temperature, moisture and wind profiles from rawinsonde observation all over the United States, the Barnes (1964) scheme was used to investigate the convergence and divergence of wind fields at different heights in the area of interest. The figures of convergence and divergence at different heights were also checked with the satellite rapid-scan imagery in which convergence can be estimated from satellite imagery for cloud top area rate of change (Wallace and Hobbs, 1977). In this case, lower level convergence was set at the heights of 2.0 and 6.0 km; while upper level divergence was set at 12.0 km. The magnitude of convergence unit was 6×10^{-5} s^{-1}.

Figure 7 shows the numerical simulation of the cloud height development of the Ardmore, Oklahoma storm clouds.

The air mass was fairly unstable between 820 to 850 mb, and between 680 to 730 mb. There was high concentration of moisture at the altitudes between 700 to 800 mb. A cloud was initiated at a 2 km height. This cloud grew rapidly and penetrated above the tropopause at 0030 GMT (calculation started at 0000 GMT based on the initial input sounding data of rawindsonde observed at that time). The clouds reached the altitude of 12.2 km at 0035 GMT. Then the cloud top started to oscillate up and down. The cloud top collapsed at 0045 GMT which was approximately 9 minutes before the touchdown of the Ardmore tornadoes, in good agreement with the results of our earlier satellite observation of tornadic storms (Hung et. al., 1980; 1983; 1984; Hung and Smith, 1982) and those of Fujita and his associates (Fujita and Caracena, 1977; Fujita and Byers, 1977). The cloud top experienced growth and collapse during the time period of the tornado touchdown. The cloud was collapsing at a high rate at 0125 GMT, approximately 6 minutes before the liftoff time of Ardmore tornadoes.

In contrast with the numerical simulation of the cloud height development of the Ardmore, Oklahoma storm clouds, shown in Figure 9 the cloud base variation of the storm clouds was also studied and shown in Figure 8. During the time period of the cloud formation and development, the cloud base was rather low and kept within the height of 0.8 km, untill the liftoff time of the tornado. The cloud base was then lifted

up to the height of 6.8 km when the storm cloud dissipated and the cloud top collapsed below the tropopause height. The maximum local condensation of liquid water content inside the cloud was calculated and shown in Figure 9. A large amount of local water vapor condensation, with the maximum value of liquid water content 8.3 g/kg, resulted when the up-draft motion pushed up the warm, moist air and overcame the temperature inversion. The value of liquid water content decreased when the cloud top started to collapse at 0045 GMT, and then increased to the value of 12.6 g/kg when the cloud reached to the maximum height at 0110 GMT. Figure 10 shows the instantaneous maximum vertical velocity of up-draft motion. The behavior of time dependent variation of the instantaneous maximum vertical velocity was in phase with growth and collapse of the cloud top, shown in Figure 7. In particular, a decrease in instantaneous maximum vertical velocity is an indicative of the decrease in vertical updraft momentum which implies a collapse of overshooting cloud tops penetrating above the tropopause resulting from the decreasing of updraft momentum which supports the much heavier air masses of overshooting cloud tops above the tropopause. An example of a dip in instantaneous maximum vertical velocity at 0105 GMT is an indicative of the collapse of overshooting cloud tops which was in phase with satellite observation.

Figure 7 also shows the variation of the local

tropopause heights modified by the formation and develoment of the storm clouds in the area. It has been shown that the local tropopause height started to decrease when the cloud top approached the altitude of the tropopause. The local tropopause height is also an indication of the boundary of the stable and unstable layers surrounding the clouds. In other words, clouds can only develop to the layer of the local tropopause height, unless there is a large vertical momentum with a very strong updraft motion which pushes up the cloud top and penetrates above the local tropopause. In general, the selection of the tropopause height follows the definition made by the World Meteorological Organization (WMO). In this study, the local tropopause height indicates the height of the layers of the boundary between the stable and unstable layers of the cloud tops surrounding the thunderstorm clouds. This selection of local tropopause height from the modeling calculation of cloud development was checked with the computed temperature profile based on the tropopause definition made by the WMO, and the boundary between stable and unstable layers of cloud tops observed from the rapid-scan imagery from the satellite. It is shown that the local tropopause heights started to decrease when the cloud top approached the altitude of tropopause. The local tropopause height reached a minimum height at 0040 GMT, approximately 14 minutes after the touchdown of the Ardmore tornado. The lowest local height of the tropopause was 11 km,

approximately 0.9 km below the observed tropopause height obtained from the sounding data. In this study, the observed tropopause height refers to the environmental height of the tropopause, and the local tropopause height indicates the height of the layers of the boundary between the stable and unstable layers of the cloud tops surrounding the thunderstorm clouds. The local tropopause height varied in phase with the height variation of the cloud top during the time period of the tornado touchdown. The local tropoapuse height increased to the higher altitude after the dissipation of the storm clouds.

Recently, by using satellite remote sensing measurements of ozone (data from the backscattered ultraviolet experiment on the Nimbus-4 satellite), and the ground truth measurements (that used ozonesonde data to investigate total ozone and the vertical distribution of the mixing ratio of ozone), variations of local tropopause heights were shown to be closely related to the observed ozone distribution (Hung and Liu, 1988). In other words, the decrease of local tropopause height could be influenced by the effects of the increasing of the following ozone parameters: (1) local concentration of total ozone content; (2) vertical profile of ozone mixing ratio at lower stratosphere and upper troposhere; and/or (3) concentration of ozone in the lower half of total column ozone (Hung and Liu, 1988). These variations of ozone concentration and vertical

distribution affect the variations of local tropopause heights which, in turn can be significant in making the contribution to the severe storm formation and development. In other words, the ozone concentration and its vertical profile is indicative of possibly important conditions leading to storm development.

Recently, Hung and Tsao (1987) studied four groups of severe storms, that produced 27 tornadoes in the midwestern and north central United States. The study showed that the local tropopause height: (1) started to decrease 7 to 12 hours (based on the best available rawinsonde data) before the storm formations, (2) reached their lowest heights at the time of the storm formation, and then (3) increased to an altitude higher than the pre-storm conditions after the dissipation of the storms (Hung and Tsao, 1987; 1988). These results are in agreement with the present study.

The intensity of storms can be related to the distance which overshooting cloud tops penetrate above the tropopause (Hung et. al., 1984). As it is shown in Figure 7, the local height of the tropopause varies during the time period of storm cloud development. A better picture will be seen if we can show the overshooting height of the storm clouds based on the calculated local height of tropopause. Figure 11 shows the overshooting height of the calculated modeling Ardmore storm clouds adjusted by the local tropopause height, based on the model calculation. It is

clearly shown that the cloud top penetrated above the tropopause at 0030 GMT and reached to the overshooting height of 1.2 km above the tropopause at 0035 GMT. The cloud top then oscillated and started to decrease to the overshooting height of 0.5 km above the tropopause at 0045 GMT, approximately 9 minutes before the touchdown of the Ardmore tornado. Then, the cloud tops grew and collapsed a couple of times during the time period when the Ardmore tornado swept over south central Oklahoma (Not shown in the figure. Figure 13 has been smoothed out in time coordinate.) Finally, the cloud tops collapsed with a high rate at 0125 GMT, approximately 6 minutes before the liftoff time of the Ardmore tornadoes. This figure illustrates a better picture for the development and dissipation of the Ardmore storms than that of Figure 7.

It is true that all overshooting cloud tops will eventually collapse, regardless of their association with tornadoes. However, the dissipation rate of the non-tornado-associated clouds is much slower, and the clouds can persist for several hours after the cloud top penetrates above the tropopause and reaches its highest altitude. The tornado-associated cloud collapsed in a very short time (Hung et. al., 1984; Hung and Tsao, 1987; 1988). The result of the present model simulation agrees with this conclusion.

5. Satellite Infrared Sensing of Storm Clouds

A three-minute interval rapid-scan imagery from GOES was used in this study. A quick view of the time history of the cloud formation and development for the Ardmore storm clouds, based on half-hourly satellite infrared imagery from GOES, is illustrated in Figure 2. There was no formation of clouds before 2300 GMT, 29 April 1985, in south central Oklahoma.

The satellite infrared imagery of the clouds show the cloud top temperatures as equivalent blackbody temperatures. For clouds with heights below the tropopause height, the temperature-height relationship can be determined from the rawinsonde observation shown in Figure 6; however, for clouds above the tropopause height, the relationship is rather complicated. Simpson and her associates, based on two aircraft observing the same cloud above tropopause height, determined that the heights of the cloud tops penetrating above the tropopause are consistent with the assumption of an approximate adiabatic lapse rate above the tropopause (Simpson, 1980; Hung et. al., 1985). Figure 12 shows the life cycle of satellite-observed Ardmore storm clouds, formation and development, in terms of growth and collapse of cloud tops, based on the technique developed by Simpson (1980) and her associates.

Figure 12 shows that the Ardmore storm cloud initiated at 2314 GMT. This cloud grew quickly and penetrated above the tropopause in less than 20 minutes. The tropopause

height was determined from rawinsonde data shown in Figure 6. The cloud top started to oscillate up and down and grew up to 13 km height (1.2 km above the tropopause height) at 0045 GMT. At this moment, the cloud top collapsed and produced funnel clouds observed on the ground. The cloud top collapsing time, observed by the satellite, was approximately 9 minutes before the touchdown of the Ardmore tornadoes, in good agreement with the results of other observations (Hung et. al., 1984). The rapid-scan satellite imagery also shows that the cloud cells grew and collapsed one after another while the Ardmore storm clouds moved toward the northeast with a velocity of 13 km/hr when tornadoes swept over the south central Oklahoma. The cloud finally collapsed at a high rate, at the altitude of 12.5 km, at 0125 GMT, approximately 6 minutes before the liftoff time of the Ardmore tornadoes.

The temperature distribution of the Ardmore storm clouds responsible for the outbreak of the tornadic storms at 0100 GMT (9 minutes after the tornado touchdown), based on satellite infrared imagery, is shown in Figure 13. Rawinsonde data at Oklahoma City, Oklahoma showed that the tropopause temperature was -57° C at 0000 GMT. The lowest satellite-observed cloud top temperature, -60° C, at the southwestern part of the cloud, was the highest altitude overshooting cloud top of the cloud responsible for the formation of the funnel cloud. Again, this cloud moved

toward the northeast direction with a velocity of 13 km/hr when the tornadoes hit the area, described in Section 2 of this paper.

6. Discussion and Conclusions

The life cycle of the Ardmore storm clouds has been studied based on cloud modeling with input sounding data from Oklahoma City, Oklahoma, and rapid-scan imagery from GOES. Satellite imagery shows that there was no formation of clouds before 2300 GMT, 29 April 1985 in the area of the tornado occurrence, and the storm clouds initiated at 2314 GMT. The simulation started at 0000 GMT, 30 April 1985, at the time of sounding. Cloud formation and development, in terms of growth and collapse of cloud tops, based on cloud modeling and rapid-scan imagery from the satellite are superimposed and shown in Figure 14. Tropopause height, shown in the figure, is from rawinsonde data.

Figure 14 shows that the cloud heights in model simulation were significantly less than for satellite remote sensing between 0000 and 0030 GMT. The reason can be illustrated as follows. Satellite infrared imagery from GOES shows that there was no any cloud formation before 2300 GMT, 29 April 1985 in south central Oklahoma. Satellite imagery further shows that the cloud started to form around 2314 GMT, and grew rapidly to the mature stage within one hour. In the numerical simulation of storm cloud formation,

the closest available rawinsonde data was 0000 GMT, 30 April 1985. In other words, the simulation started at 0000 GMT, 30 April 1985, rather than 2300 GMT, 29 April 1985. This explains why the cloud heights in model simulation were significantly less than for satellite remote sensing between 0000 and 0030 GMT. The simulation catched up quickly, and the cloud started to penetrate above the tropopause at 0035 GMT.

There are several agreements between these two approaches of study which are shown as follows: (1) clouds developed to a mature stage with overshooting cloud tops penetrated above the tropopause and collapsed at 0045 GMT, approximately 9 minutes before the touchdown of tornadoes; (2) maximum height of cloud tops for modeling was 13.7 km, while that for sensing from satellite was 13.5 km, and the difference was only 0.2 km; and (3) the cloud tops collapsed with a high rate at 0125 GMT, approximately 6 minutes before the liftoff time of the tonadoes.

Since the temperature of the overshooting cloud top penetrating above the tropopause is below the temperature of the surrounding air, the mass density of the overshooting turret is much higher than the mass density of the surrounding air. The high mass density overshooting turret can only exist as long as it is dynamically supported by intense vertical convection; therefore, as the intense vertical convection disappears, the overshooting turret collapses.

Figure 12 shows the evolution of instantaneous maximum vertical velocity of the modeled Ardmore, Oklahoma clouds which exhibited the following characteristics: (1) increasing of vertical velocity before the initiation of collapsing of overshooting cloud tops and the tornado touchdown (comparing to Figure 11); (2) zigzag changing of the vertical velocity during the time period of tornado touchdown (comparing to Figures 10 and 11); and (3) decreasing of vertical velocity during the time of the liftoff of tornadoes (again comparing to Figures 10 and 11). The magnitude of force per unit area supporting the weight of the high mass density overshooting turret is proportional to the height of the cloud top above the tropopause and the difference between the temperature of the turret and the ambient environment (Hung and Tsao, 1987). The downward collapsing rate of the overshooting turret is, therefore, proportional to the height of the cloud top above the tropopause and the temperature difference. This makes the height of the cloud top above the tropopause and the temperature difference critical in studying the initiation of the downdraft motion which produces the funnel cloud. Figure 10 shows that the cloud base was: (1) decreasing when the overshooting cloud top was penetrating above the tropopause; (2) becoming the lowest height during the time period of the tornado touchdown; and (3) increasing to the higher altitude after the time of the tornado liftoff.

The difference between the overshooting cloud top height and the local tropopause height, a measure of how much the cloud has penetrated above the tropopause, is important in the development of severe storms (Hung and Smith, 1983; Hung and Tsao, 1987; and 1988). Furthermore, this final difference will increase toward the storm production when the tropopause height decreases during the time period of storm formation. In this study, it is shown that the local tropopause heights started to decrease when the cloud top reached to the altitude of tropopause due to local subsidence around the overshooting top. The local tropopause height decreased to the lowest height, approximately 16 minutes after the touchdown of the tornadoes. The tropopause height increased to the higher altitudes after the dissipation of storm clouds.

Acknowledgements

The authors wish to thank the Office of Space Sciences and Applications, the National Aeronautics and Space Administration Headquarters, through NASA Grant NAGW-1165, which supported the present research.

References

Barnes, S. L., 1964, A technique for maximizing detail in numerical map analysis. Journal of Applied Meteorology, 3, 396-409.

Barnes, S. L., 1976, Severe local storms: concepts and understanding. Bulletin of American Meteorological Society, 57, 412-419.

Chang, S. W., and H. D. Orville, 1973, Large scale convergence in a numerical cloud model. Journal of Atmospheric Sciences, 30, 947-950.

Chen, C. H. and H. D. Orville, 1980, Effects of mesoscale convergence on cloud convection. Journal of Applied Meteorology, 19, 256-274.

Curry, M. J., and R. C. Murty, 1974, Thunderstorm-generated gravity waves. Journal of Atmospheric Sciences, 31, 1402-1408.

Fujita, T. T. and H. R. Byers, 1977, Spearhead echo and downburst in the crash of an airliner. Monthly Weather Review, 105, 129-146.

Fujita, T. T. and F. Caracena, 1977, An analysis of three weather related aircraft accidents. Bulletin of American Meteorological Society, 58, 1164-1181.

Gossard, E. E., and W. B. Sweezy, 1974, Dispersion and spectra of gravity waves in the atmosphere. Journal of Atmospheric Sciences, 31, 1540-1548.

Hung, R. J., J. C. Dodge, and R. E. Smith, 1983, The life cycle

of a tornadic cloud as seen from a geosynchronous satellite. American Institute of Aeronautics and Astronautics Journal, 21, 1217-1224.

Hung, R. J., and J. P. Kuo, 1978, Ionospheric observation of gravity waves associated with Hurricane Eloise. Journal of Geophysics, 45, 67-80.

Hung, R. J., and J. M. Liu, 1988, Satellite remote sensing and ozonesonde observation of ozone vertical profile and severe storm development. International Journal of Remote Sensing, 9, 469-475.

Hung, R. J., J. M. Liu, and R. E. Smith, 1985, Infrared remote sensing of convective clouds and amount of rainfall over the Tibet Plateau area. Annales Geophysics, 3, 767-776.

Hung, R. J., T. Phan, D. C. Lin, R. E. Smith, R. R. Jayroe, and G. S. West, 1980, Gravity waves and GOES IR data study of an isolated tornadic storm on 29 May 1977. Monthly Weather Review, 108, 456-464.

Hung, R. J., T. Phan, and R. E. Smith, 1978, Observation of gravity waves during the extreme tornado outbreak of 3 April 1974. Journal of Atmospheric and Terrestrial Physics, 40, 831-843.

Hung, R. J., T. Phan, and R. E. Smith, 1979a, Case studies of gravity waves associated with isolated tornadic storms on January 13, 1976. Journal of Applied Meteorology, 18, 460-466.

Hung, R. J., T. Phan, and R. E. Smith, 1979b, Coupling of ionosphere and troposphere during the occurrence of isolated tornadoes on November 20, 1973. Journal of Geophysical Research, 84, 1261-1268.

Hung, R. J., and R. E. Smith, 1978, Ray tracing of gravity waves as a possible warning system for tornadic storms and hurricanes. Journal of Applied Meteorology, 17, 3-11.

Hung, R. J., and R. E. Smith, 1981, Ionospheric remote sensing of medium scale gravity waves and tornadic storms. Il Nuovo Cimento, 4C, 339-358.

Hung, R. J., and R. E. Smith, 1982, Remote sensing of tornadic storms from geosynchronous satellite infrared digital data. International Journal of Remote Sensing, 3, 69-81.

Hung, R. J., and R. E. Smith, 1983, Remote sensing of Arkansas tornadoes on 11 April 1976 from a satellite, a balloon and an ionospheric sounder array. International Journal of Remote Sensing, 4, 617-630.

Hung, R. J., and Y. D. Tsao, 1987, Study of prestorm environment by using rawinsonde and satellite observations. International Journal of Remote Sensing, 8, 1123-1150.

Hung, R. J., and Y. D. Tsao, 1988, Satellite remote sensing and cloud modeling of St. Anthony, Minnesota storm clouds and dew point depression. Annales Geophysics, 6,

453- 462.

Hung, R. J., and Y. D. Tsao, 1989, Study of Ardmore, Oklahoma storm cloud initiation and development based on gravity wave-induced convection. International Journal of Remote Sensing, 10, in press.

Hung, R. J., Y. D. Tsao, D. L. Johnson, A. J. Chen, C. H. Lin, J. M. Cheng, and C. M. You, 1988, VHF radar remote sensing of atmospheric parameters over Taiwan during the time period of Typhoon Wayne. International Journal of Remote Sensing, 9, 477-493.

Hung, R. J., Y. D. Tsao, C. C. Lee, D. L. Johnson, A. J. Chen, C. H. Lin, and J. J. Pan, 1989, Observation of VHF radar on mesospheric and HF Doppler sounder on thermospheric density disturbances caused by typhoons and convective storms in the western Pacific area. Journal of Spacecraft and Rockets, 26, in press.

Hung, R. J., D. Y. Tsao, and R. E. Smith, 1984, Case study of Pampa, Texas multicell storms. Pure and Applied Geophysics, 121, 1019-1034.

Kuo, H. L., 1965, On formation and intensification of tropical cyclones through latent heat release by cumulus convection. Journal of Atmospheric Sciences, 22, 40-63.

Kuo, H. L., 1974, Further studies of the parameterization of the influence of cumulus convection on large-scale flow. Journal of Atmospheric Sciences, 31, 1232-1240,

National Climate Data Center, 1985, Storm Data, 27, 4-5.

Newton, C. W. 1963, Dynamics of severe local storms. In Severe Local Storms, Meteor. Mongr. 5, American Meteorological Society, Boston, Mass., 33-58.

Orville, H. D., 1965, A numerical study of the initiation of cumulus clouds over mountain terrain. Journal of Atmospheric Sciences, 22, 684-699.

Orville, H. D., R. D. Farley, and J. H. Hirsch, 1984, Some surprising results from simulated seeding of stratiform-type clouds, Journal of Climate and Applied Meteorology, 23, 1585-1600.

Orville, H. D., and F. J. Kopp, 1977, Numerical simulation of the life history of hailstorm. Journal of Atmospheric Sciences, 34, 1596-1618.

Pielke, R. A., 1974, A three dimensional numerical model of the sea breezes over south Florida. Monthly Weather Reviews, 102, 115-139.

Purdom. J. F. W., 1976, Some uses of high-resolution GOES imagery in the mesoscale forecasting of convection and its behavior. Monthly Weather Reviews, 104, 1474-1483.

Schlesinger, R. E., 1973a, A numerical model of deep convection: Part I. Comparative experiments for variable ambient moisture and wind shear. Journal of Atmospheric Sciences, 30, 835-856.

Schlesinger, R. E., 1973b, A numerical model of deep

convection: Part II. A prototype experiment and variations upon it. Journal of Atmospheric Sciences, 30, 1374-1391.

Sikdar, D. N., V. E. Suomi and C. E. Anderson, 1970, Convective transport of mass and energy in severe storms over the United States-an estimate from a geosynchronous altitude. Tellus, 22, 521-532.

Simpson, J., 1980, Progress report for the period October 1, 1979 to Occtober 1, 1980. NASA/GSFC, Greenbelt, Maryland, 88p.

Stull, R. B., 1976, Internal gravity waves generated by penetrative convection. Journal of Atmospheric Sciences, 33, 1279-1286.

Uccellini, L. W., 1975, A case study of apparent gravity waves initiation of severe convective storms. Monthly Weather Reviews, 103, 497-513.

Wallace, J. M., and P. V. Hobbs, 1977, Atmospheric Science, An Introductory Survey, Academic Press, New York, pp. 467.

Figure Captions

Figure 1 Radar summary of central United States at 2235 GMT, 29 April 1985.

Figure 2 Sample microbarograph data from Dallas/Ft. Worth, Texas; Amarillo, Texas; and San Angelo, Texas, during the time period of 2040-2155 GMT, 29 April 1985.

Figure 3 Growth of mesoscale convective cloud, located at south central Oklahoma, during the time period from 2330 GMT, 29 April 1985 to 0200 GMT, 30 April 1985 based on satellite infrared imagery of GOES west. Figures (A) at 2330 GMT, (B) at 0000 GMT, (C) at 0030 GMT, (D) at 0100 GMT, (E) at 0130 GMT, and (F) at 0200 GMT.

Figure 4 Geographical distribution of surface divergence, with a unit of 10^{-5} sec^{-1} (negative value implies convergence, and positive value, divergence) in the area of south central United States, at 0000 GMT, 30 April 1985.

Figure 5 Geographical distribution of surface moisture content (mixing ratio, with a unit of g/kg) in the area of south central United States, at 0000 GMT, 30 April 1985.

Figure 6 Vertical temperature and dew point temperature profile in a skew T, log P, diagrams for Oklahoma City, Oklahoma at 0000 GMT, 30 April 1985, from

rawinsonde data.

Figure 7 Life cycle of cloud height development of Ardmore, Oklahoma storm clouds, and variation of local tropopause height modified by the formation and development of storm clouds, based on the results of cloud modeling.

Figure 8 Life cycle of cloud base height development of Ardmore, Oklahoma storm clouds, based on the results of cloud modeling.

Figure 9 Evolution of maximum liquid water content of Ardmore, Oklahoma storm clouds, based on the results of cloud modeling.

Figure 10 Evolution of instantaneous maximum vertical velocity of Ardmore, Oklahoma storm clouds, based on the results of cloud modeling.

Figure 11 Height of Ardmore storm cloud tops overshooting the computed tropopause level based on cloud model computation.

Figure 12 Life cycle of Ardmore storm clouds, in terms of the development and dissipation of cloud tops, based on the rapid-scan imagery from GOES.

Figure 13 Cloud-top temperature distribution of the convective cloud located at south central Oklahoma, at 0100 GMT, 30 April 1985, based on satellite infrared imagery.

Figure 14 Superposition of life cycle of Ardmore storm clouds

based on the results of cloud modeling and also based on the observation from rapid-scan satellite imagery.

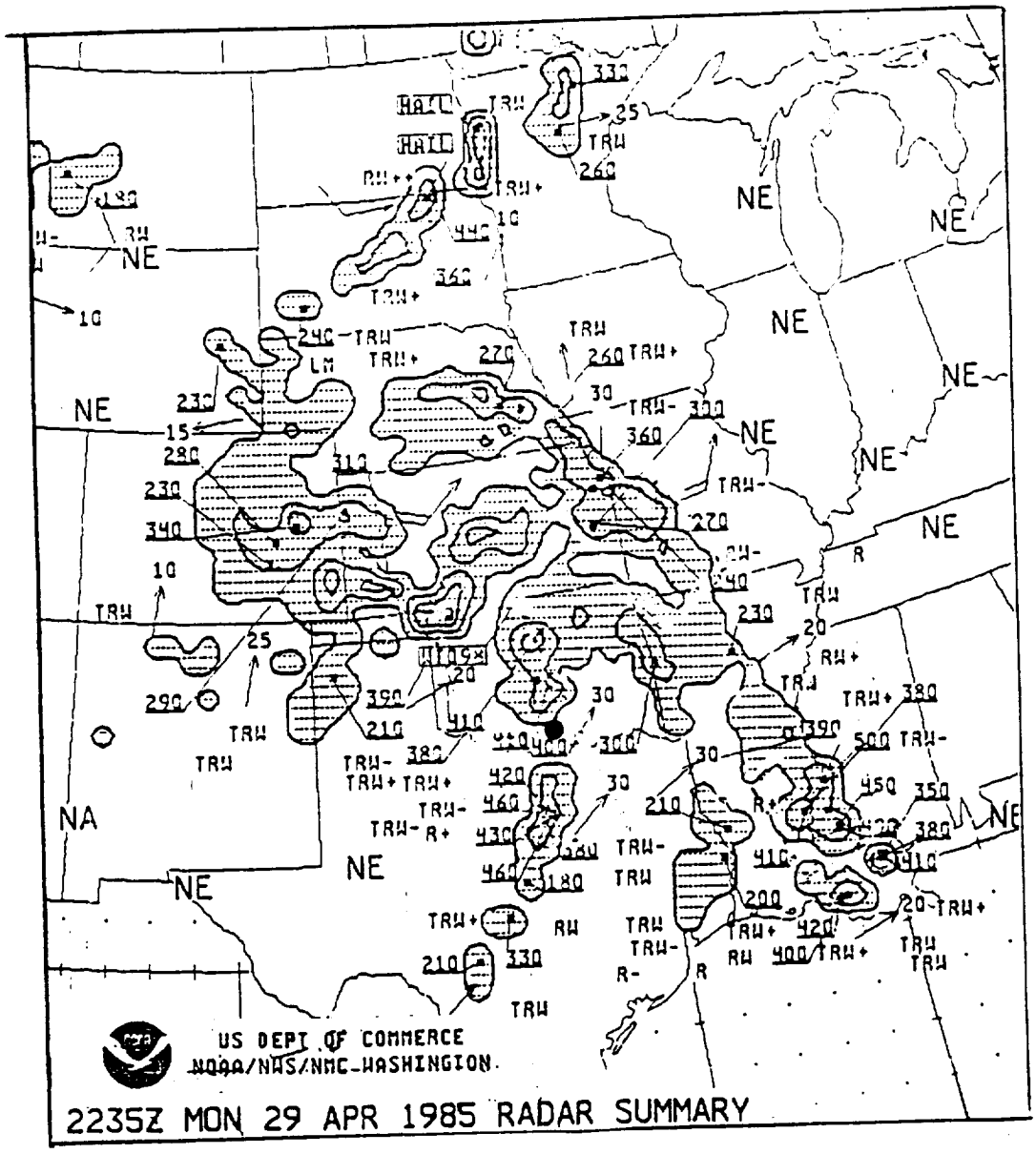
US DEPT OF COMMERCE
NOAA/NWS/NMC-WASHINGTON
2235Z MON 29 APR 1985 RADAR SUMMARY

FIG. 1

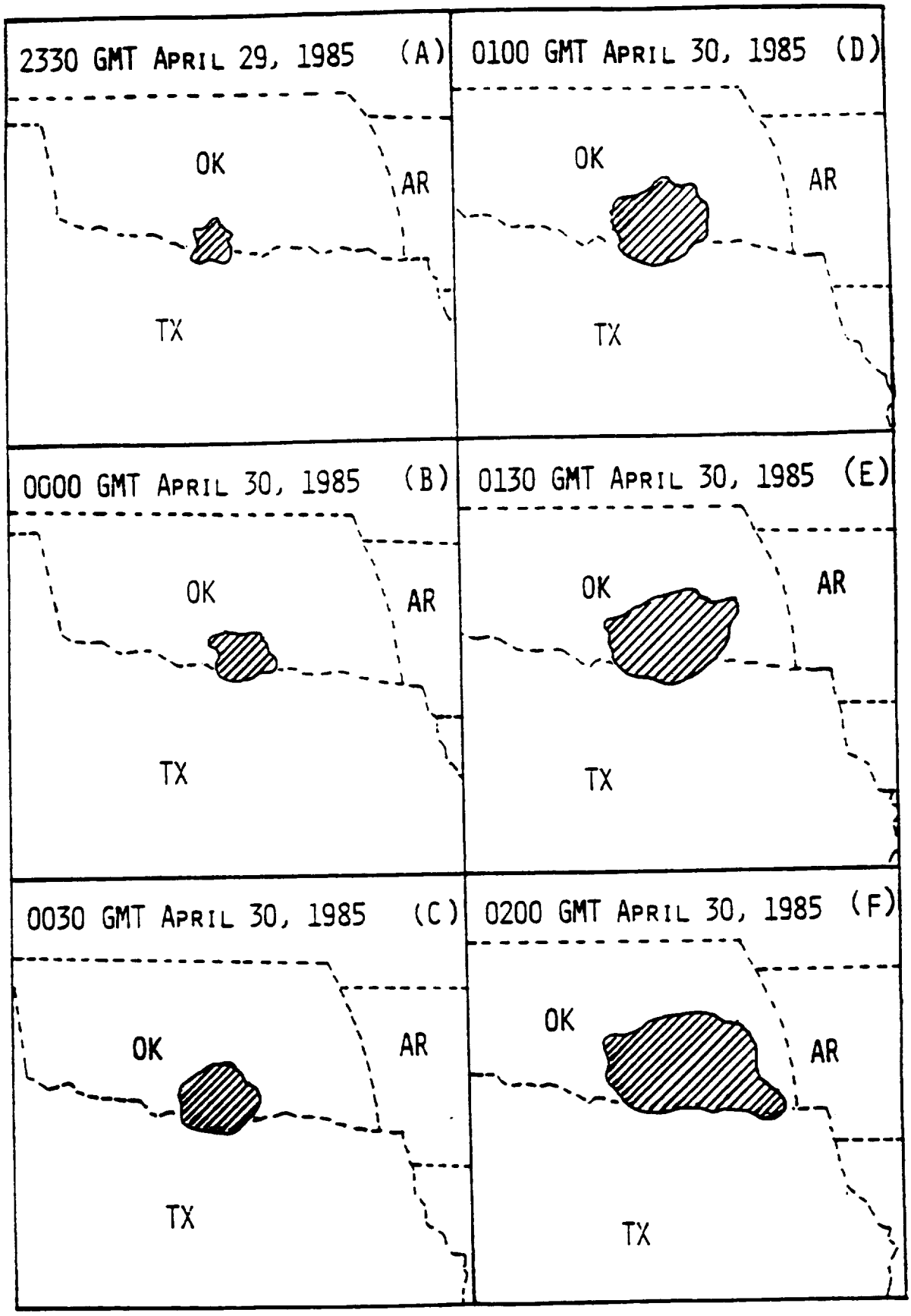
2330 GMT APRIL 29, 1985 (A)
OK
AR
TX
0100 GMT APRIL 30, 1985 (D)
OK
AR
TX
0000 GMT APRIL 30, 1985 (B)
OK
AR
TX
0130 GMT APRIL 30, 1985 (E)
OK
AR
TX
0030 GMT APRIL 30, 1985 (C)
OK
AR
TX
0200 GMT APRIL 30, 1985 (F)
OK
AR
TX

FIG. 2

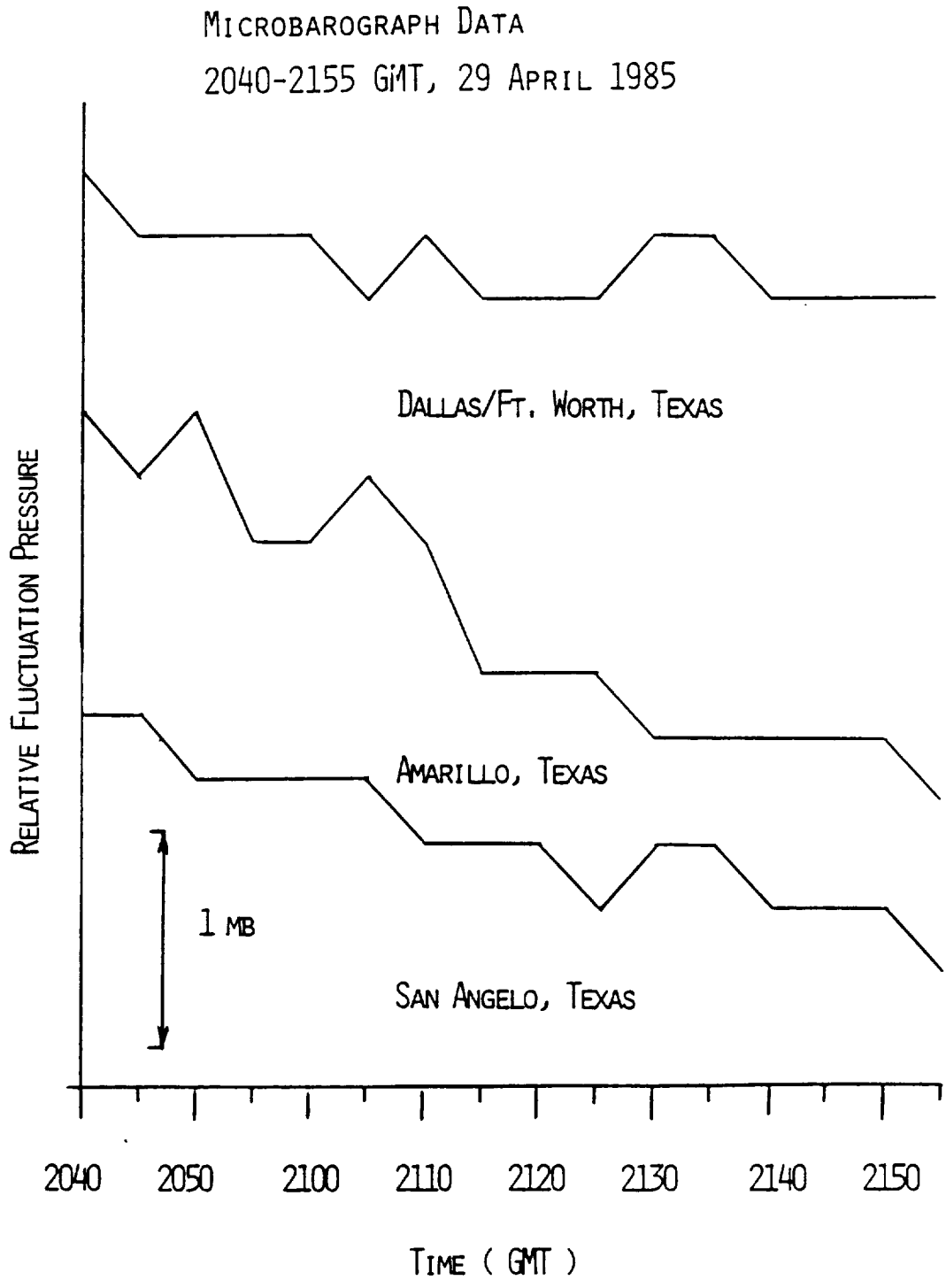
MICROBAROGRAPH DATA
2040-2155 GMT, 29 APRIL 1985
DALLAS/FT. WORTH, TEXAS
AMARILLO, TEXAS
SAN ANGELO, TEXAS
1 MB
RELATIVE FLUCTUATION PRESSURE
2040
2050
2100
2110
2120
2130
2140
2150
TIME (GMT)

FIG. 3

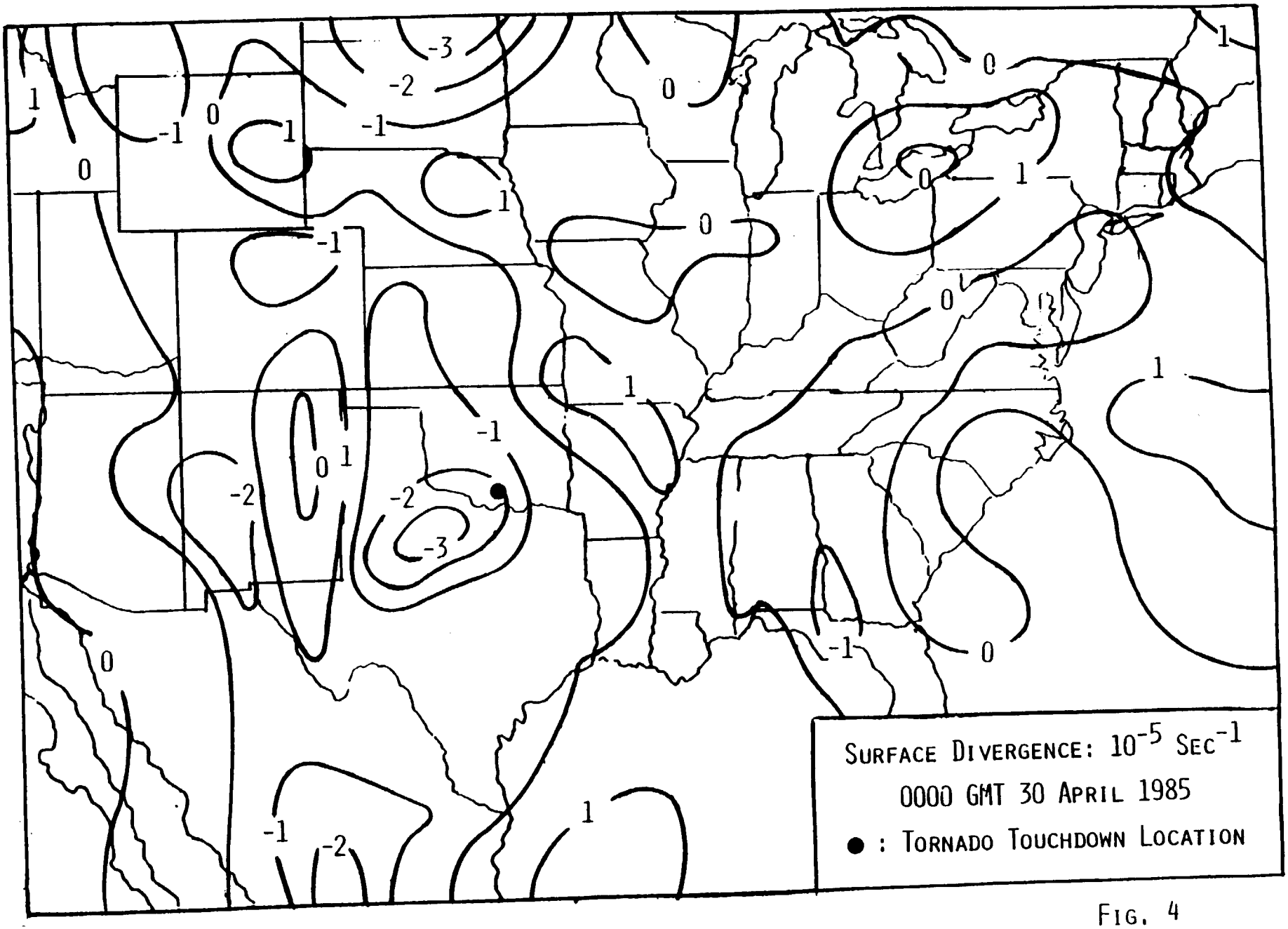
SURFACE DIVERGENCE: 10^{-5} SEC^{-1}
0000 GMT 30 APRIL 1985
● : TORNADO TOUCHDOWN LOCATION

FIG. 4

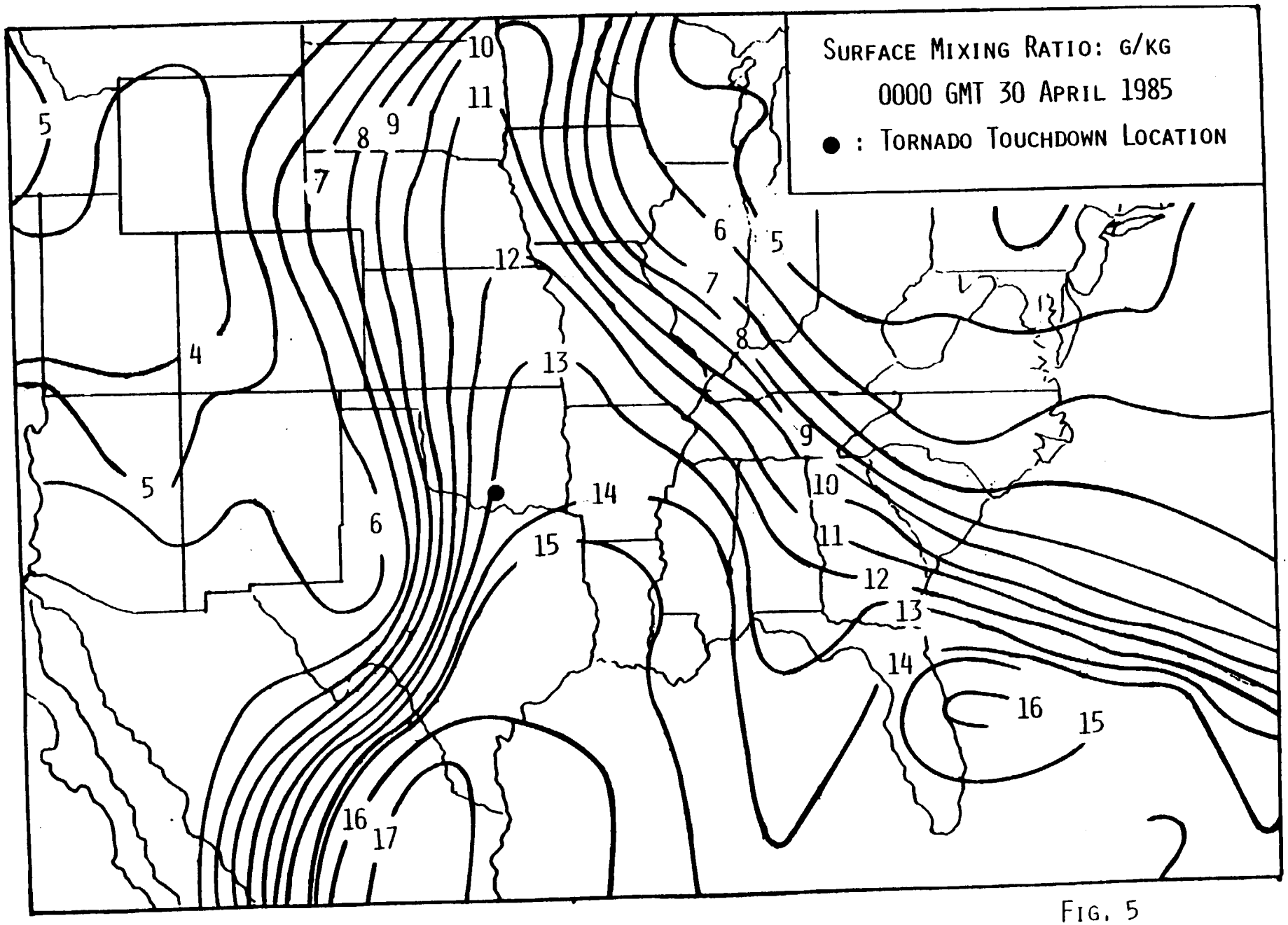
SURFACE MIXING RATIO: G/KG
0000 GMT 30 APRIL 1985
● : TORNADO TOUCHDOWN LOCATION
5
10
11
8
9
7
12
6
5
7
13
8
4
13
9
5
14
10
6
15
11
12
13
14
16
15
16
17

FIG. 5

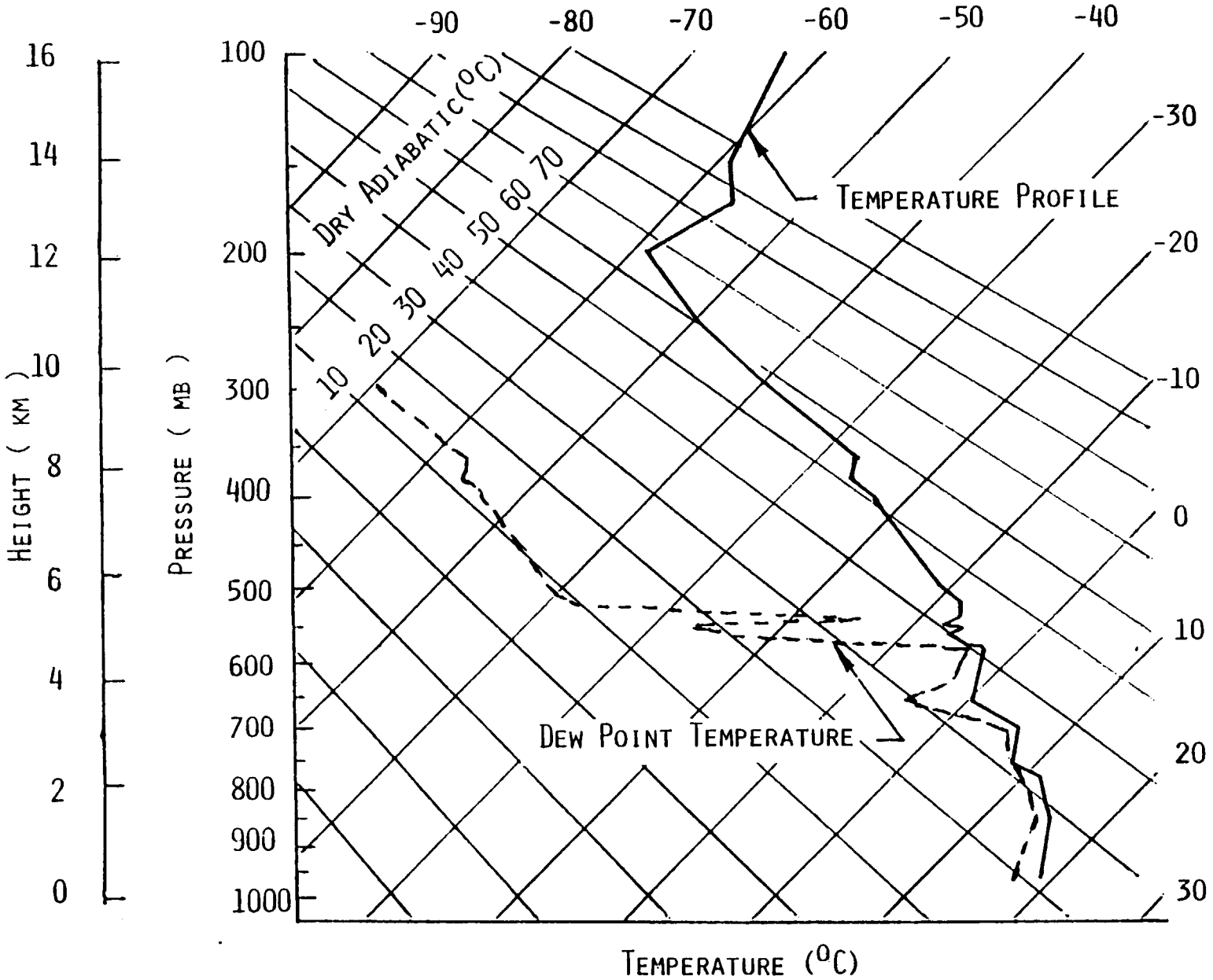
-90
-80
-70
-60
-50
-40
100
200
300
400
500
600
700
800
900
1000
16
14
12
10
8
6
4
2
0
-30
-20
-10
0
10
20
30
DRY ADIABATIC(°C)
10 20 30 40 50 60 70
TEMPERATURE PROFILE
DEW POINT TEMPERATURE
HEIGHT (KM)
PRESSURE (MB)
TEMPERATURE (°C)
OKLAHOMA CITY
OKLAHOMA
0000 GMT
APRIL 30, 1985

FIG. 6

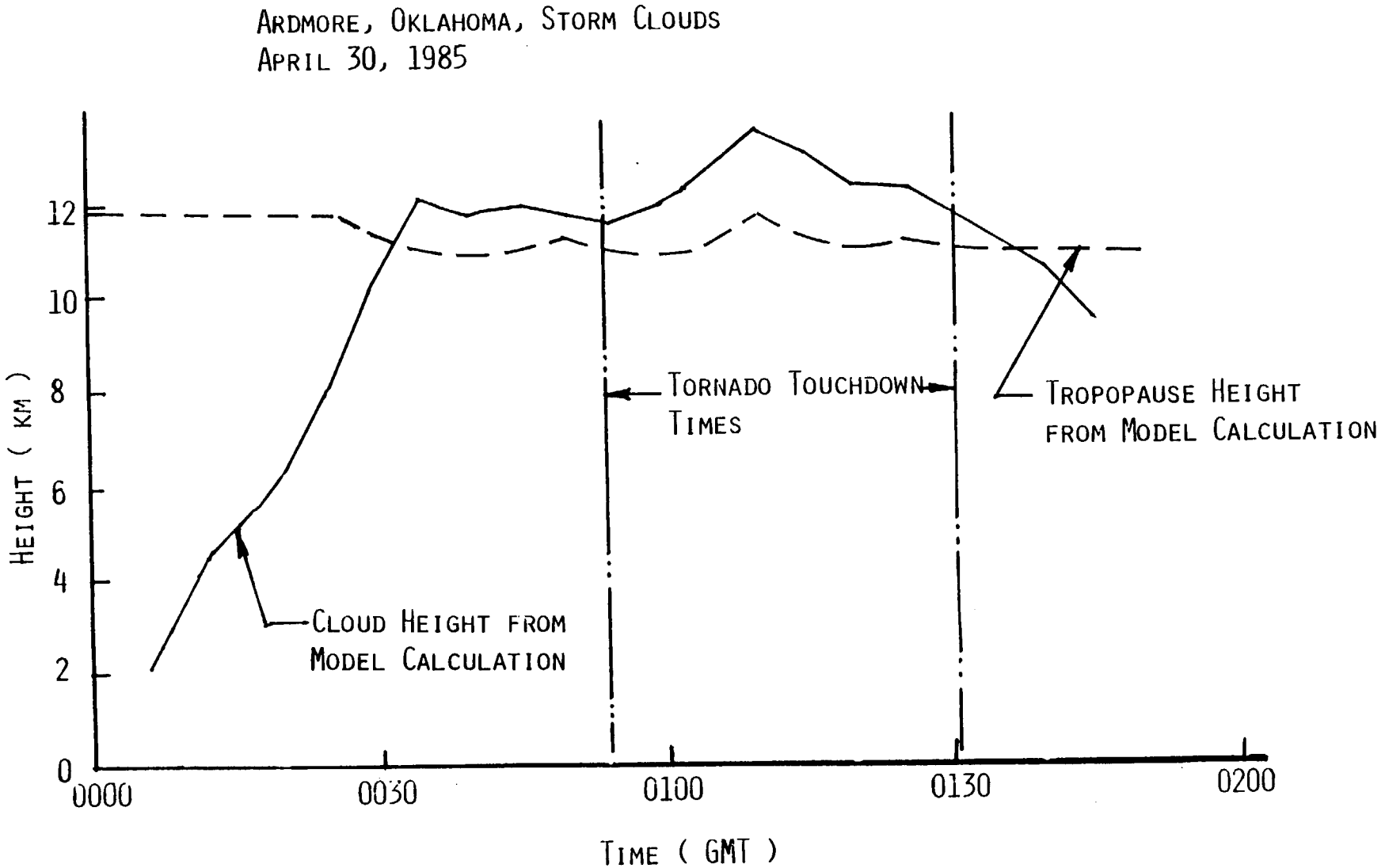
ARDMORE, OKLAHOMA, STORM CLOUDS
APRIL 30, 1985
HEIGHT (KM)
12
10
8
6
4
2
0
0000
0030
0100
0130
0200
TIME (GMT)
TORNADO TOUCHDOWN TIMES
TROPOPAUSE HEIGHT FROM MODEL CALCULATION
CLOUD HEIGHT FROM MODEL CALCULATION

FIG. 7

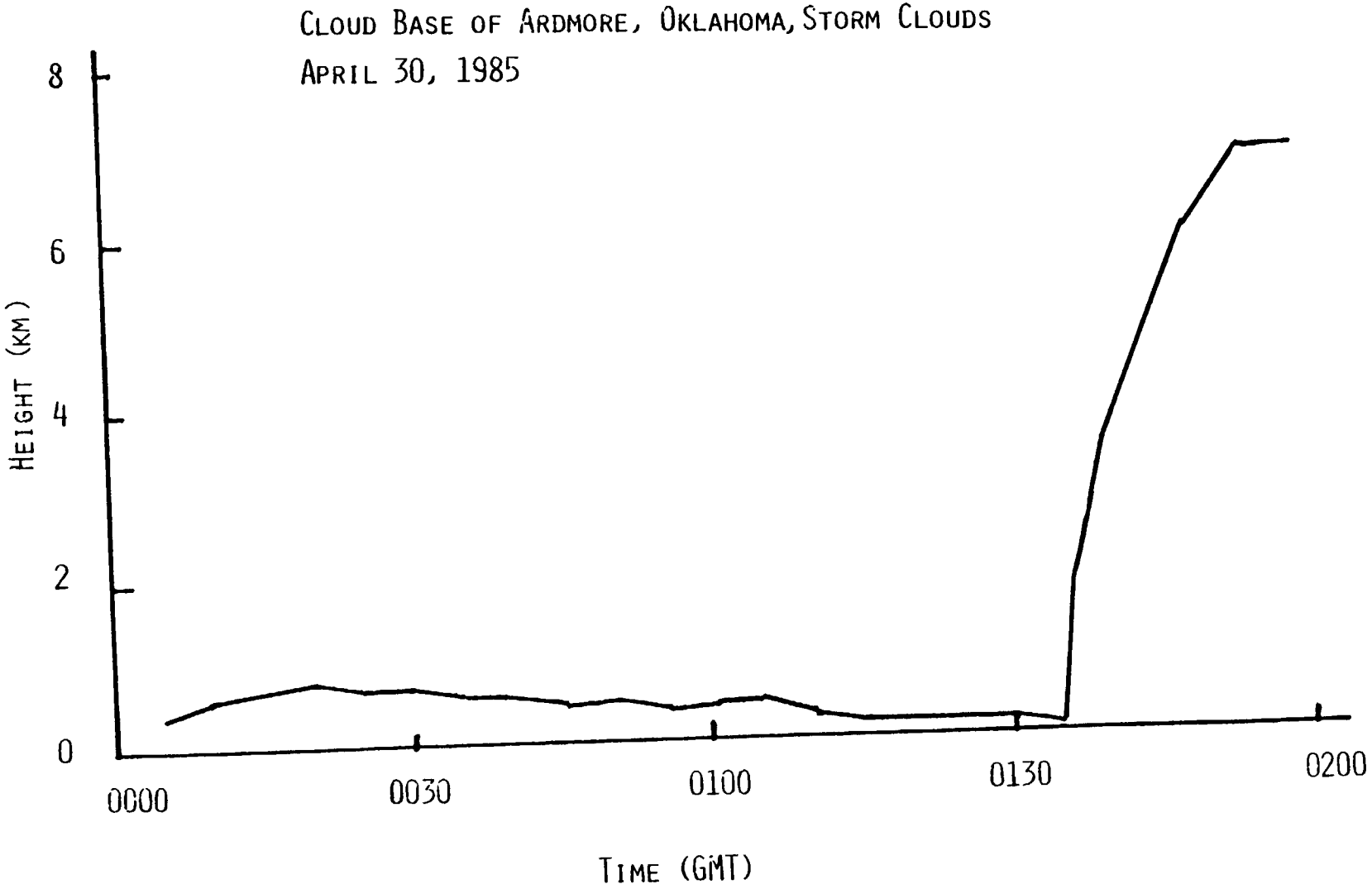
CLOUD BASE OF ARDMORE, OKLAHOMA, STORM CLOUDS
APRIL 30, 1985
8
6
4
2
0
HEIGHT (KM)
0000
0030
0100
0130
0200
TIME (GMT)

FIG. 8

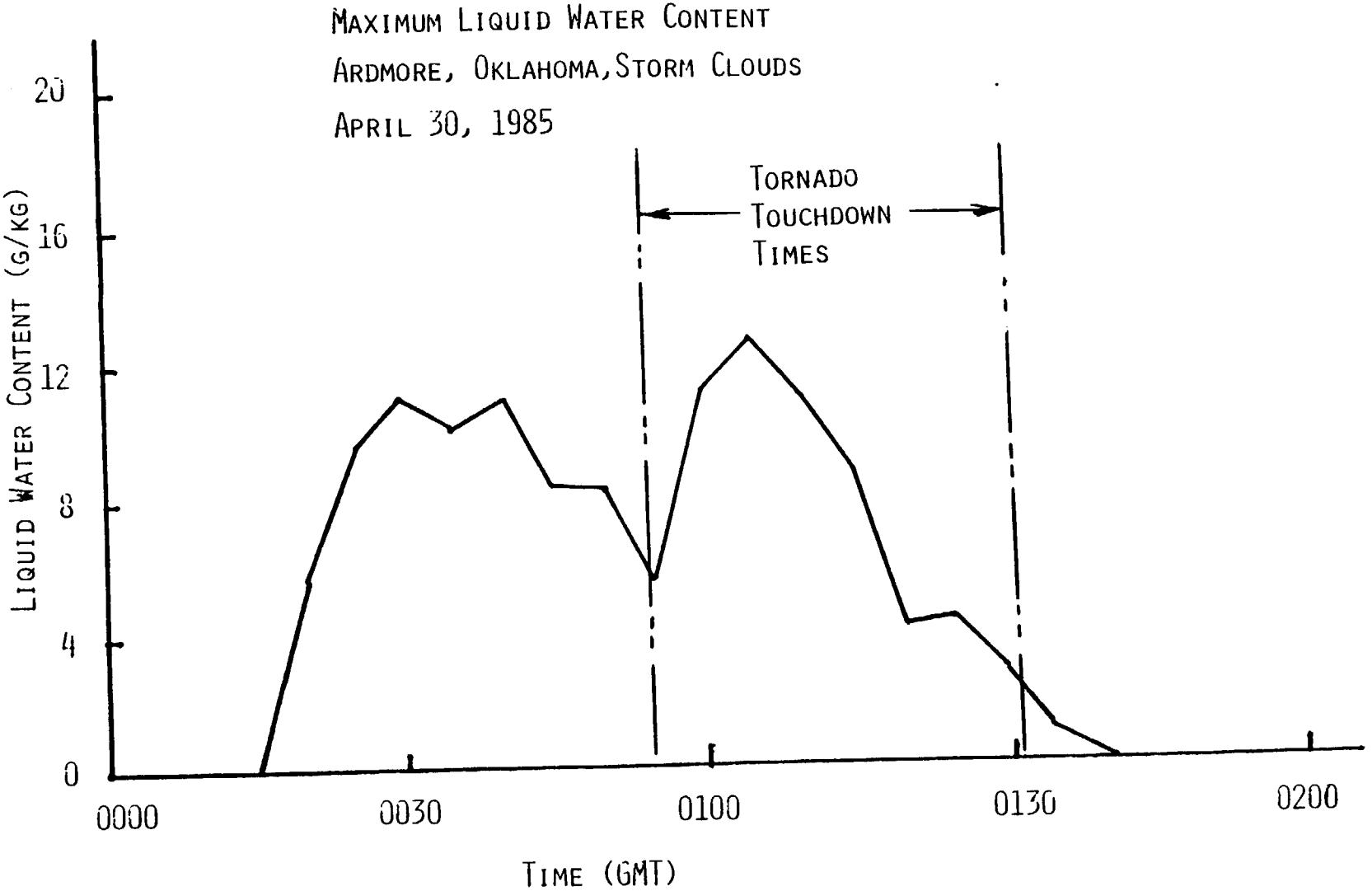
MAXIMUM LIQUID WATER CONTENT
ARDMORE, OKLAHOMA, STORM CLOUDS
APRIL 30, 1985
TORNADO
TOUCHDOWN
TIMES
LIQUID WATER CONTENT (G/KG)
20
16
12
8
4
0
0000
0030
0100
0130
0200
TIME (GMT)

FIG. 9

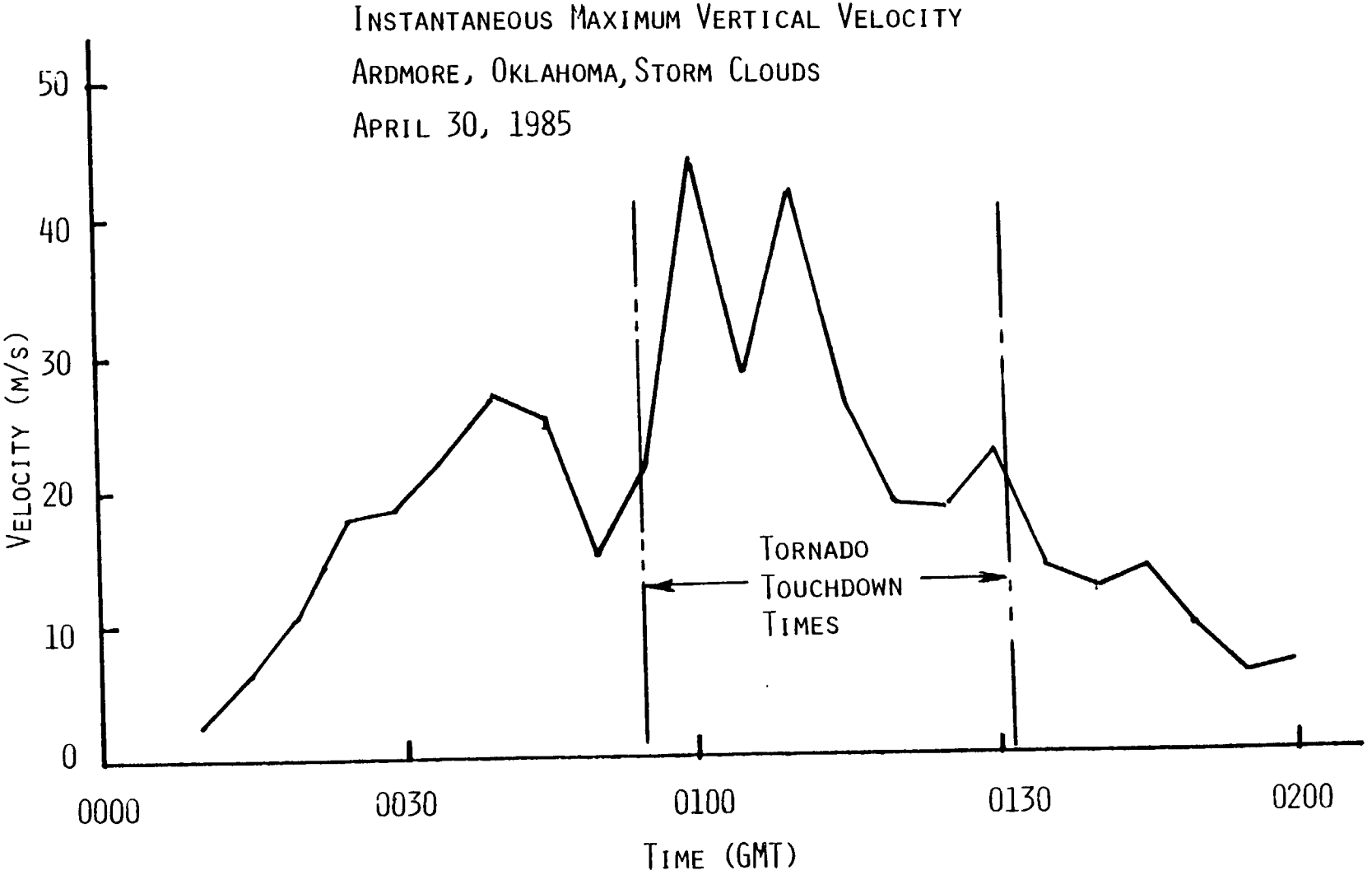
INSTANTANEOUS MAXIMUM VERTICAL VELOCITY
ARDMORE, OKLAHOMA, STORM CLOUDS
APRIL 30, 1985
VELOCITY (M/S)
50
40
30
20
10
0
TORNADO
TOUCHDOWN
TIMES
0000
0030
0100
0130
0200
TIME (GMT)

FIG. 10

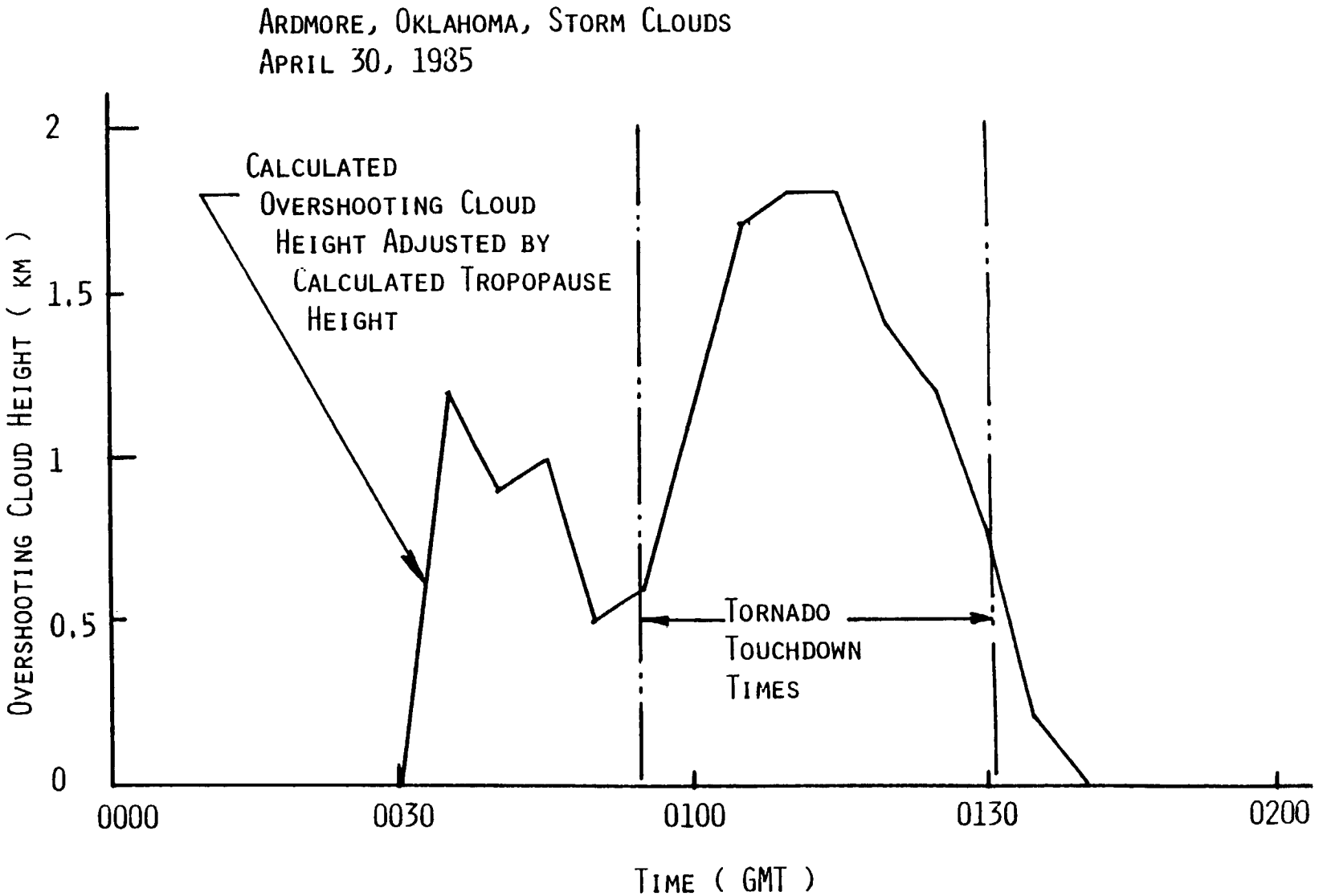
ARDMORE, OKLAHOMA, STORM CLOUDS
APRIL 30, 1935
CALCULATED
OVERSHOOTING CLOUD
HEIGHT ADJUSTED BY
CALCULATED TROPOPAUSE
HEIGHT
TORNADO
TOUCHDOWN
TIMES
OVERSHOOTING CLOUD HEIGHT (KM)
2
1.5
1
0.5
0
0000
0030
0100
0130
0200
TIME (GMT)

FIG. 11

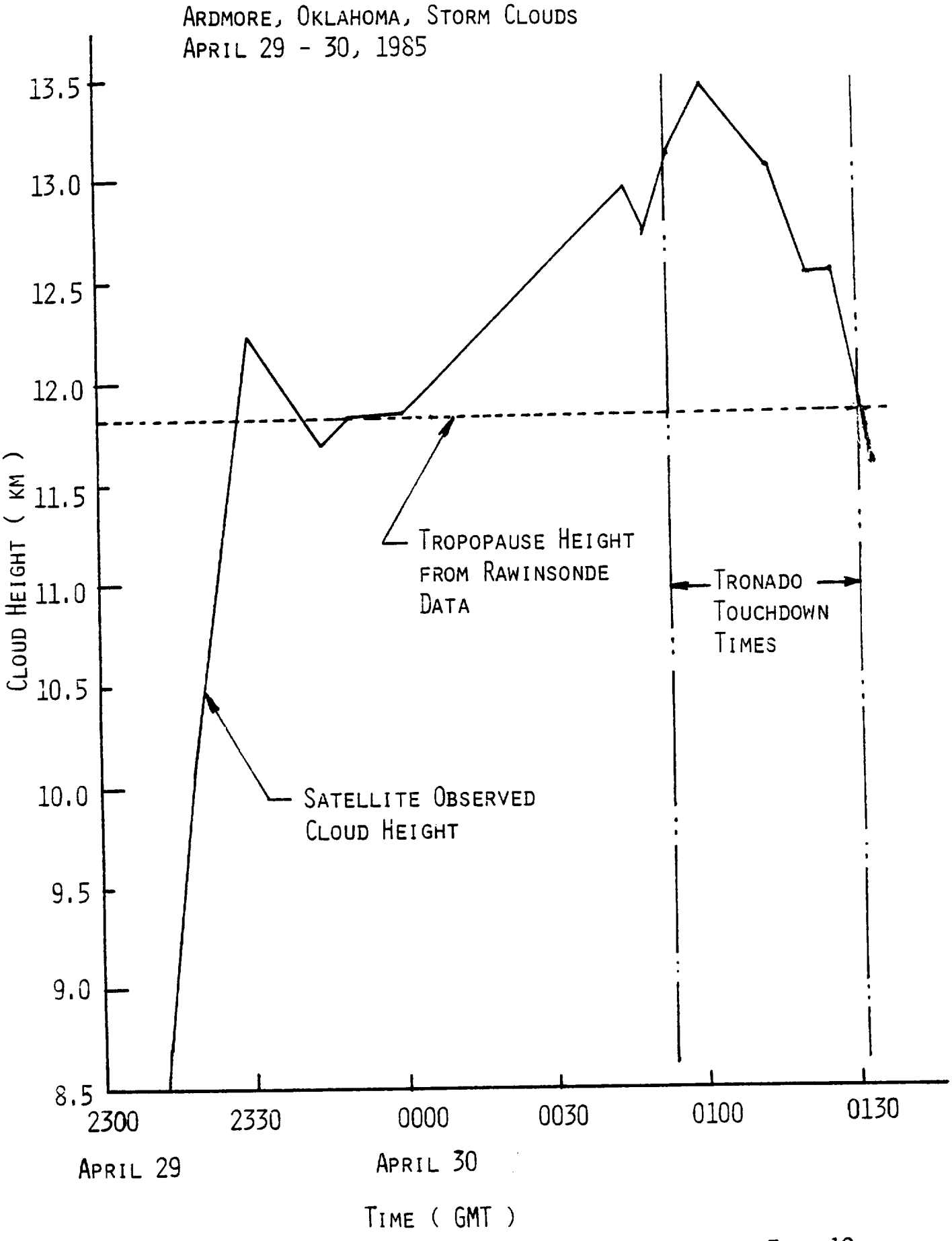
ARDMORE, OKLAHOMA, STORM CLOUDS
APRIL 29 - 30, 1985
13.5
13.0
12.5
12.0
11.5
11.0
10.5
10.0
9.5
9.0
8.5
CLOUD HEIGHT (KM)
TROPOPAUSE HEIGHT FROM RAWINSONDE DATA
TRONADO TOUCHDOWN TIMES
SATELLITE OBSERVED CLOUD HEIGHT
2300
2330
0000
0030
0100
0130
APRIL 29
APRIL 30
TIME (GMT)

FIG. 12

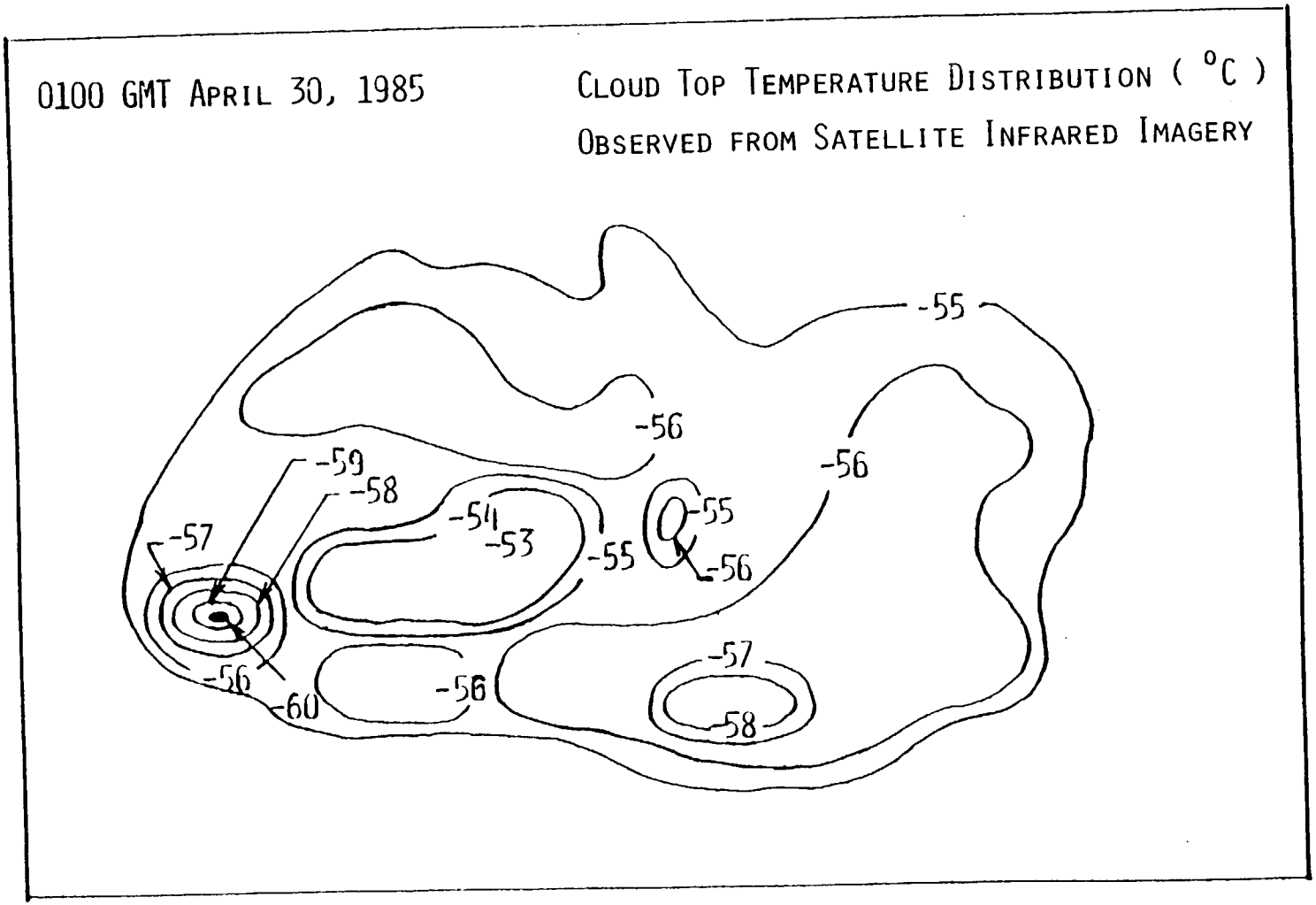
0100 GMT April 30, 1985
Cloud Top Temperature Distribution (°C)
Observed from Satellite Infrared Imagery
-55
-56
-59
-58
-57
-54
-53
-55
-55
-56
-56
-56
-57
-60
-56
-58

Fig. 13

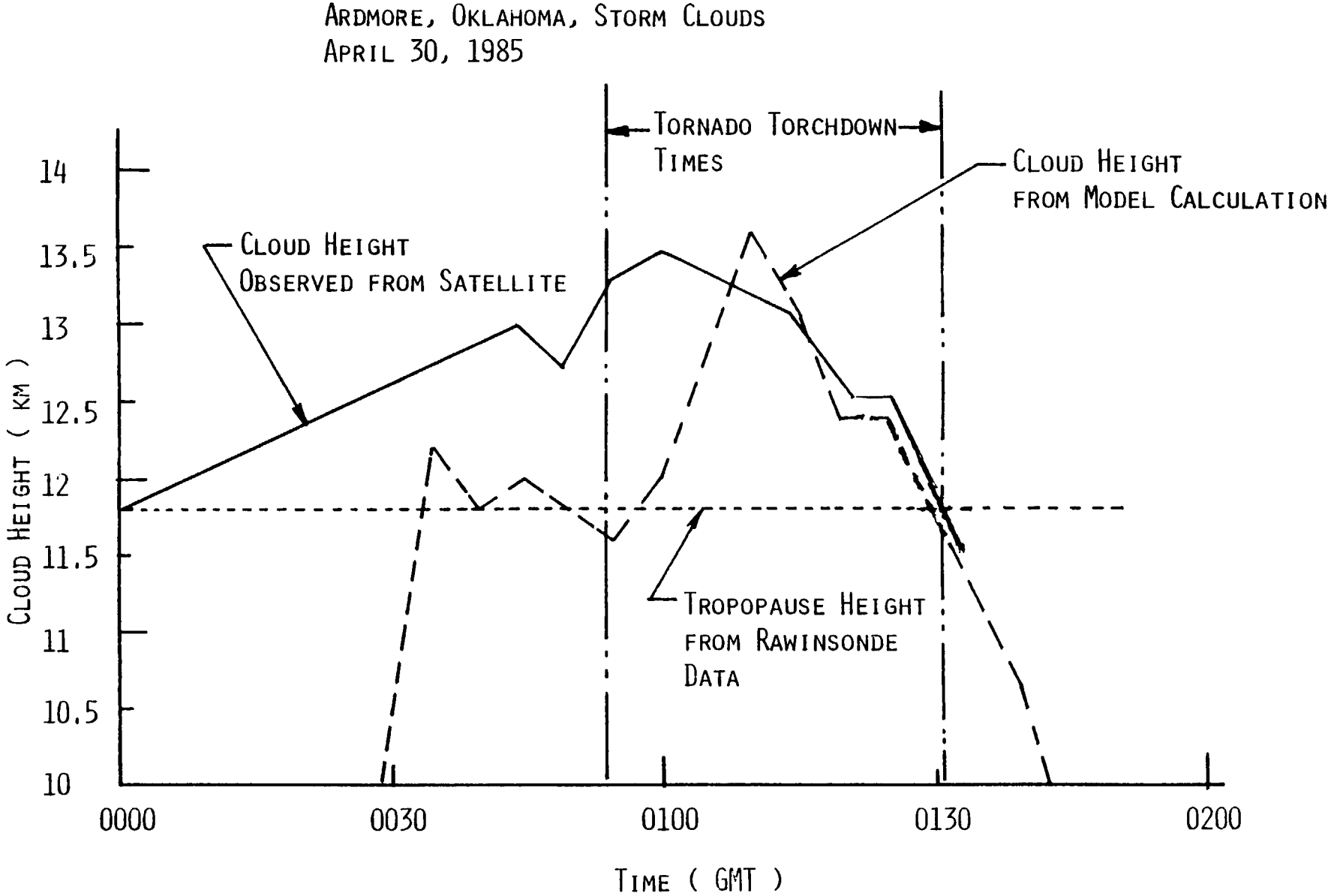
ARDMORE, OKLAHOMA, STORM CLOUDS
APRIL 30, 1985
TORNADO TORCHDOWN TIMES
CLOUD HEIGHT FROM MODEL CALCULATION
CLOUD HEIGHT OBSERVED FROM SATELLITE
TROPOPAUSE HEIGHT FROM RAWINSONDE DATA
CLOUD HEIGHT (KM)
14
13.5
13
12.5
12
11.5
11
10.5
10
0000
0030
0100
0130
0200
TIME (GMT)

FIG. 14